TESIS DE LA UNIVERSIDAD
DE ZARAGOZA
2017
64

Rosa María Monge Prieto

Development and application of microtechnologies in the design and fabrication of cell culture biomimetic systems

Departamento

Ingeniería Mecánica

Director/es

Fernández Ledesma, Luis José
Ochoa Garrido, Ignacio
Doblaré Castellano, manuel

ISSN 2254-7606

Prensas de la Universidad
Universidad Zaragoza

ISSN 2254-7606

Tesis Doctoral

DEVELOPMENT AND APPLICATION OF MICROTECHNOLOGIES IN THE DESIGN AND FABRICATION OF CELL CULTURE BIOMIMETIC SYSTEMS

Autor

Rosa María Monge Prieto

Director/es

Fernández Ledesma, Luis José
Ochoa Garrido, Ignacio Doblaré
Castellano, manuel

UNIVERSIDAD DE ZARAGOZA
Ingeniería Mecánica

2017

Development and application of microtechnologies in the design and fabrication of cell culture biomimetic systems

PhD thesis by
Rosa María Monge Prieto

Doctoral advisors
Dr. Manuel Doblaré Castellano
Dr. Luis J. Fernández Ledesma
Dr. Ignacio Ochoa Garrido

PhD Programme in **Computational Mechanics**
March 2017

Universidad
Zaragoza
1542

Development and application of microtechnologies in the design and fabrication of cell culture biomimetic systems

PhD thesis by
Rosa María Monge Prieto

Doctoral advisors
Dr. Manuel Doblaré Castellano
Dr. Luis J. Fernández Ledesma
Dr. Ignacio Ochoa Garrido

PhD Programme in **Computational Mechanics**
March 2017

Universidad
Zaragoza
1542

Son tiempos difíciles para los soñadores.
- Amélie -

Agradecimientos

Me resulta muy paradójico que esta parte de la tesis, los agradecimientos, que *a priori* es un texto libre, en castellano y que siempre se deja para el final, me esté resultando la más difícil de escribir. Supongo que esto se debe a que es la única parte no-técnica y por ello, es en la única en la que uno se muestra cómo realmente es. Y mostrarse siempre es un acto complicado.

Me gustaría comenzar agradeciendo al Dr. Manuel Doblaré la oportunidad que me brindó, hace ya unos cuántos años, por acogerme en su grupo de investigación; primero como estudiante realizando el Proyecto Fin de Carrera, y posteriormente confiando en mis capacidades al proporcionarme los medios para poder llevar a cabo esta tesis doctoral. También tengo que agradecerle enérgicamente que me diera la oportunidad de trabajar con el Dr. Luis J. Fernández y el Dr. Ignacio Ochoa. Dejando formalismos a un lado, Luis, Iñaki, nunca os estaré suficientemente agradecida por todo el apoyo que me habéis dado durante estos años, por la confianza. Me gustaría que supieseis que os considero mis mentores, que considero una suerte increíble el poder haber trabajado con vosotros, y que espero que podamos seguir haciéndolo juntos muchos más años y con éxito.

No me puedo olvidar de los compañeros del laboratorio, Chema, María, Alan, Guillermo, José Luis, Rebeca, Clara, Sara, Roxana y de todos los que han pasado (entre ellos todos mis estudiantes de proyecto) porque las horas en el trabajo son más llevaderas si se trabaja con gente como vosotros.

Los técnicos de Sala Blanca, donde tantas y tantas horas he pasado, Rubén, Isabel, Gala, siempre dispuestos a echarme una mano.

I would also like to thank Dr. Séverine Le Gac for the welcome she gave me during my stay at the University of Twente, for treating me as one of her research group and also for all the help she gave me in order to settle down. Dr. Adithya Sridhar ... what can I say ... life became easier the day I started to understand your English. The only person I know who, with a mobile phone and a glass of water, is able to do science in a bar. Thank you very much for being my friend. I'll wait for you in Zaragoza.

Quiero dar también las gracias a mis amigos: Belén, Carmelo, Clara, Héctor, María, Marta, Noelia, Samuel y Sara porque lo seguís siendo a pesar de mi perpetua falta de tiempo y de no poder veros tanto como me gustaría.

Si hay un resultado tangible de mi tesis, ese es BEOnChip, así que además de a Luis y a Iñaki (una vez más), gracias por embarcaros en esta aventura conmigo, también me parece de justicia darles las gracias a Camille Bertrand y a Luz López por toda la ayuda, apoyo e incluso sufrimiento que comparten con nosotros. Es increíble ver cómo algo tan tuyo es tan bien aceptado y tratado con el cariño con el que vosotras los hacéis.

A los compañeros de SpinUp y de CEMINEM, en especial a Iván y Alejandro ("los Herizont"), Marcos y Lucía ("los REMOTs"), Luis E. ("emprendido" con el que he tenido la suerte de compartir también unas cuantas horas en sala blanca) y Joaquín (llevas años estando, estás y quiero que sigas estando). Es una suerte y un privilegio compartir este momento de ilusión con vosotros.

A todo el equipo de BEOnChip. Que nuestro camino juntos sea largo y exitoso.

A Carlos, por su paciencia y apoyo incondicional. Seguiremos descubriendo la vida juntos.

Por último, a mis padres, Aurelio y Emilia. Esta tesis es vuestra, como todo lo que haga o consiga en la vida, porque todo os lo debo a vosotros. Muchas gracias por apoyarme y también por cuestionarme. No tiene que ser fácil entender las decisiones que he ido tomando en la vida, pero sé que siempre os tengo a mi lado. Gracias por haberme dado la educación que me habéis dado. Gracias por los valores que me habéis inculcado. Gracias porque sé que, con aciertos y errores, todo lo hacéis por mi bien. Muchas gracias. Os quiero.

Abstract

"Lab-On-a-chip" systems have proved to be a promising tool in the field of biology. Currently, cell culture is performed massively on Petri dishes, which have traditionally been used in cell culture laboratories and tissue engineering. However, having proved to be a widely used tool until now, the scientific community has largely described the lack of correlation between the results obtained in the laboratory and the clinical results. This lack of connection between what has been studied in the laboratories and what has been observed in the clinic has led to the search for more advanced alternative tools that allow results to be obtained closer to reality. Thus, the use of microtechnologies in the field of biomedical engineering, presents itself as the perfect tool as an alternative to obsolete traditional media. Thanks to the low volumes of liquid it presents for its use, it also makes it an essential technology for the testing of drugs, new compounds and materials. By being able to more accurately reproduce the biomimetic environment of cell cultures and tissues, they make this technique fundamental as an intermediate step between basic *in vitro* laboratory tests and preclinical animal tests, resulting from this way in the best alternative for the reduction of both the use of animal models, as in times and costs.

For a biomimetic system to be as such, it also needs another series of complementary devices for its better functioning. Micro-valves, micro pumps, flow sensors, O2 sensors, pH, CO2 are fundamental for the correct functioning and sophistication of biomimetic systems. This complexity, on the other hand, is often not perceived by the user since the miniaturization of all these components makes "Lab-On-a-Chip" systems smaller every day, despite numerous control components that can be incorporated.

This thesis presents some examples of different microfluidic devices designed and manufactured through the use of microtechnologies, with all applications, focused on their use in biomimetic systems.

Resumen

Los sistemas “Lab-On-a-chip se han revelado como una prometedora herramienta en el campo de la biología. Actualmente, el cultivo celular se realiza de manera masiva en placas Petri, las que tradicionalmente se han venido utilizando en laboratorios de cultivo celular e ingeniería de tejidos. Sin embargo, habiendo demostrado ser una herramienta de gran utilizad hasta la fecha, la comunidad científica ha descrito ampliamente la falta de correlación entre los resultados obtenidos en el laboratorio con los resultados clínicos. Esta falta de conexión entre lo estudiado en los laboratorios y lo observado en la clínica, ha llevado a la búsqueda de herramientas alternativas más avanzadas y que permitan la obtención de resultados más cercanos a la realidad. Así, el uso de las microtecnologías en el campo de la ingeniería biomédica, se presenta como la herramienta perfecta como alternativa a los obsoletos medios tradicionales. Gracias a los bajos volúmenes de líquido que presenta para su uso, la hacen, además, una tecnología imprescindible para el testeo de fármacos, nuevos compuestos y materiales. Al ser capaz de reproducir de una manera más fidedigna el entorno biomimético de los cultivos celulares y de los tejidos, convierten a esta técnica en fundamental como un paso intermedio entre los ensayos básicos *in vitro* en laboratorio, y los ensayos preclínicos en animales, resultando de esta manera en la mejor alternativa para la reducción tanto del uso de modelos animales, como en tiempos y costes. Para que un sistema biomimético lo sea como tal, además necesita de otra serie de dispositivos complementarios para su mejor funcionamiento. Microválvulas, microbombas, sensores de flujo, sensores de O2, pH, CO2 son fundamentales para el correcto funcionamiento y sofisticación de los sistemas biomiméticos. Esta complejidad, por el contrario, muchas veces no llega a ser percibida por el usuario ya que la miniaturización de todos estos componentes hace que los sistemas “Lab-On-a-Chip sean cada día más pequeños, a pesar de los numerosos componentes de control que pueda llevar incorporados.

Esta tesis presenta algunos ejemplos de diferentes dispositivos microfluídicos diseñados y fabricados mediante el uso de las microtecnologías, con aplicaciones todas ellas, enfocadas a su uso en sistemas biomiméticos.

Contents

Contents

List of Figures

List of Tables

Thesis

Chapter 1

Introduction

1.1 General overview

This thesis presents some examples of microfluidic devices integrable in systems for cell culture applications as well as for their control or manipulation by the user, such as flow sensors and microfluidic packagings. The aim of this chapter is to describe, in a general manner, the use of microtechnologies in cell cultures in biomimetic environments, as well as different fabrication methods that are currently used.

1.2 Microfluidics

Born in the 80's initially under the development of microelectromechanical systems (MEMS), **microfluidics** has become a discipline itself over the years [1–3]. Although first devices where based on silicon or glass materials, with the development of polymer-based fabrication techniques, the democratization of the use of microfluidic devices has started. **Polymer-based microfluidic devices become more prevalent with the advantages of being economic, easy to fabricate, material versatility, a wide range of applications and good system compatibility**. The early applications of microfluidic were focused in control systems, where the miniaturization of components such as microvalves, micropumps and micromixer [4–6] where the starting point. With further development, whole microfluidic systems were achieved with the integration of flow sensors, microactuactors or microreactors. Also, the fields in which microfluidic is present range from mechanics (mass transport effects [7, 8] and flow control [9, 10], biology (drug development, diagnosis, genome and proteins sequence) and chemistry (chemical microreactors).

1.2.1 Fabrication methods and materials

The fabrication processes of microfluidic devices have been changing with the passage of time. In the early years, its manufacture and the materials used were based on those developed for the realization of integrated circuits (IC) using their same processes, such as photolithography, thin film metallization and chemical etching. The appearance of new materials, glass-based, glass-silicon, glass-polymer made the number of users of this type of devices increasing, as well as their processing techniques [6, 11–23]. The main advantages of **glass and silicon based devices** are the biocompatibility (indispensable for biomedical applications), transparency (only for glass devices), chemical and high temperatures resistance. On the other hand, the manufacturing method used for these devices is micromachining, which becomes in high expensive devices, which has slowed its use in the search for more applications in microfluidics. In the search to get cheaper and faster techniques, in the decade of the 70's began to use the soft-lithography technique. **Soft-lithography** usually refers to the moulding of a bi-component polymer (the elastomer and the curing agent), called PDMS (polydimethylsiloxane) using a master. The ability to have designs on PDMS devices is limited by the design of the master. The main advantages of the manufacturing of devices in PDMS are the speed, the transparency of the material, the low cost (not that of the masters, although they are reusable), the simplicity of the technique and the biocompatibility. On the other hand, PDMS is a material that allows the gas exchange and presents absorption of organic compounds when they are used in cell culture applications. **Optical photolithography** processes have traditionally been used to obtain masters to, for example, use them with soft-lithography. But these processes themselves are also used to obtain microfluidic devices. The most used material is the SU-8, a negative photoresist that allows to obtain devices on substrates like glass or silicon, or to have devices manufactured entirely in SU-8. The photolithography process used to obtain these devices is based on the deposition of the resin on a wafer with a spin-coating process, obtaining a succession of very thin layers of controlled thickness. By the application of UV-light and a mask with the desirable patter, the wafers are developed in a later step, obtaining this way, the devices to be used as masters for soft-lithography. In the case of devices manufactured entirely in SU-8 this process is performed on two separate wafers that finally undergo a controlled bonding process. The advantages of the SU-8 as processing material are transparency, high-resolution structures, reproducibility and biocompatibility. The mains disadvantages are the need for specialized equipment and medium cost-effective. In recent years the trend has shown a

Materials	**Advantages**	**Disadvantages**
Glass/Silicon	Biocompatibility, temperature and chemical resistance, transparency (only glass)	High cost fabrication
PDMS	Transparency, low cost, biocompatibility	Gas diffusion, unspecific molecules absorbance
SU-8	3D geometries, biocompatibility, transparency	Medium cost-effective
Thermoplastics	Transparency, biocompatibility, low cost production	Initial invest in molds, post processing

Table 1.1. Advantages and disadvantages of different material used in microfluidics.

growing interest in the use of **thermoplastic materials** for the development of new microfluidic devices, which is highly attractive due mainly to its low cost (compared to silicon and glass), easier to be fabricated and presents a friendly integration in complex systems. There are many types of thermoplastics and for each specific application it should be chosen the most appropriated, but generally stand out for good optical transparency, biocompatibility and good chemical and mechanical properties. But the most interesting reason why this type of device is where the industry and the academy are moving is the possibility of making disposable devices for biomedical and clinical applications. These devices have a low cost of production, are highly reproducible, are mass-produced and have a high versatility in terms of applications. Table 1.1 shows a comparison of the materials presented above.

The current manufacturing methods can be divided into three groups: direct fabrication techniques, prototyping techniques, and mass production techniques.

Direct techniques. As their name implies, they allow the direct manufacture of microfluidic devices. The main direct fabrication techniques are: laser micromachining, photolithography and X-ray lithography. In the case of laser micromachining, the surface of the substrate (glass, silicon, etc.) is directly attached by a laser that records the desired pattern. In the case of photolithography, the working process has been briefly explained when the SU-8 material was introduced. Starting from a rigid substrate, one or more negative photoresist layers are deposited. For its polymerization, UV-light is applied with the mask where the patter is defined. Different layers of photoresist can be deposited and different masks applied. The last step would be the development to remove the photoresist that has not been exposed to ultraviolet light. This manufacturing process of microfluidic devices has been used in all cases in this Thesis and in each of the chapters the method of manufacture is widely explained. In the case of X-ray lithography, the process is similar to the previous one. Starting from a rigid substrate, a positive photoresist layer is deposited, which is exposed to X-ray with the mask where the desired pattern is defined. Unlike in the case of photolithography, this time the area exposed to X-ray will be the material that will be removed by developing. A layer of metal is deposited and after removing the rest of the photoresist, the master is already prepared to be able to obtain microfluidic devices by replication. Figure 1.1 shows the manufacturing process of photolithography and X-ray lithography processes.

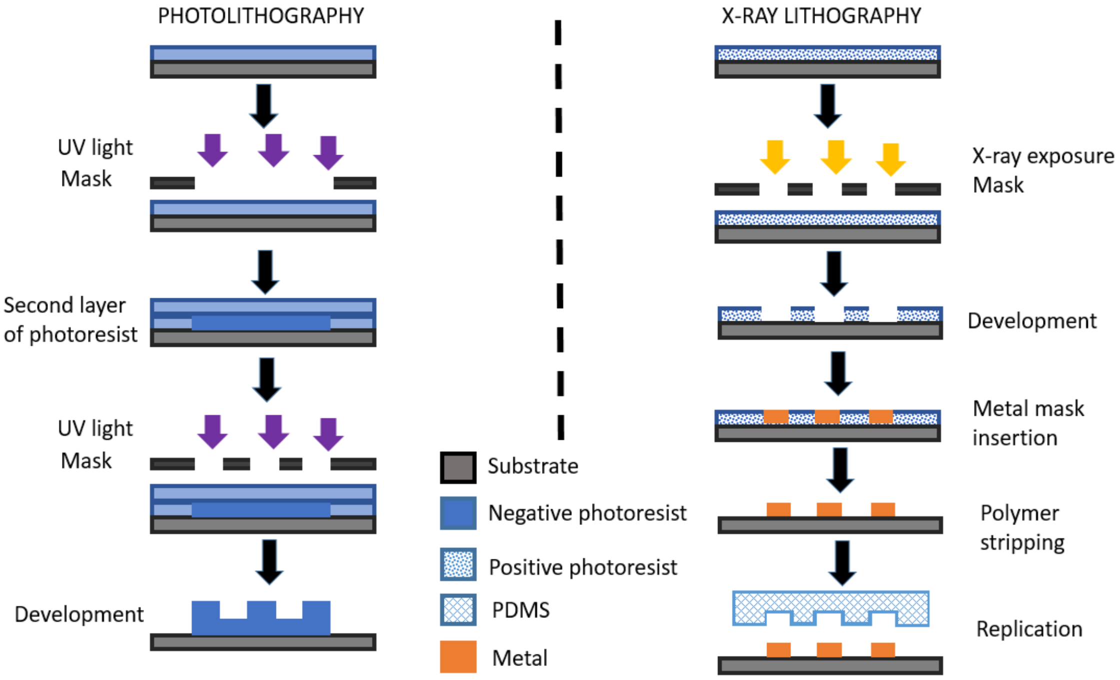

Figure 1.1. Workflow for a typical photolithography process and a X-ray lithography process.

Prototyping techniques. They are designed for the manufacture of low quantities of devices. They are the most used methods “in house” by researchers. The commonly used methods are hot-embossing and soft-lithography. Figure 1.2 shows the manufacturing process in these two cases. In the case of hot-embossing technique, it is based on a master previously manufactured (almost always by optical photolithography) with which the thermoplastic material is brought into contact (using a glass layer as a support). By means of a controlled cycle of pressure and temperature the piece is obtained, which will be closed by repeating another cycle equal to or different from the previous one, placing two pieces of the same material in contact. In the case of soft-lithography the process also starts with a master (also almost always made by photolithography) where the PDMS is poured. Once cured, an oxygen plasma treatment is performed, which modifies the surface and allows the bonding of the piece with glass or another PDMS layer, just applying a light pressure.

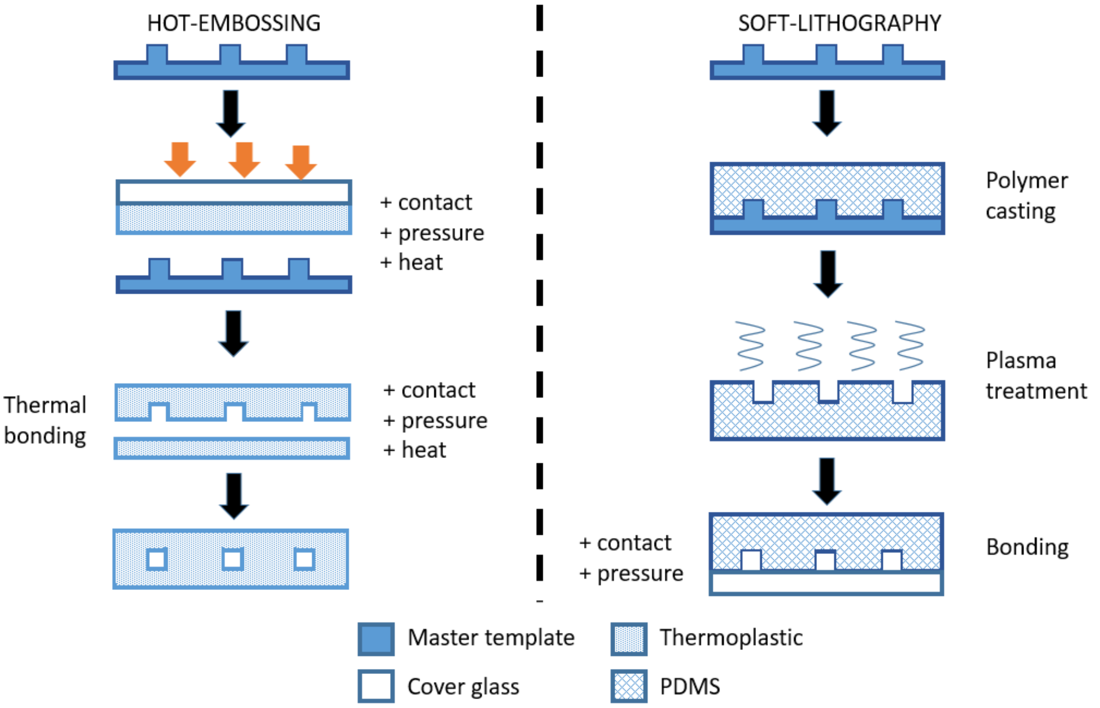

Figure 1.2. Workflow for a typical hot-embossing process and a soft-lithography process.

Mass production techniques. This is the technique used to be able to have large runs at very low prices, using thermoplastic materials. A very simple scheme of the production process is shown in Figure 1.3. In this case, it is necessary to have a mould made by machined steel to obtain the best results. The thermoplastic material is introduced by a process whereby the pellets are heated until a fluid state that is injected on the mould. A cooling system is also necessary to carry out the demoulding process, which is typically performed by the circulation of water or a gas. This is a very basic scheme since the field of plastic injection is very wide and complex with very different techniques depending on the quantity of parts, the type of process and the materials.

In Table 1.2 appears a comparison of the manufacturing methods discussed above showing the main advantages and disadvantages of these techniques.

Methods	**Advantages**	**Disadvantages**
Hot embossing	Cost-effective, precise, and rapid replication of microstructures, mass production	Restricted to thermoplastics, difficult to fabricate complex 3D structures
Soft lithography	Cost-effective, able to fabricate 3D geometries, high resolution (down to a few nm)	Pattern deformation, vulnerable to defect
Conventional photolithography/optical lithography	High wafer throughputs, ideal for microscale features	Usually requires a flat surface to start with, chemical post-treatment needed
X-ray lithography	High resolution to fabricate nanopatterns, absorption without spurious scattering, able to produce straight smooth walls	Difficulties in master fabrication process, time consuming, high cost
Injection molding	Easy to fabricate complex geometry, fine features, and 3D geometries, low cycle time, mass production, highly automated	Restricted to thermoplastics, high cost mold, difficult to form large undercut geometries

Table 1.2. Microfluidic fabrication techniques.

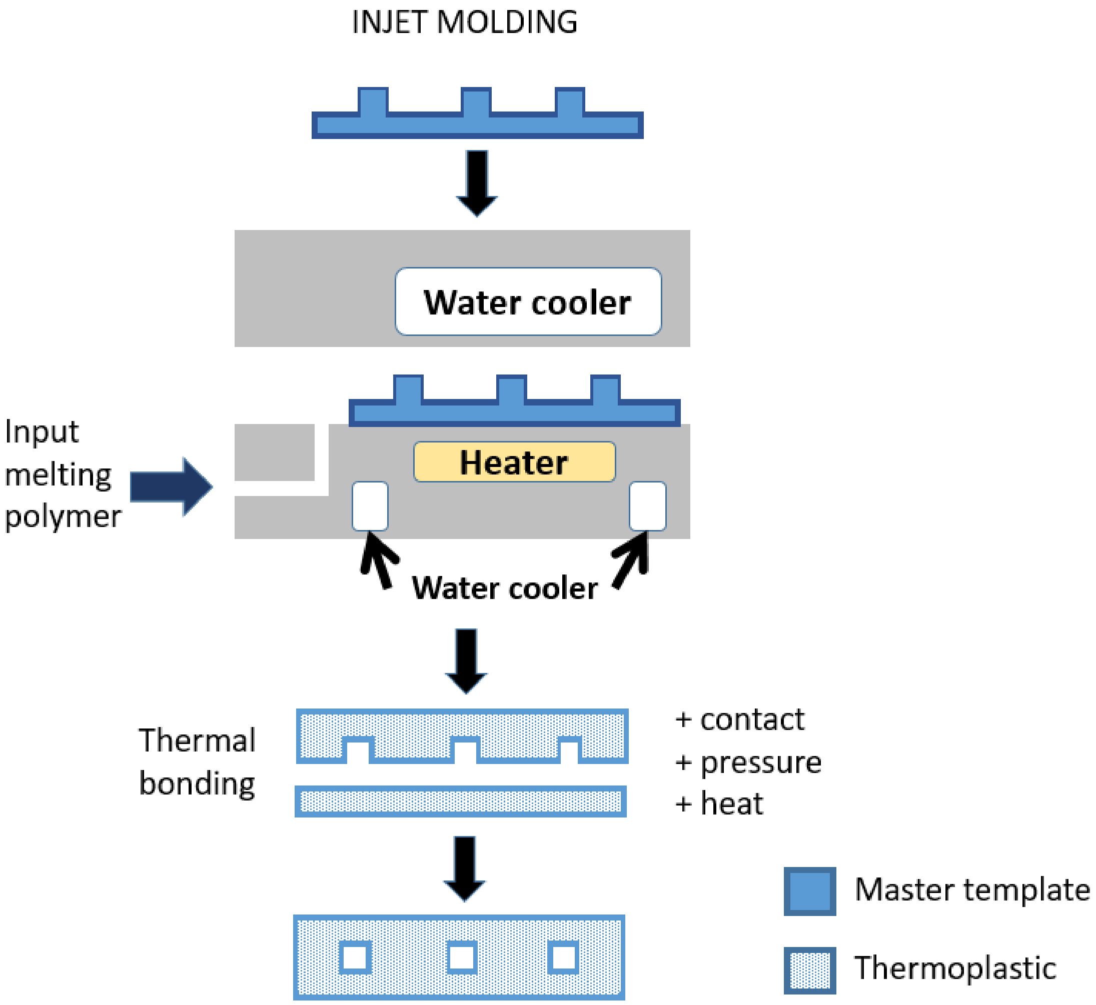

Figure 1.3. Workflow for a typical inject molding process.

1.2.2 Microfluidics for cell culture applications

As mentioned above, for many years, microfluidics has been used more or less widely in fields such as micromechanics or microelectronics, while its use in other fields of application such as tissue engineering or cell culture have a more recent creation. Microfluidics has a number of advantages that are very beneficial for the study of cell culture applications:

- Reduced size: microfluidic devices are designed by a series of channels and cameras with very small dimensions (few hundred microns) which means that the volumes are also very small. This characteristic is of great importance when performing cell cultures because it presents a significant cost savings in the use of reagents, culture media, compounds, etc. It is also a clear saving during the drug development phase, since, at the earliest stages of study, these compounds have a very high price. Its small size is also an advantage in storage within incubators.

- High parallelization: microfluidic devices are not designed to perform a single experiment on each chip, but the parallelization of experiments is sought. This is of vital importance, once again for the development of new drugs, being able to perform high-through output screening in a very simple way.

- Possibility to include stimuli: in the microfluidic devices it is possible to perform mechanical, chemical, electrical stimulation, etc. to the cell cultures that are being carried out inside. These stimuli are vital when we want to have a biomimetic environment. When we speak of biomimetic environment, we refer to all this environment full of stimuli that we are able to recreate in an *in-vitro* way but that results in the cell culture behaving in the most similar way possible as it would in a *in-vivo* . This environment is fundamental to be able to test drugs more quickly and effectively reducing time and costs, studies of new materials for, for example, bone prostheses, study of new food compounds, study of new diseases and the creation of the very fashionable “Organ-on-a-chip ”. With the use of these models, we can reduce the need for animal models for the study of diseases and the testing of drugs and compounds.

- Reduction of human error: since it helps to reduce human handling, analysis using microfluidic devices will reduce the risk of human error compared with classical analytical processes.

- Faster response time: at micrometric scale, diffusion, changes in pH, temperature or flow are faster. This allows, for example, evaluate the effect of a chemical reaction by diffusion in few seconds.

- Real time monitoring: thanks to optical access and the compact design of the devices, the cell culture or the chemical reaction performed in the microfluidic chip can be controlled in real time, leading to more controlled results.

- Expendable: due to the possibility of automation, low energy consumption and low price, microfluidic devices can be also used in an integrated platform for, not only perform a cell culture assay, but also flow controlling, flow actuation (valves and pump), sensoring (glucose, lactate, pH, CO2, O2, etc.) without the need of human intervention.

Cell and environment control

Cells in an in-vivo environment are subjected to a large number of external stimuli such as physical, chemical, electrical and interactions with other cells or tissues. In traditional in-vitro cell culture, these essential stimuli for the correct study of cells cannot be taken into account (or not in the most correct way possible) due to the lack of appropriate tools. The realization of cell cultures in microfluidic devices allows to place the cells in an orderly way, respecting the ordering that they have in the in-vivo environment, allowing co-cultures and, besides, they are able to simulate those stimuli necessary to approach in a realistic way the in-vitro cell culture to in-vivo like way.

To make the environment we are creating as much biomimetic as possible, one of the main factors we have to take into account is the desired cell patterning. The cellular organization determines behaviour like polarity, migration, proliferation and apoptosis. This patterning can be achieved simply within a microfluidic device by chemical or mechanical methods, for example, one part of the device can be modified by making it hydrophobic while another part remains hydrophilic allowing in this easy way to organize the cells with the desired patterning [24]. Another method for ordering within the chip is the design of the device itself. The current fabrication processes allow to obtain structures where the cells can grow in 2D, 3D or in combination of both. Another very interesting design is the gradient. There are many examples reported in which the use of chemical gradients has been used to regulate basic cellular functions such as biological processes such as gene regulation, cancer metastasis [25, 26], cellular chemotaxis, differentiation, immune response and migration. Other methods for obtaining unique organization within the microfluidic device are the insertion of scaffolds or porous membranes. With these methods we can have 3D ordering very simply, in the case of scaffolds, or different cell types separated by porous membranes to recreate interfaces between different tissues. The most innovative method that has risen up in the last years is printing by inkjet. This method is especially interesting for 3D model construction and allows the assembly of heterogeneous tissue structure.

Microfluidic setups

From the advantages discussed above, both the parallelization and the inclusion of mechanical stimuli, it is possible to achieve them by performing complete microfluidic setups. These setups are composed, in their most basic way of working by three components: reservoir, microfluidic chip and pump (Figure 1.4).

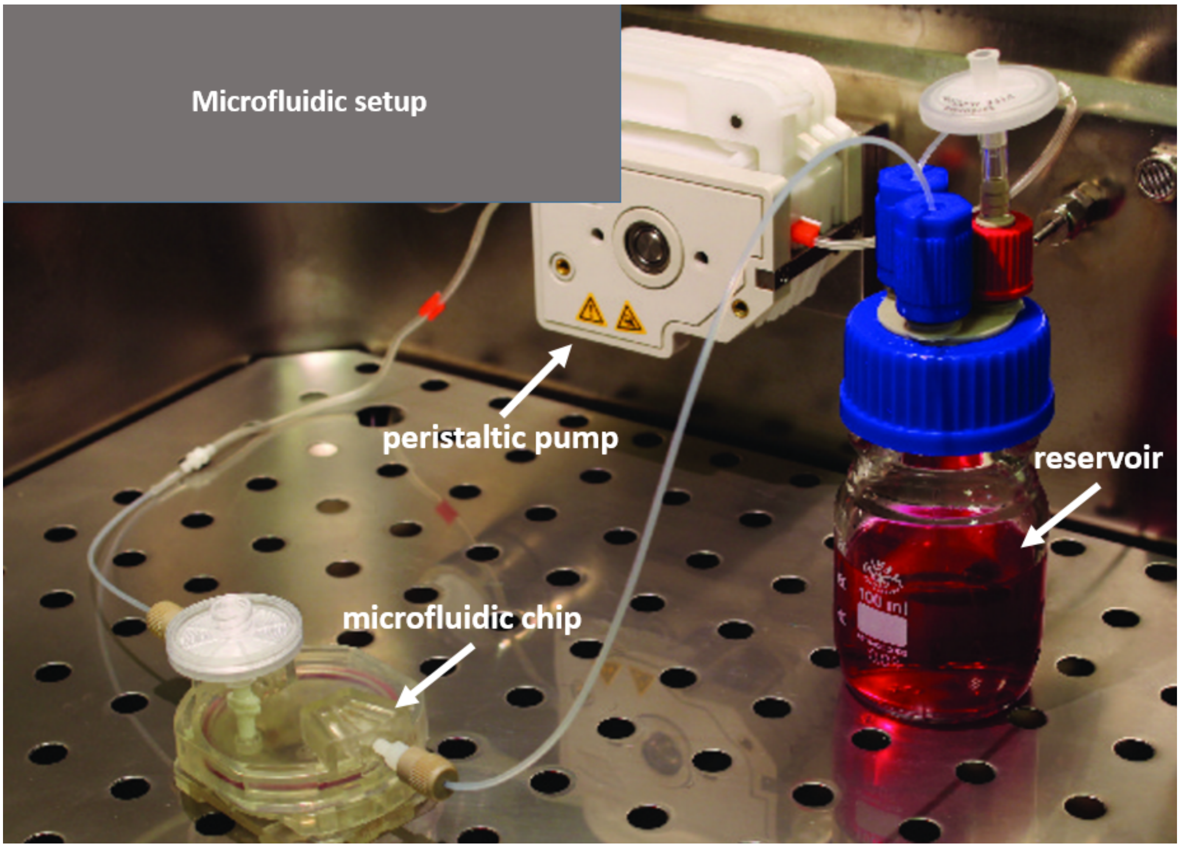

Figure 1.4. Microfluidic setup.

The reservoir is the place where the medium for cell culture is maintained. The culture medium is composed essentially of essential amino acids, serum, vitamins and other compounds necessary for the correct grow of the cell culture. The pump is the external element that allows the culture medium to reach the microfluidic chip, which is where the cell culture is to be performed. There are different types of pumps on the market such as peristaltic or syringe pumps. The third of the elements is what this thesis is about: the microfluidic chip.

The characteristic of small dimensions, not only refers to the internal dimensions of microfluidic chips, but also refers to the external dimensions. For better handling of the devices, these are encapsulated within a dedicated packaging to house the microfluidic chip. This packaging, besides facilitating the handling by the user, also has the purpose of keeping the cell culture isolated from the outside, by means of O-ring seals that make the seal hermetic not allowing the contamination with the exterior, but the optical inspection by microscopy and the correct fluid flow through the cell culture.

Other components: micropums, microvalves and flow sensors

In addition to the microfluidic chips for cell culture, there are a number of active components that are also interesting to miniaturize for incorporation into microfluidic setups: microvalves, micropumps and flow sensors.

Microvalves Microvalves control routing, timing, and separation of fluids within a microfluidic device and are crucial for designs with complex functionality. The interest in the miniaturization of these components lies in the search for reduction of dead volumes, the possibility of supplying precise doses of reagents or their storage. Traditionally, the microvalves can be divided into active or passive, depending on whether there is presence of an actuator or not, having a better performance the active ones than the passive ones. [27–31].

Micropumps As with microvalves, micropumps are control elements of the fluid flow in a microfluidic setup. In this case, micropumps can also be classified in two categories: passive and active. In the case of passive micropumps, these do not depend on any external element for its operation, but that its principle of operation is based on the careful design of the micropump itself and the surface tension and chemistry of the materials that compose them [32, 33]. The main disadvantage of this type of micropump is that the flow is uncontrolled and is often not constant over time. The performance of active micropumps is regulated by an external signal. Although the need to incorporate this external work signal, which increases the complexity of the device, they also allow a precise control of the behaviour of the pump. There are numerous operating principles for this type of micropumps, including the pneumatic membrane micropumps [34, 35], piezoelectric micropumps [36, 37], Braille pin micropumps [38, 39], electrochemical micropumps [40–42] and acoustic micropumps [43–46].

Flow sensors The control of the flow that is going through the microfluidic setup is fundamental in any application of cell culture since it is the flow that determines the shear stress that the cells suffer. A high shear stress could lead to kill our culture for physiological reasons, and an excessively low flow may lead to them not behaving as expected, for example, not de-differentiating into the expected cell type. For other types of applications, it is also interesting, for example, to know the sample volume being dispensed. The flow sensors for very high volumes have been developed with technologies that have not been able to adapt to microfluidic control in all cases, since in this case the really low flows are the most interesting (of the order of tens of microliters /minute).

Depending on the physical phenomenon to which they respond, the flow sensors can be divided into five categories: thermal, mechanical, acoustic, optical and electromagnetic flow sensors. The physical principle used by thermal flow sensors [9, 47] (calorimetric, hot wire and time-of-flight sensors) is based on the punctual heating of a very small mass of fluid. In general, the advantages of this type of sensors are great sensitivity even in very flow rates (under 1 µl / min) and a large measurement range. The main disadvantages are the lack of linearity over their temperature range, the sensitivity to the presence of particles in the fluid, so it is important to perform a cleaning protocol after each use. In addition, the method of measurement depends on the thermal properties of each fluid, so a prior calibration with each fluid change is required. Within the mechanical flow sensors [10, 48–52], it is possible to highlight the Coriolis mass flow sensors (developed within this thesis) although they exist of other types like the ones based on differences of pressure, the deformation of cantilevers or the ones of positive displacement. In general, mechanical flow sensors have a wide measuring range, but in all cases they cannot be used for flows of the l / min range. Acoustic flow sensors are actually ultrasonic flow sensors. The main ultrasonic technology for flow sensing uses the principle that ultrasonic signals propagate faster in the flow direction than in its opposite direction [53].

1.3 Thesis outline

The use of microtechnologies to achieve different microdevices related to cell culture in biomimetic applications is the leitmotiv of this thesis. That is why, in chapter 2 we begin by explaining the development of a microfluidic chip, encapsulated included, for a very specific application such as nanophotonic biosensors. Of all the manufacturing methods presented in this thesis, the one presented here is made on a Si wafer, as a base material. In chapter 3, we present a microfluidic chip made entirely in SU-8 and used successfully for the cultivation of spheroids and single cells and the study of the effect of chemotactic gradient. Another application also linked to 3D cell culture in microfluidic devices, can be found in chapter 4, where a new microfluidic cell culture device compatible with real-time nuclear magnetic resonance (NMR) is presented. The device was designed for, on one hand, allows long-term 3D cell culture, and on the other hand, to fit inside the commercial NMR equipment to obtain the maximum readout resolution. In chapter 5, a novel SU-8 Coriolis flow sensor is presented. As it has been mentioned before in this chapter, biomimetic cell culture needs a very sensitive flow control. Here is a high-accuracy flow sensor that can also detect density changes in the flow. Lastly, some final conclusions are drawn in chapter 6, including thesis contributions.

Chapter 2

Nanophotonic lab-on-a-chip platforms including novel bimodal interferometers, microfluidics and grating couplers

One of the main limitations for achieving truly lab-on-a-chip (LOC) devices for point-of-care diagnosis is the incorporation of the “on-chip” detection. Indeed, most of the state-of-the-art LOC devices usually require complex read-out instrumentation, losing the main advantages of portability and simplicity. In this context, in this chapter last advances towards the achievement of a portable and label-free LOC platform with highly sensitive “on-chip” detection by using nanophotonic biosensors are presented. Bimodal waveguide interferometers fabricated by standard silicon processes have been integrated with sub-micronic grating couplers for efficient light in-coupling, showing a sensitivity of $3.3 \cdot 10^{-7}$ refractive index unit (RIU) in bulk. A 3D network of SU-8 polymer microfluidics monolithically assembled at the wafer-level was included, ensuring a perfect sealing and a compact packaging. To overcome some of the drawbacks inherent to interferometric read-outs, a novel all-optical wavelength modulation system has been implemented, providing a linear response and a direct read-out of the phase variation. Sensitivity, specificity and reproducibility of the wavelength modulated BiMW sensor has been demonstrated through the label-free immunodetection of the human hormone hTSH at picomolar level using a reliable biofunctionalization process.

2.1 Introduction

One of the main challenges of the 21st century is related to human health, including environment monitoring, food safety and early medical diagnostics. These fields share the common need of detecting very low concentration of analytes or toxins in real-time. Traditional techniques, such as ELISA or RIA tests, suffer from important limitations: laborious sample preparation, the need of bulky instrumentation and the slow data processing. Moreover, they often have to be performed by specialized technicians in laboratory environments. To overcome these drawbacks, the implementation of a portable, easy-to-use and highly sensitive biosensor lab-on-a-chip (LOC) for label-free and real-time analysis is mandatory. A LOC must combine, ideally, all the functionalities on a single chip: fluid handling, sample preparation (filtration, homogenization, dilution, etc.), target detection and signal processing. During the last years, the quest for such fast and efficient analytical platforms has attracted the attention of many researchers [54, 55].

When dealing with a biosensor LOC system, the first issue to solve is the choice of the transducer. Even if the validity of electrochemical methods has already been demonstrated for several applications [56, 57], optical detection is generally considered as the most promising method for the development of label-free LOC platforms. In particular, integrated optical (IO) devices are having an increasing impact [58, 59] as they offer high sensitivity, mechanical stability, miniaturization and the possibility of mass-production. They also present the advantages inherent to optical read-outs, *i.e.* non-invasive and non-destructive nature, absence of risk of electrical shocks or explosions and immunity to electromagnetic interferences. In addition, IO transducers have a great potential for parallel measurements making multiplexing detection feasible.

Most of the IO sensors are based on the evanescent field detection principle: the biomolecular interaction between the analyte to detect and the corresponding bioreceptor immobilized on the waveguide (WG) surface within the evanescent field region results in a variation of the refractive index of the WG outer medium. This modification affects the effective index of the wave propagating in the WG which can be detected by measuring the intensity, the phase, the resonant momentum or the polarization of the output signal. In this detection scheme, there is no need for labelling or prior separation of non-specific components making label-free detection feasible. Among the different IO sensors described in the literature or commercially available, it is worthwhile to mention the ones using micro-ring resonators, with a limit of detection (LOD) of $7,6 \cdot 10^{-7}$ refractive index unit (RIU) in bulk and $0,3 pg/mm^2$ in mass surface density,[60, 61] grating couplers (LOD: $2,5 \cdot 10^{-6}$ RIU and $0,3pg/mm^2$),[62] photonic crystals (LOD: $6 \cdot 10^{-4}$ RIU and $2,1pg/mm^2$), [63] Young interferometers (LOD: $8,5 \cdot 10^{-8}$ RIU and $0,02pg/mm^2$) [64] or Mach-Zehnder interferometers (LOD: $1 \cdot 10^{-7}$ RIU and $0,06pg/mm^2$) [65].

However, despite the growing interest of the academic and industrial communities, very few stand-alone LOC platforms based on IO sensors have emerged. Indeed, the transit from bulky and complex laboratory equipments to a small, portable and cheap LOC device with low consumption is still a challenge: even if the technologies for each component are mature, their integration into a single platform is complex. The device must be carefully designed since it is not merely the sum of the basic units.

One key issue in the development of LOC devices is the way to bring the sample in contact with the sensing area. The volume of the sample and the flow rate are critical parameters, especially for clinical testing where it is extremely important to reduce the sample volume. Recent technology efforts to combine the fields of photonics and microfluidics have led to the development of optofluidics, in which optical and fluidic systems are integrated together to provide improved functions and performances. The interest in this field is demonstrated by the increasing number of papers and reviews published during the last years [66, 67].

In the case of IO sensors, the way to couple light into the WG is another critical aspect as an efficient coupling increases the sensitivity of the device through an improved signal-to-noise ratio. Common in-coupling techniques are the end-fired method, the prism coupling and the grating assisted coupling, the last one being the most suitable for future commercial devices as it provides better integration and stability. However, very few publications have demonstrated biosensing capabilities of IO sensors incorporating grating couplers. Exception is made with the multiplexed ring resonator array integrated with microfluidics and grating couplers developed by Carlborg *et al.* [68] or the grating coupled with a WG interferometer recently optimized by Kozma *et al.* [69].

The biofunctionalization protocol is a third aspect which also plays a crucial role in the biosensor LOC performance as it will guarantee the sensitivity, the selectivity, the stability and the longevity of the biosensor. Enormous efforts are continuously invested to develop new strategies adapted to a particular application and to each type of silicon-based photonic sensor [58, 70].

Taking into account all the above described aspects, different attempts have been done to integrate multiplexed IO biosensors into LOC platforms and promising results have been achieved [71, 72]. But these systems still require complex read-out laboratory instrumentation, losing the advantages of portability and simplicity. Therefore, the main difficulty when implementing truly LOC devices for point-of-care platforms remains on the incorporation of real “on-chip” detection.

To solve this gap, we present here our last advances towards the assembly of a LOC platform with “on-chip” detection using a recently developed nanophotonic biosensor, the bimodal waveguide (BiMW) interferometer [73]. In the first part, the working principle and the fabrication processes of the nanometric BiMW will be presented as well as the experimental set-up. Then, the successful integration of several of the required units of a LOC platform will be demonstrated: (i) nanograting couplers for efficient light in-coupling into BiMW interferometers, (ii) a novel all-optical wavelength modulation system to ensure linear response and avoid false read-out, (iii) reliable immobilisation protocols of the sensor surface and the immunosensing of the human hormone hTSH at pM level (iv) a 3D network of SU-8 polymer microfluidics monolithically assembled at the wafer level with the BiMW sensors.

2.2 Bimodal waveguide interferometer

2.2.1 Optical transduction principle

In the BiMW sensor the interference of two WG modes (fundamental and first modes) of the same polarization occurs in a straight WG, without the need of a reference arm [73]. The simplicity of this design using only straight WGs is especially attractive for the implementation of LOC platforms.

As depicted in Figure 2.1a, the light from a coherent source is first coupled (by end-fire method or via a grating coupler) into a rib WG that supports a single transversal mode. After a certain distance, the guided beam reaches a modal splitter that splits the first guided mode in two transversal modes, the fundamental and the first order modes, which are propagating until the output of the chip. A sensor area is defined on the bimodal part of the WG and, as the fundamental and the first order modes have different intensity distributions at the core-cladding interface, the interference pattern is a function of the refractive index in the sensing region. In this scheme, there is no need for Y junctions facilitating the device fabrication as compared to other interferometric configurations. Moreover, the interference pattern does not depend on the light intensity or on coupling variations which are important drawbacks when using Mach-Zehnder or Young interferometers.

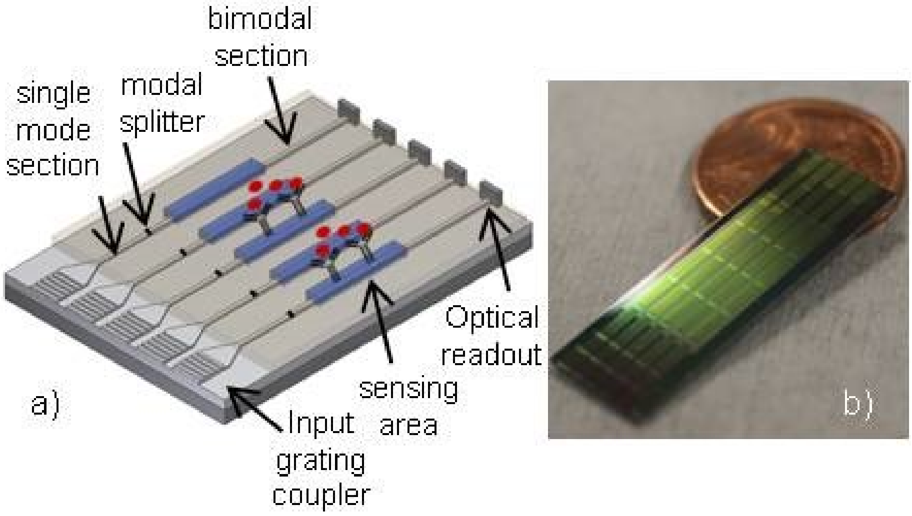

Figure 2.1. (a) Scheme of the BiMW interferometers in a multiplexed configuration, integrated with input grating couplers and photodetectors. (b) Photograph of a chip of $30 \times 10mm^2$ containing 16 BiMW interferometers.

Regarding multiplexing, the small foot-print of the BiMW interferometer allows the integration of a large amount of sensing element within a single chip. For instance, Figure 2.1b shows a chip of $30 \times 10mm^2$ containing 16 BiMW distributed as four groups of four; up to 30 interferometers could be easily integrated in such chip.

2.2.2 Optical chip

To optimize the sensor design, calculations and simulations were previously done as described elsewhere [73]. According to the modelization, lithographic masks and devices were fabricated using standard microelectronics technology. The bottom cladding layer consists of a 2 µm-thick thermally grown silicon dioxide layer (nSiO2 = 1.46 at 658 nm) deposited on a silicon wafer. Then, a 350 nm-thick core layer of silicon nitride (nSi3N4 = 2.00 at 658 nm) is deposited by LPCVD. The thickness of the single mode section is reduced to 150 nm using conventional photolithography and dry etching processes. Once the two different modal sections are defined, the nanometric rib structure of the WG (4 µm in width and less than 1.5 nm in height) is generated by BHF etching through a photoresist mask patterned by photolithography. The top cladding layer, a silicon dioxide layer ($n_{SiO2} = 1.48$ at 658 nm), is then deposited by PECVD. The final wet etching step defines the sensing window ($15 \times 0.05mm^2$) and the 2 mm-long grating window.

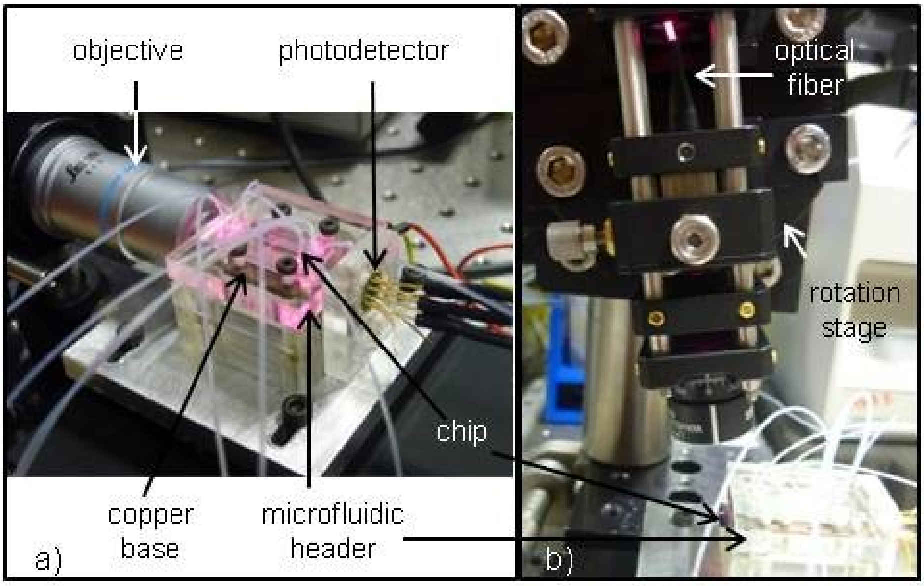

Figure 2.2. Photographs of the set-up based on (a) end-fire method and (b) grating coupler method.

The choice of a standard fabrication process offers important advantages such as robustness, reliability and potential for mass production with consequent reduction of costs. In addition, the integration of light sources, photodetectors and CMOS processing electronics into the LOC platform would be facilitated if needed.

2.2.3 Experimental set-up and procedures

To control the temperature of the chip, a Peltier device, composed of a copper base and a thermo-electric element (TEC 3-2.5, Thorlabs) connected to a temperature controller (TED 200C, Thorlabs), was integrated into a PMMA holder. The whole structure is placed on a XYZ translation stage (NanoMax, Thorlabs, travel range: 4 mm, resolution 1 µm).

For light coupling into the chip, two different methods have been used: end-fire coupling and grating assisted coupling. In the end-fire method, light from a high-power laser diode (ML101J27, Mitsubishi, $\lambda 0$ = 658 nm, 120 mW) is coupled into the WG using a x40 microscope objective (Figure 2.2a). For the grating coupler method, a fiber pigtailed laser diode (LPS-660-FC, Thorlabs, $\lambda 0$ = 658 nm, 7.5 mW) is mounted on a rotation stage placed above the chip to control the incidence angle of the focused beam (Figure 2.2b). In both cases, TE polarization is employed.

Photography of the BiMW chip highlighting the excited grating and the light propagating in the WG.

The interference pattern produced at the output of the BiMW is directly monitored by a two sectional photodiode (S5870, Hamamatsu), each section being connected to a current amplifier (PDA 200C, Thorlabs). The currents generated in the upper and lower part of the photodetector, respectively I_{up} and I_{down}, are function of the interference pattern. To quantify the variation of this pattern, we define the sensor signal S as

$$S(\%) = \frac{I_{up} - I_{down}}{I_{up} + I_{down}} \times 100 \tag{2.1}$$

When a variation of the phase difference $\Delta\Phi_S$ is induced between the two guided modes, for instance by varying the refractive index in the sensing area, it results into an intensity variation of S that can be expressed as:

$$S(t) \propto \cos\big(\Delta\phi_S(t)\big) \tag{2.2}$$

As it can be deduced from Equation 2.2, the output of the BiMW device is periodic with respect to the phase changes induced in the sensing area.

The microfluidic header used for preliminary measurements is a PDMS flow cell encapsulated in a PMMA housing to provide connections to the exterior. The microfluidic header has four independent channels of 3 µl each, one on top of each of the four groups of interferometers.

Prior to biomeasurements, the sensitivity of the device is evaluated measuring the phase changes $\Delta\phi$ induced by refractive index variations Δn in the sensing area. Different concentrations of HCl (from 0.03 to 0.5 M) are injected with running water (milli-Q grade) as buffer using a syringe pump. The refractive indices of the solutions have been previously measured with an ABBE refractometer (Optic Ivymen System). Table 2.1 reports the absolute refractive indices and the index difference induced in the sensing area considering milli-Q water (n = 1.3329) as buffer.

The limit of detection (LOD) of the sensor is then estimated by considering that the lowest detectable phase $\Delta\phi_{min}$ is equal to three times the noise-to-signal ratio. In term of refractive index, the detection limit Δn_{min} is given by $\Delta n_{min} = \Delta\phi_{min}/k$, with k the slope of the calibration curve.

We have previously reported a bulk refractive index sensing using BiMW interferometers of $2.5 \cdot 10^{-7}$ RIU, with a HeNe laser ($\lambda_0 = 633nm$) and end-fire coupling [73]. Our previous result will be used as a reference to compare and estimate the performance of the BiMW device while it is progressively integrated with the required elements of the LOC platform.

Solutions	n	Δn
HCl 0.03 M	1.3332	$3 \cdot 10^{-4}$
HCl 0.05 M	1.3334	$5 \cdot 10^{-4}$
HCl 0.1 M	1.3338	$9 \cdot 10^{-4}$
HCl 0.2 M	1.3348	$1.9 \cdot 10^{-3}$
HCl 0.3 M	1.3357	$2.8 \cdot 10^{-3}$
HCl 0.4 M	1.3366	$3.7 \cdot 10^{-3}$
HCl 0.5 M	1.3376	$4.7 \cdot 10^{-3}$

Table 2.1. Refractive indices of the HCl solutions used for calibration.

2.3 Implementation of the lab-on-a-chip platform

2.3.1 Grating couplers

How to couple light into a WG is an important issue to solve when dealing with LOC based on IO sensors. Our solution is to integrate grating couplers at the input of the BiMW interferometers, making feasible better integration, stability and alignment tolerance than with the traditional end-fire method. Moreover, when coupling light with gratings, no polishing of the chip edges is required.

Due to the sub-micronic cross-section of the WG and to the operating wavelength ($\lambda = 658nm$), the grating length cannot exceed 100 m with a sub-micronic period which makes it suitable for high scale integration. To increase the coupling efficiency, the grating is associated to a tapered WG with an initial width of 20 µm that linearly reduces until reaching the BiMW width (4 µm). The resonant coupling between the guided TE mode and the grating is obtained when the following phase matching condition is verified:

$$\sin\theta = n_{eff} + \frac{\lambda}{\Lambda} \tag{2.3}$$

with θ the incidence angle, n_{eff} the effective index of the guided mode in the BiMW (here $n_{eff} = 1.677499$), m the diffraction order (here $m = -14$), λ the wavelength and Λ the grating period.

Equation 2.3 is used to design gratings with incidence angles ranging from 5º to 15º. This range of angles enables an efficient coupling but, above all, it is an important requirement for the implementation of the complete LOC platform where the different units have to be integrated all together in a minimum of space but without disturbing each other.

Taking into account the above considerations, the gratings are directly written onto the Si3N4 WG by electron beam lithography and reactive ion etching with a period of 450 nm, a duty cycle of 0.5 and a depth of 50 nm. The set-up shown in Figure 2.3b is used to excite the grating. An example of light coupled into a BiMW via a grating is shown in Figure 2.3 ($\theta = 950'$).

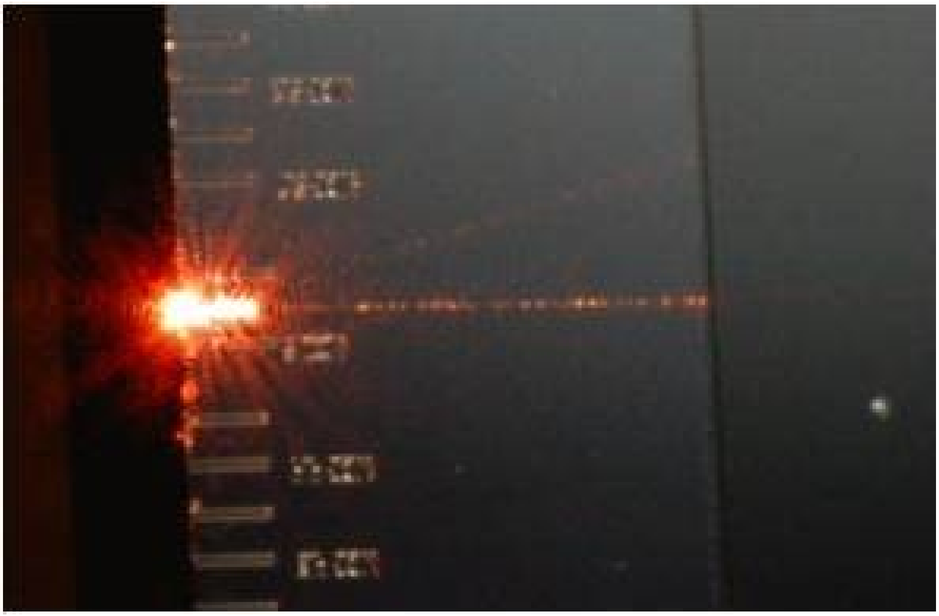

Figure 2.3. Photography of the BiMW chip highlighting the excited grating and the light propagating in the WG.

The sensitivity of the BiMW interferometer integrated with grating couplers is evaluated by carrying out a calibration curve with the set of solutions of HCl (Table 2.1). Figure 2.4a shows the response of the system to an injection of a solution of HCl 0.2 M with milli-Q water as running buffer ($\Delta n = 1.9 \cdot 10^{-3}$): the phase starts at a constant level, corresponding to the running water, then oscillates when the HCl solution reaches the sensing area of the BiMW and finally stabilises. The total phase difference $\Delta\Phi$ equivalent to this change of index Δn is estimated taking into account that an entire oscillation is equivalent to a $\Delta\Phi$ of 2π. Here, the total phase difference for $\Delta n = 1.9 \cdot 10^{-3}$ has been estimated to $3.89 \cdot 2\pi$ rad. The same methodology has been applied to the other solutions and the resulting calibration curve is plotted in Figure 2.4b. A linear fit gives a slope $k = 2008 \cdot 2\pi$ rad/RIU, with R2=0.999. With a noise-to-signal ratio of the system of $2.2 \cdot 10^{-4} \cdot 2\pi$ rad, a detection limit of $3.3 \cdot 10^{-7}$ RIU is achieved. This LOD, obtained with a cheap and easily integrated laser diode, is comparable to the one demonstrated in our previous study using HeNe laser and end-fire method [73]. This strongly supports the adoption of the grating coupler method for the achievement of a truly portable and sensitive LOC platform.

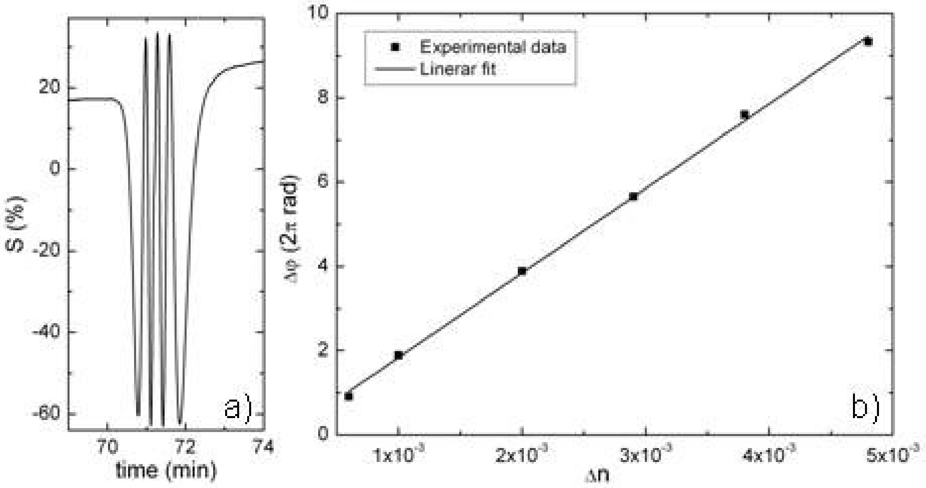

Figure 2.4. (a) Sensor response in the case of an index change of $\Delta n = 1.9 \cdot 10^{-3}$ and (b) calibration curve obtained with a BiMW excited via a grating coupler (TE polarization, $\theta = 950'$).

It has to be noticed that in the case of BiMW interferometers, gratings for light out-coupling are not needed as we opted for a direct monitoring of the signal with a two sectional photodiode directly placed at the WG output.

2.3.2 All-optical phase modulation

An important drawback of interferometric sensors comes from the periodic nature of the output signal which can give rise to wrong or ambiguous interpretations. This problem can be solved by implementing a phase modulation system [74] based for instance on electro-optical [74], acousto-optical [75] or magneto-optical [76] working principles. However, these techniques generally involve not standard CMOS materials and rely on complex read-out equipment which clearly impedes their integration into LOC platform. To overcome these difficulties, we recently have developed an all-optical modulation approach which provides a real-time and direct read-out of the phase variation without additional fabrication processes and instrumentation [77].

In this modulation scheme, the phase difference between the two modes propagating in the BiMW is controlled by tuning few nanometers the input wavelength of the guided light. According to our calculations, a wavelength variation of 2 nm is enough to induce a shift of 2π rad between the two modes. This wavelength variation is easily obtained by taking advantage of a drawback of the commercial Fabry-Perot laser diodes, *i.e.* the dependence of their emission wavelength with the driving current. Therefore, by applying a sinusoidal variation to the laser driving current, it is possible to induce a periodic phase change in the WG. As a consequence of this periodical change, the sensor output defined by Equation 2.2 is now expressed by:

$$S(t) \propto \cos\big(\Delta\phi_S(t) + \mu_M \sin(\omega t)\big) \tag{2.4}$$

where μ_M is the amplitude and ω the frequency of modulation. A Fast Fourier Transform deconvolution of the output signal, performed in real-time with a Labview application, gives a direct read-out of the phase variation [77]. To implement this method, we used the end-fire coupling (Figure2.2a). The 2 nm wavelength shift was obtained with the laser diode ML101J27 (Mitsubishi). Figure 2.5a shows the real-time sensor response during the injection of a solution of HCl 0.2 M with milli-Q water as running buffer ($\Delta n = 1.9 \cdot 10^{-3}$): the phase starts at a constant level, increases when the HCl solution reaches the sensing area and then stabilises. The difference between the two constant levels is the phase difference corresponding to the index variation in the sensing area (here, $\Delta\Phi = 4.17 \cdot 2\pi rad$). With this approach, the phase information is not deduced anymore from the variation of the interference pattern (as the one shown in Figure 2.4a) but is directly monitored, solving all the problems of false read-out responses arising from interferometric signals. In addition, this detection scheme provides a theoretically infinite dynamic range of phase variation.

The phase changes for the complete set of HCl solutions have been evaluated in the same way. As a result, Figure 2.5b shows the calibration curve obtained with a wavelength modulated BiMW (TE polarization, laser driving current: (143 ± 51) mA, modulation frequency: 215 Hz). A linear fit gives a slope $k = 2267 \cdot 2\pi rad/RIU$, with $R^2 = 0.999$. With the standard deviation of the system of 0.002 rad, a detection limit of $4.2 \cdot 10^{-7}$ RIU is obtained. Again, this LOD achieved using cheap, compact and easily integrated laser diode is comparable to our previous results obtained with bulky HeNe laser [73]. This, in addition to the direct phase read-out, clearly promotes the adoption of the all-optical wavelength modulation approach for the implementation of a LOC device.

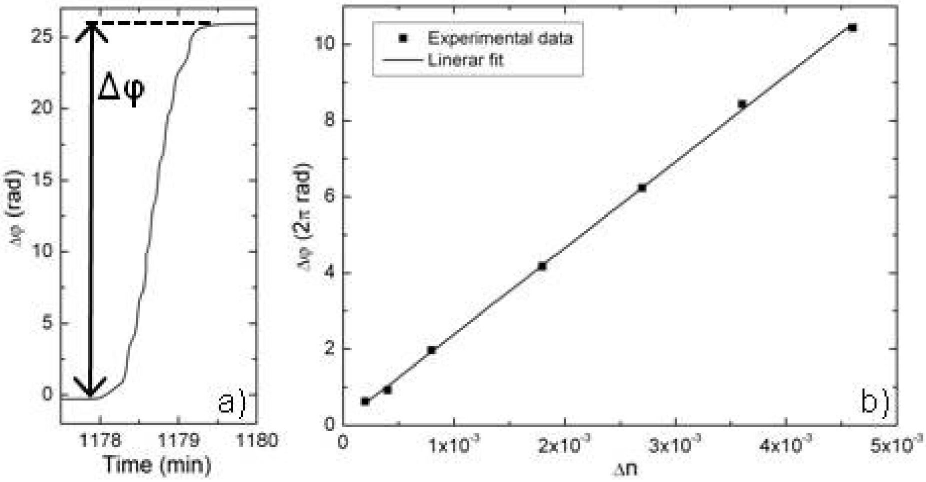

Figure 2.5. (a) Real-time monitoring of the phase variation due to a change of $\Delta n = 1.9 \cdot 10^{-3}$ and (b) calibration curve of the wavelength modulated BiMW (TE polarization, laser driving current: (143 ± 51) mA, modulation frequency: 215 Hz) for different refractive indexes changes.

2.3.3 Biofunctionalization and biosensing evaluation of the wavelength modulated BiMW

The biofunctionalization protocol plays a crucial role in the biosensor LOC performance as the immobilization process should guarantee an efficient coverage of the transducer surface and ensure sensitivity, selectivity and stability of the biosensor. Different immobilization strategies can be employed according to the selected application, *i.e.* to the nature of the bioreceptor to be immobilized. However, one of the most reliable strategies is the covalent binding through one of the chemical group of the molecules [58]. In particular, for proteins, the preferred options are amino, carboxylic or thiol groups. To provide the sensor area with functional groups allowing covalent binding, silane molecules are extensively used.

The implementation of a suitable silanization method involves the optimization of different steps, such as the activation of the silicon surface by oxidation processes and the covalent anchorage of the silane molecule. In order to covalently attach proteins on the BiMW transducer, a carboxyethylsilanetriol sodium salt silane (CTES, abcr) has been used. The formation of a stable and homogeneous monolayer of CTES supplies the silicon surface with carboxylic end-groups. The achievement of an enduring peptidic bond between the carboxylic groups present on the transducer surface and amino groups of the proteins is obtained by the use of 1-ethyl-3-[3-dimethylaminopropyl] carbodiimide hydrochloride (EDC, Sigma-Aldrich) and N-hydroxysulfosuccinimide (NHS, Sigma-Aldrich).

We have selected as a clinical application the detection of the human Thyroid Stimulating Hormone (hTSH), secreted by the anterior pituitary gland. The determination of low concentration of the hTSH is of clinical importance in the case of hyperthyroid syndromes such as thyroid adenoma, nodular goiter or the autoimmune disorder Graves' disease for which hTSH serum levels are below normal ones (normal concentration is considered to be between 2-20 pM). To detect such low level, a competitive immunoassay was carried out with the wavelength modulated BiMW. In a competitive assay, the antigen to detect (here the hTSH) is immobilized on the sensor area surface. Afterwards, an antibody solution of an appropriate concentration is incubated with the sample. The hormone concentration is then detected in an indirect way, by means of the signal obtained by the immunoreaction of the free antibodies in the solution with the immobilised hormones. This procedure implies more time and reagent consumption than direct methods but it allows the reuse of the bioreceptor surface many cycles thanks to regeneration solutions. In direct methods, the antibodies are immobilized on the sensor surface but after the biomolecular interaction, the use of regeneration solutions can easily denaturalize them. In a competitive immunoassay, several detections can be performed using the same bioreceptor layer, reducing the total cost and duration when a complete analytical study is required.

In order to monitor in real time, the interferometric signals obtained by the different steps of the biofunctionalization procedure, the processes are done in situ, with the BiMW chip mounted with the microfluidic header on the experimental set up (Figure 2.2a). During all the functionalization procedure, water flow is maintained at a constant rate of 10 l/min and the different solutions are injected in a volume of 250 l. The generation of reactive silanol groups on the sensor surface is achieved by flowing a 20% nitric acid solution through the microfluidic channels. Three consecutive injections of the oxidizing solution were required to stabilize the interferometric signal. Then, a CTES solution at a concentration of 1% is employed to create a well-package monolayer of silanes. The ended carboxylic groups of the silane are activated afterwards through the EDC-NHS chemistry. The hTSH is then immobilized by covalent bonding by supplying a 10 µg/ml solution of hTSH in phosphate buffer saline (PBS, 10 mM phosphate, 2.9 mM KCl, 137 mM NaCl, pH 7.4, Sigma-Aldrich). The hTSH solution is injected twice, to assure the total covering of the surface by the proteins. Finally, a solution of ethanolamine (Sigma-Aldrich, 1 M, pH 8.5, Sigma-Aldrich) is injected in order to react with activated carboxylic groups, protecting the surface against unspecific adsorption. The buffer is then changed to PBS that is maintained during all the experiments at a constant rate of 20 l/min. Different solutions of the specific monoclonal antibody of hTSH, the anti-hTSH, are injected, with concentrations ranging from 0.5 to 5 g/ml. Regeneration of the biosensing surface is achieved by means of an injection of a HCl solution (20 mM). The resulting calibration curve, expressed as the phase variation as function of the anti-hTSH concentrations, is shown Figure 2.6a.

Highly specific signals have been obtained as can be deduced form the control experiment presented in Figure 2.6b: the injection of a concentration of 5 g/ml of anti-hTSH produces a phase variation of $1.22 \cdot 2\pi$ rad while an injection of 5 g/ml of the antibody against human growth hormone (anti-hGH), the control antibody, does not induce significant phase variation, demonstrating the high selectivity of the immunoassay.

According to the above results, a fixed concentration of anti-hTSH of 1 g/ml has been chosen to perform a competitive immunoassay. A 1 g/ml solution of anti-hTSH is thus incubated with a 1 ng/ml hTSH solution and injected on the sensor surface. The results are shown in Figure 2.7: the injection of 1 g/ml of anti-hTSH induces a phase difference of $0.31 \cdot 2\pi$ rad while the injection of the incubated solution of 1 g/ml of anti-hTSH with 1 ng/ml of hTSH produces a phase difference of only $0.14 \cdot 2\pi$ rad. This detection corresponds to a concentration of hTSH of 20 pM. However, given the significant phase difference between the two signals, lower concentrations should easily be detected once the competitive assay protocols in situ will be further optimized.

Regarding reproducibility, the detection of anti-hTSH 1 g/ml has been repeated three times. The sensor response was similar for the three evaluations: a standard deviation of $0.03 \cdot 2\pi$ rad was found for a mean value of $0.29 \cdot 2\pi$ rad.

These results, obtained with a new wavelength modulated BiMW interferometer, are promising as they clearly demonstrate a high sensitivity, reproducibility and specificity.

2.3.4 Microfluidics and Packaging

In order to integrate a dedicated microchannel on each of the 16 sensors contained in each single chip, SU-8 based microfluidic technology was applied [78, 79]. Figure 2.8 includes the schematic process flow used for the fabrication of the microfluidics devices. The process starts with the spinning of a 20 µm thick SU-8 layer, followed by a soft-bake step (7 minutes at 90º C). Then, another layer is spun and soft-baked in the same way to end up with a 50 µm thick layer (Figure

2.8a). The increased thickness from the expected 40 µm thick layer is caused by the difference in surface friction: while the first SU-8 layer is spun on top of silicon oxide, the second SU-8 layer is spun on top of SU-8 material, increasing the final thickness. Once the final 50 µm thick layer is obtained, an exposure of 140 mJ/cm^2 ultraviolet light (365 nm wavelength) is applied using a mask which defines 100 m-wide microchannels. Then, a post-bake step is performed (4 minutes at 95º C) followed by a gentle development during 4 minutes to remove the unexposed SU-8 (Figure 2.8b). At this point, open microchannels are defined on top of every WG present on the chip. Since any debris deposited on top of the silicon nitride will dramatically decrease the resolution of the sensor, an oxygen plasma step was included as an extra cleaning step (100 watts and 50 sccm oxygen flow during 1 hour). The wafer was then measured by AFM to confirm that the silicon nitride sensing areas were completely SU-8 free.

To close the microchannels, another wafer with kapton on top was processed to carry a 40 µm thick SU-8 layer (Figure 2.8c). This layer is meant to be the cover of the channels with the inlets and outlets already patterned by photolithography (Figure 2.8d). After the alignment of both wafers, a bonding step using a pressure of 3 bar at 90º C during 30 minutes (Figure 2.8e) was performed. The exposure and post bake conditions used in combination with the pressure and temperature chosen for the bonding step allowed the achievement of a perfect bonding with no deformation of the microchannel dimensions [80, 81]. The kapton wafer was then manually released from the silicon wafer thanks to its low adhesion to SU-8 (Figure 2.8f). As a result, the microchannels were finally closed with inlets and outlets accessible from the top of the wafer (Figure 2.9a) [80, 81]. Due to the high density of microchannels present on the chip, the device and the packaging were designed to use one dedicated inlet for each microchannel (Figure 2.8b), but a common outlet for every four sensors (Figure 2.8c). In this way, only 20 fluidic connections between the chip and the packaging were required to handle the device (instead of 32). As a result, the microfluidic connection between the outside and the sensor was done by the use of standard fluidic connectors and O-rings, ensuring a perfect sealing (Figure 2.8d).

2.4 Conclusions and perspectives

We are implementing a sensitive, affordable, hand-held and portable device for point-of-care diagnosis of relevant analytes. Our LOC platform is based on an innovative BiMW interferometer which has already shown its capabilities for sensitive, label-free and real-time biosensing. In contrast to most IO biosensors, the design of our interferometer is simple, allowing easy fabrication processes and integration.

Light in-coupling into the nano-interferometers using grating couplers has been achieved, leading to a limit of detection of $3.3 \cdot 10^{-7}$ RIU in bulk. A wavelength modulation system has been implemented in order to simplify data read-out and to solve some of the problems inherent to periodic signals. In addition, a versatile silanization method for surface biofunctionalization has been implemented and the detection of 20 pM of hTSH has been successfully demonstrated, showing high sensitivity, reproducibility and specificity. Regarding the microfluidic platform, a 3D microchannel network in SU-8 was fabricated at the wafer-level, ensuring a perfect sealing.

Our system presents a high degree of integration as sub-micronic structures are employed in combination with compact laser diodes and simple read-out instrumentation. An additional advantage of our device lies in the use of standard silicon technologies together with polymer material processing, which could allow mass production with consequent reduction of costs.

Work is in progress to evaluate the surface sensing limit of detection of the wavelength modulated BiMW integrated with the grating couplers and the SU-8 microfluidic platform. Moreover, BiMW interferometers are currently being implemented in a multiplexed configuration, taking advantage of the individual inlet of the microchannel network to functionalize individually each BiMW sensor. The final prototype will incorporate the individual components presented here, plus commercial laser diodes, photodetectors, control electronics, firmware and software, sensor read-out algorithms and user interface.

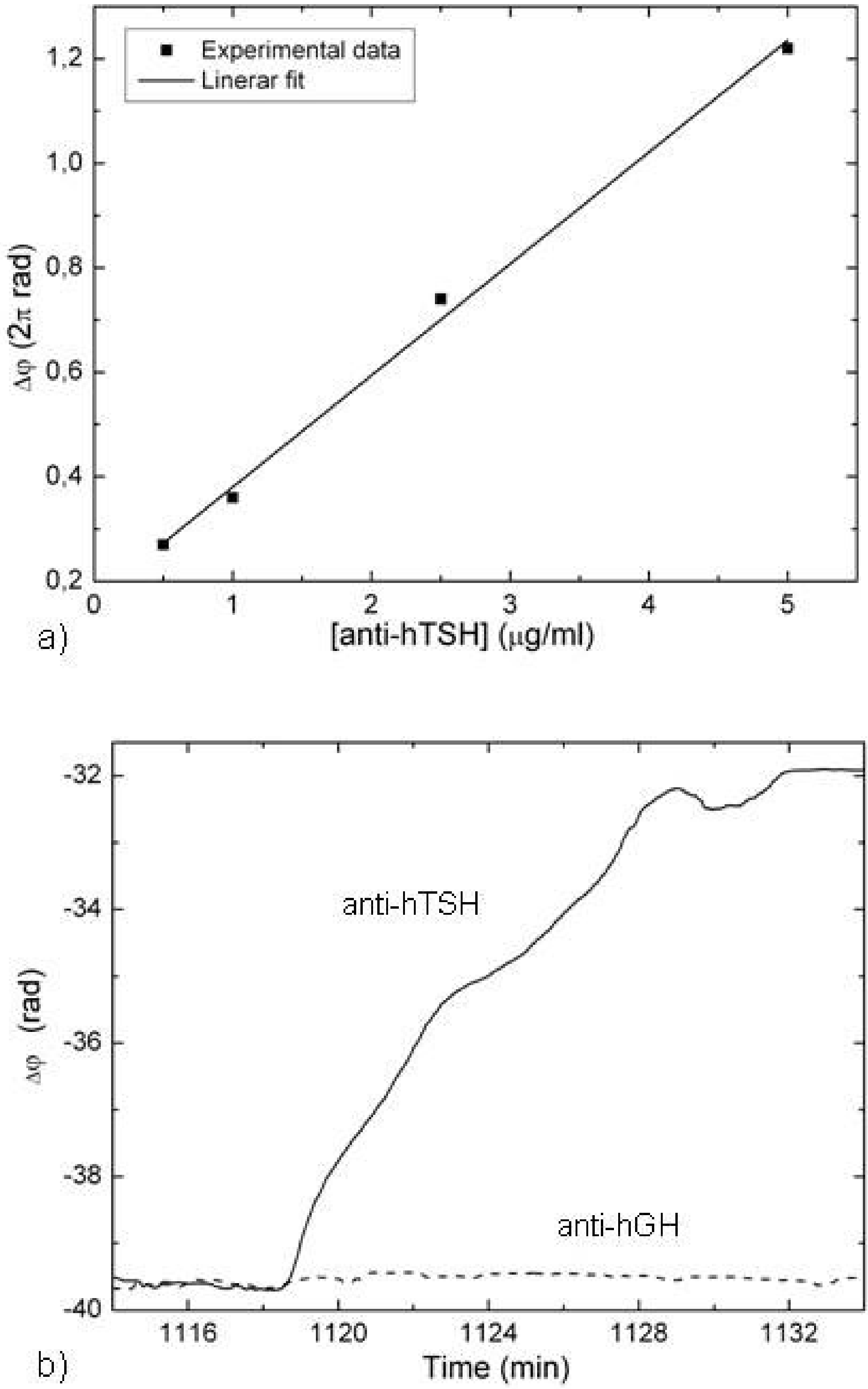

Figure 2.6. (a) Calibration curve for the detection of different concentrations of anti-hTSH. (b) Control experiment: real-time monitoring of the phase variation for the detection of anti-hTSH 5 μg/ml and of anti-hGH 5 μg/ml employed as control. Results obtained with a wavelength modulated BiMW sensor (TE polarization, laser driving current: (143 ± 51) mA, modulation frequency: 215 Hz).

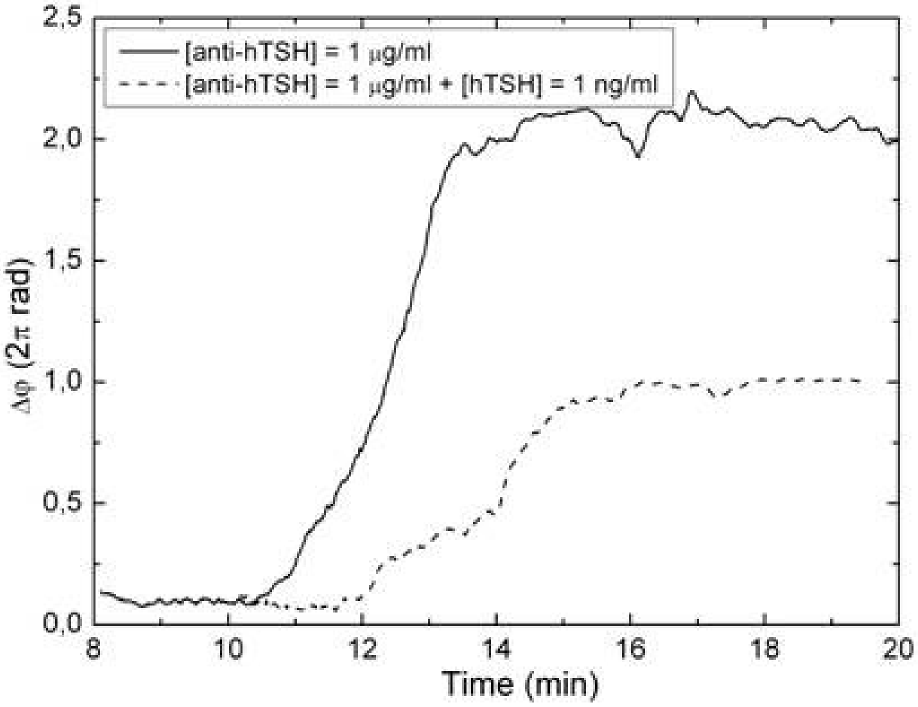

Figure 2.7. Competitive assay: real-time monitoring of the phase variation for the detection of 1 μg/ml of anti-hTSH (solid line) and for the indirect detection of hTSH (1 μg/ml of anti-hTSH + 1 ng/ml of hTSH) (dashed line).

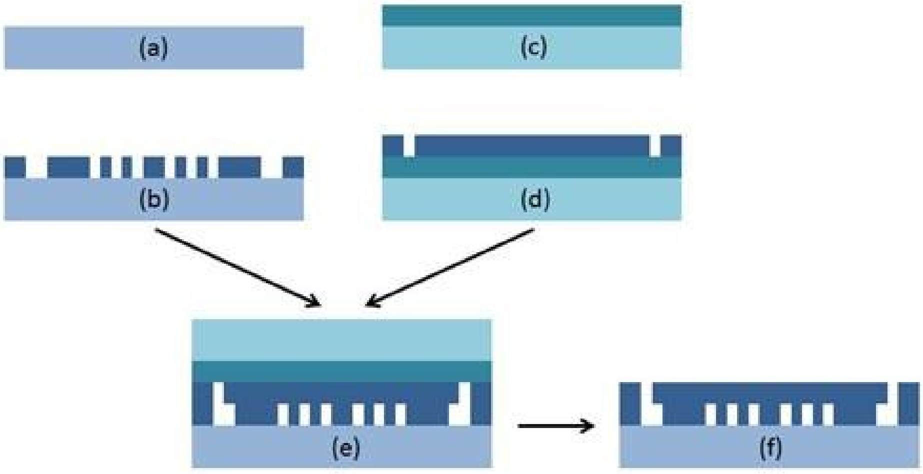

Figure 2.8. CMicrochannel fabrication process flow: (a) spinning of SU-8 to reach a 50 μm thick layer, (b) microchannel definition using photolithography, (c) kapton wafer with a 40 μm thick SU-8 layer on top (d) Cover definition by photolithography, (e) bonding step, (d) kapton wafer release.

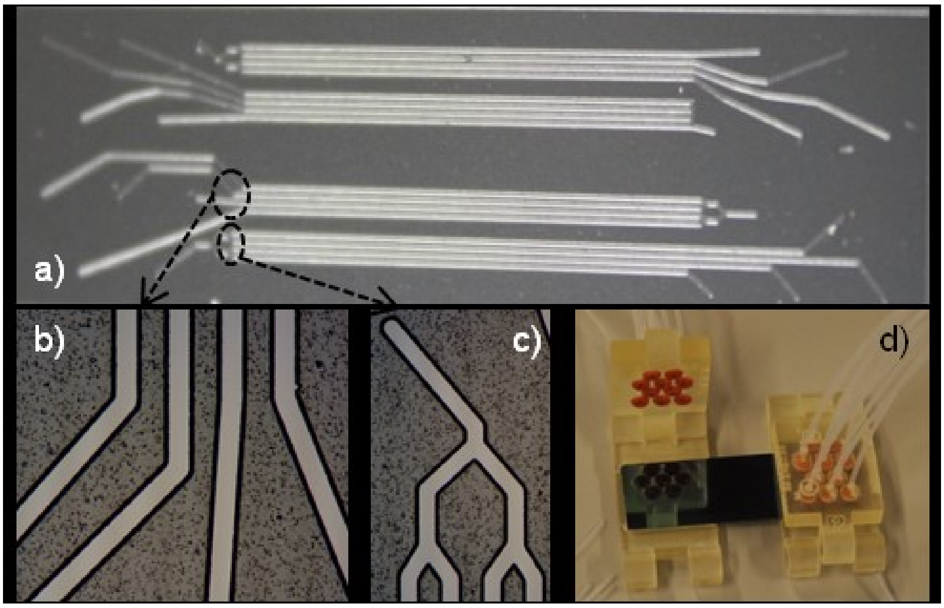

Figure 2.9. Optical images of the 3D SU-8 microfluidic network: (a) BiMW chip with 16 channels, one on top of each sensor, (b) individual inlets of 4 sensors (c) common outlet of 4 sensors and (d) final encapsulation.

Chapter 3

Study of the chemotactic responses of multicellular spheroids in a microfluidic device.

In this chapter, the first application of a microfluidic device to observe chemotactic migration in multicellular spheroids is presented. A microfluidic device was designed comprising a central microchamber and two lateral channels through which reagents can be introduced. Multicellular spheroids were embedded in collagen and introduced to the microchamber. A gradient of foetal bovine serum (FBS) was established across the chamber by addition of growth media containing serum into one of the lateral channels. We observe that spheroids of oral squamous carcinoma cells OSC-19 invade collectively in the direction of the gradient of FBS. This invasion is more directional and aggressive than that observed for individual cells in the same experimental setup. In contrast to spheroids of OSC-19, U87-MG multicellular spheroids migrate as individual cells. A study of the exposure of spheroids to the chemoattractant shows that the rate of diffusion into the spheroid is slow and thus, the chemoattractant wave engulfs the spheroid before diffusing through it.

3.1 Introduction

Chemotaxis is the process by which cells migrate against a concentration gradient towards a chemoattractant. Chemotaxis plays a critical role in many pathologies, including inflammatory [82–84], autoimmune diseases [85] as well as cancer [85–88] and many developmental and tissue remodelling processes, including embryogenesis and wound healing [89, 90]. Therefore, techniques that enable detailed scrutiny of the chemotactic process are important tools for drug discovery as well as basic biology.

A number of different protocols are used to study cell migration and chemotaxis. Boyden chamber [91] has been one of the most popular assays to study chemotactic response for many years,. However, this system as versatile it is, has some limitations, like direct observation of cells during migration processes is impossible. Different techniques have been developed to monitor cell movement in chemotactic experiments: the under-agarose gel [92], agarose spot [93], Zigmond chamber [94], Dunn chamber [95], and Insall chamber [96] assays. Although each of these assays has its own merits, they generally do not allow gradient monitoring over time, and in addition, gradient control and reproducibility can be challenging. Many of these shortcomings can be overcome by using microfluidic systems that have come to the fore as powerful tools to study chemotaxis [97–99]. A large variety of microdevices have been designed to generate chemotactic gradients, and one of the most well-known is the Premixer Gradient Generator based [100]. This microdevices relies on microchannels that split and recombine several times two different liquids in order to generate the desired gradient. Other common designs to generate molecular gradients are based the use of microjets; in such microdevices molecules are transported by convection to the culture area, where diffusion dominates over convection and leads to the gradient generation [101]. The microdevice presented here belongs to other type of gradient generators based on porous hydrogel membranes. Hydrogels posses pores which oppose high resistance to liquid flow, however molecules can diffuse passively through this pores. Therefore, microdevices designed with a chamber to allocate a hydrogel, flanked by lateral microchannels to perfuse different media, have been proved as robust tools to generate gradients and study cell response [102, 103].

Whilst observations of single cell migration with the existing techniques are very useful, they are in some way distanced from more realistic cell migration scenarios, in which cells are part of a multicellular system. Many reports have shown that solid tumour cells can migrate and invade by different mechanisms than individual cells [104, 105]. For example, gliomas are examples of isolated invading tumours, versus epithelial tumours that seem to invade by collective movements [104, 106]. With this differences in mind, is important to consider that to date, none of the previously described assay protocols allow the study of collective cancer cell migration in response to chemotactic gradients, leaving a major gap in our understanding of the process. Here we present a microfluidic device of simple design that permits real time observation of multicellular spheroids embedded in a hydrogel. Moreover, it allows the study of their chemotactic behaviour under conditions generated by introduction of a chemoattractant gradient through lateral microchannels. We directly compare the migration of multicellular spheroids embedded in collagen in a microfluidic system to those in a multiwall plate. We will show, that in response to chemotactic gradient, epithelial squamous cancer cells behave differently, when cultured as isolated cells, then as multicellular spheroids. This is the first example of such an investigation utilising a microfluidic device.

3.2 Materials and methods

3.2.1 Microdevice design and fabrication

In order to easily accommodate multicellular spheroids, microdevices were designed with 400 m diameter inlets and with 400 m wide and 300 m high microchannels. The central microchamber is 1000µm wide and 300µm high. Microdevices were fabricated using SU-8 photolithography combined with an SU-8 to SU-8 bonding process [107].

The main part of the chip is the 1 mm^2 central chamber. The chip was designed for the insertion of cells through the 200 µm wide microchannel located in the middle of the chip. Two extra 200 µm wide microchannels were designed to be at the sides. These lateral channels are connected to the central chamber by narrow fluidic connections (50 µm wide) as it can be observed in the detail of Figure 3.1. These lateral microchannels therefore ensure the supply of nutrients and oxygen by diffusion. Finally, the external chip dimensions were designed to be 10 mm by 10 mm, allowing the integration of all required elements (culture chamber, diffusion channels, 3 inlets and 3 outlets), and the fabrication of 52 devices within a single wafer run.

For the fabrication of the microfluidic chip, SU-8 based technology was applied. Figure 3.2 includes the schematic process flow used.

The process starts with the temporary bonding of a thin kapton film (125 µm) on top of a pyrex substrate (Figure 3.2.a). Kapton was used because of its low adhesion to SU-8, allowing the releasing of the devices from the substrate when their fabrication is finished. Once the kapton film was fixed to the substrate, a 60 µm thick SU-8-50 layer was deposited on top of it. After every spinning

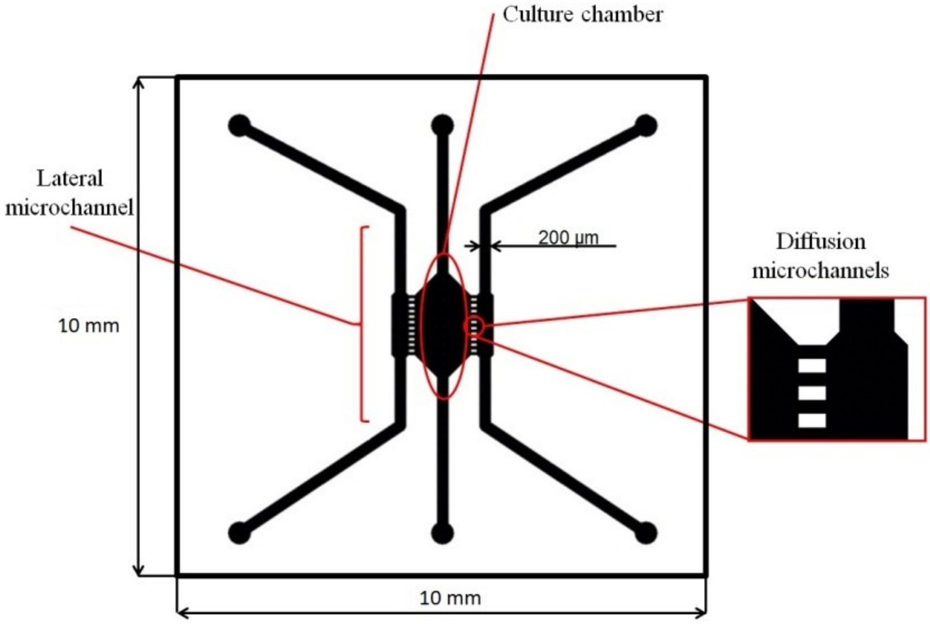

Figure 3.1. Schematic drawing of SU-8 based microfluidic chip.

step, a soft-bake treatment was performed. All soft-bake steps were performed by heating the wafer up to 65º C for 30 minutes, followed by a cooling step down to room temperature. Then, another spinning of a 20 µm thick layer was performed followed by a new soft-bake step. As a result, a 90 µm thick layer was obtained (Figure 3.2.b). The increased thickness from the expected 80 µm was caused by the difference in surface friction: the first layer was spun on top of a kapton film, while the second was spun over SU-8 material, increasing its expected thickness. Next, a 140 mJ/cm^2 exposure dose was used to pattern the floor layer of the device using a 365 wavelength lamp, followed by a post-bake step, heating of the wafer up to 65º C for 15 minutes and cooling it down to room temperature. After this step, two layers of 60 µm and one of 20 µm were spun followed by a soft-bake process (Figure 3.2.c). An exposure of 140 mJ/cm^2 was then applied using the mask which defines the microchannels and chambers. Then, a post-bake was performed followed by a development step to remove the unexposed SU-8. The development consisted on an immersion of the exposed wafer into a SU-8 developer for 8 minutes, followed by a rinsed in isopropanol, DI H2O and a drying step using nitrogen (Figure 3.2.d). As a result, open microchannels with half of the total desired height were fabricated. To close the microchannels and chambers reaching the required height, another wafer was processed. First, a 90 µm thick SU-8 layer was processed (spun and soft-baked) on top of another kapton film temporary bonded to a pyrex wafer (Figures 3.2.e and 3.2.f). Inlets and outlets were patterned by photolithography

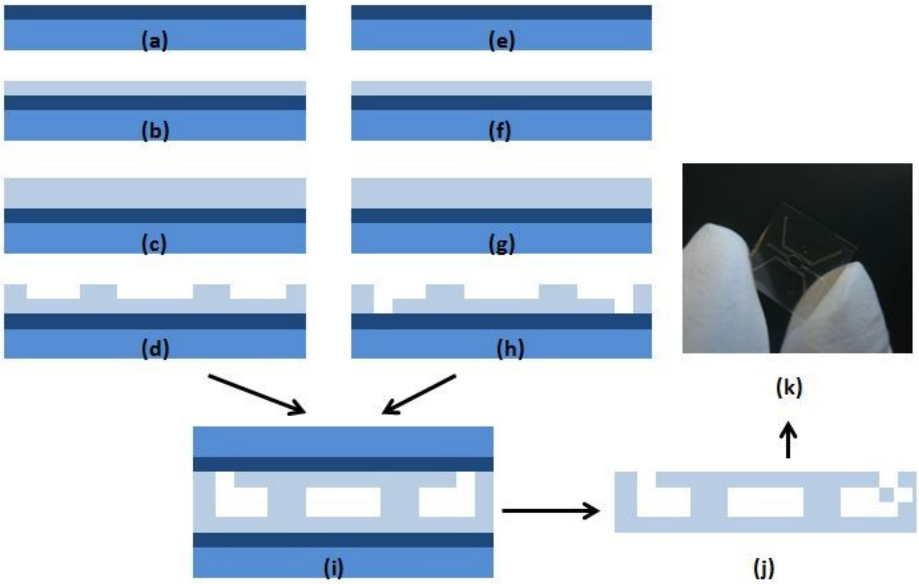

Figure 3.2. Chip fabrication process flow: (a) kapton film bonding to a pyrex wafer, (b) spinning of a 90 µm thick SU-8 layer, (c) spinning of the layer for chamber and microchannel, (d) chamber and microchannel definition by photolithography, (e) kapton film bonding to a pyrex wafer (f) spinning of a 90 µm thick SU-8 layer, (g) spinning of the layer for chamber and microchannel, (h) cover, channels and chamber definition by photolithography, (i) SU-8 to SU-8 bonding, (j) SU-8 device release and k finished SU-8 microchip.

using the same exposure and baking parameters. Next, 180 µm thick layer was processed on top. This final layer was patterned using the mask which defines the microchannels and chambers (mirrored with respect to the step described in Figure 3.2.d), followed by a post-bake step (Figure 3.2.g). The wafer was finally developed (Figure 3.2.h). Then, both wafers (the bottom and the cover) were aligned and bonded to each other applying a pressure of 1 bar and a heating up to 90º C (Figure 3.2.i). Finally, the bonded SU-8 devices were manually released from the kapton thanks to its low adhesion (Figure 3.2.j). The final thickness of the device was sufficient to be rigid enough for its easy handling, even though there is no substrate.

A picture of a finished chip can be observed in Figure 3.2.k.

3.2.2 Cells and reagents

Human oral squamous cancer cell line OSC-19 [108] was a generous gift from Dr Faye Johnson, MD Anderson Cancer Center, Houston, USA. Human glioblastoma cell line U-87 MG was purchased from American Type Culture Collection

(ATCC; LGC Standards, Middlesex, UK). Prior to use, both cell lines were maintained as monolayers in RPMI 1640 growth media (R7388) supplemented with 10% (v/v) foetal bovine serum (FBS), 1 mM sodium pyruvate (S8636) and 2 mM L-glutamine (All from Sigma–Aldrich, Dorset, UK). For the remainder of the manuscript, RPMI 1640 growth media supplemented with FBS is referred to as "complete" whereas RPMI 1640 growth media not supplemented with FBS is referred to as "incomplete". When required, cells were trypsinized and used as suspension in growth media.

Fluorescein diacetate (FDA) (Sigma F7378), Rhodamine B (Sigma, R6626) propidium iodide (PI) (Sigma P4170), Cascade Blue®-10 kDa and Tetramethyl-rhodamine (TRITC)-70 kDa dextrans (Life Technologies, D1976 and D1818) were used as solutions in phosphate-buffered saline (PBS) (Lonza BE17-516F). PBS 5X was prepared dissolving of 1 pack of PBS powder (Sigma P3813) in 200 ml deionised water.

3.2.3 Spheroid generation

OSC-19 and U-87 MG multicellular spheroids were generated using the hanging drop method [109] and methylcellulose [110]. Briefly, 12 g of high viscosity methylcellulose (Sigma, M0512) were dissolved in one litre of RPMI1640, and centrifuged at 4000 g for 2.5 hours. Only the clear supernatant was used in the next step. Cell suspension (10^5 cells/ml) and this methylcellulose solution were mixed in a 4:1 v/v ratio, and 25 µl droplets ($2x10^3$ cells) were placed on the lid of Petri dishes. Sterile water was placed on the bottom of the dishes to prevent evaporation from droplets, the lids were replaced and the Petri dishes incubated at 37ºC and 5% CO2. After 1 day, a single well-defined spheroid was generated per drop. To ensure the response of the spheroids only depends on exposure to external chemotactic gradient of FBS, traces of serum were washed off the spheroids prior to the experiments by washing with incomplete RPMI. To do this, each spheroid was transferred to a single well from a flat bottom 96 multiwell plate with 200 µl of incomplete media and allowed to stand for 30 minutes. The spheroid diameters were 248±18 µm for OSC-19 and 236±5 µm for U-87.

3.2.4 Preparation of the microdevice and multiwell plates

15.4 µl of collagen type I (4.88 mg/ml, Corning 354236), 0.37 µl of aqueous NaOH (1N, Sigma 655104), 4 µl of PBS 5X were mixed and added to a suspension of fifty spheroids in 30 µl of incomplete media. The final concentration of the collagen in this stock mixture is 1.5 mg/ml. The spheroid suspension in collagen was injected into the microdevice, and 5 µl of spheroid suspension were placed on top of the inlet to prevent hydrogel evaporation during polymerization. The microfluidic device was then placed into an incubator (37°C, 5% CO2) for 15 minutes to allow collagen polymerization. For embedding of individual cells, a similar procedure to the one described above was used to obtain a hydrogel mixture, in this case a cell suspension of 2x10^3 cells/ l was mixed with the collagen mixture and injected into the microdevice.

3.2.5 Gradient visualisation

FDA (5 g/ml), Rhodamine B (1 g/ml), PI (4 g/ml), 10 kDa dextran (10 M) and 70 kDa dextran (10 M) were pipetted into one of the lateral microchannels whilst PBS was perfused on the other one. To visualize gradient evolution, time-lapse confocal microscopy images were taken.

3.2.6 Chemotaxis experiments

Chemotaxis experiments were performed within the SU-8 based microdevices (Figure 3.3.a). “Complete” growth media (supplemented with 10% FBS) was perfused through one lateral microchannel, whereas incomplete growth media (not supplemented with FBS) was perfused through the opposite side (Figure 3.3.b). Microdevices were observed on the microscope with temperature and CO2 control systems, conditions were set at 37ºC and 5% CO2 respectively. Brightfield images were taken every 5 minutes.

3.2.7 Imaging and analysis

To assess cell viability and visualize the gradient, confocal images were taken using a Nikon Eclipse Ti microscope equipped with a C1 modular confocal microscope system. Images were collected at different focal planes (300 µm in the “z” direction with 10 µm steps) within each microdevice and multiwell plate control. In order to analyze cell viability a “Z” projection was performed using Fiji® maximum intensity projection algorithm. Isolated cell migration was tracked and quantified using the Fiji manual tracking plugin, whereas OSC-19 spheroid migration was quantified by measuring manually the spheroid occupied area at different times. This spheroid occupied area was drawn to show the collective invasion under the different chemotactic conditions.

3.2.8 Statistical analysis

Experiments were repeated at least three times. OSC-19 invasion results are presented as mean ± standard error. Statistical analysis was performed using SPSS software, and statistical significance was set at $p < 0.05$. The normal distribution was tested by the Kolmogorov-Smirnov test and for nonparametric comparisons the U-test of Mann-Whitney was used.

3.3 Results and discussions

Spheroids are viable inside the microfluidic device. We compared the viability of cells within the spheroids inside the microfluidic device to those in a multiwell plate 24 hours after implantation, by treating both with FDA/PI solutions to detect viable and dead cells. We observed that spheroids within the microdevice remained intact during injection within the microdevice. Cell viability was measured in those spheroid located within the microdevice as well as in those placed in multiwall plate. Results showed more than 95% of the cell were viable in both conditions (Figure 3.3.c-h) and no necrotic core was observed.

Visualization of chemo-gradient. We next set out to gauge the exposure of the spheroids and individual cells within the microdevice to a chemical gradient. To assess how this exposure is time dependent, Rhodamine B (1 µg/ml) was added to one side of the confined collagen hydrogel in the microdevice and allowed to diffuse across the hydrogel. Time-lapse confocal images show the gradient evolved along the full width of the central microchamber (Figure 3.3.a and b).

We next set out to evaluate the spheroid gradient sensing ability using FDA that was added to one side of the collagen hydrogel within the microdevice and allowed to diffuse across the hydrogel. In live cells, FDA enters through the cell membrane and once inside the cell, it is transformed by the action of esterases into the green-fluorescent compound Fluorescein [111]. Thus, cells within the spheroid became fluorescent once they are exposed to the FDA perfused through one of the lateral microchannels. As can be seen (Figure 3.4.c), cells on the surface of the spheroid did indeed show fluorescence, however, the intensity of this fluorescence was not uniform across the spheroid boundary at any stage during the 1 hour experiment (Figure 3.4.d). Instead, those cells on the spheroid closer to the diffusing chemical front show more fluorescence intensity, suggesting that they are exposed to more FDA. Over the length of the experiment, fluorescence intensity gradually builds up not only in the front of the spheroid, where exposure to the chemical continues, but also to the sides and the back of the spheroid (Figure 3.4.e). Interestingly, whilst there is significant infiltration of the chemical into the spheroid, FDA appears to reach the back of the spheroid before reaching the core. Fluorescence intensity measurement along spheroid perimeter showed a maximum centred on the region closest to the microchannel perfused with FDA, and decreasing as the distance increases (Figure 3.4.f). This pattern is wholly consistent with a chemical front moving across the microchamber and washing over the spheroid rather than penetrating through it. Since we have already shown the whole of the spheroid contains viable cells, we conclude that this is not due to a necrotic core, but an inability of FDA to penetrate through the spheroid at a rate comparable to the one it diffuses through the medium.

When FDA was flushed manually through the hydrogel, exposure of the spheroid to the chemical was uniform and fluorescence intensity along the spheroid perimeter showed homogeneous distribution (Figure 3.4.f, blue line).

Here a FDA/Rhodamine B gradient has been characterized. However in the FBS there is a complex mixture of different growth factors. These different growth factor have different molecular weights, which have a deep impact on the diffusion velocity. To illustrate this, diffusion profile of fluorescent 10kDa and 70kDa dextrans was recorded using confocal microscopy (Figure 3.5). The results show how the larger dextran takes longer time to diffuse through the hydrogel. Many of these FBS growth factors have a molecular weight within this 10 kDa-70 kDa range, therefore these results provide of a general time-scale of the diffusion profile and show the influence of the molecule size on gradient evolution.

Spheroids migrate against the chemotactic gradient inside the microfluidic device. We next turned our attention to the invasion of OSC-19 spheroids. It is already a well-established principle that cancer cells directionally invade towards serum enriched environment [98, 99]. To demonstrate that OSC-19 spheroids invade in response to serum, we first carried out a migration experiment outside the confines of the microdevice. OSC -19 Spheroids embedded in collagen were applied to wells of 96-well plate and cultured in complete medium. In this experiment, spheroids experience a uniform (non-gradient) concentration of FBS. We observed that the rate of spheroid invasion depended on the concentration of FBS. Whilst no invasion was observed in 0% FBS, and little invasion in 1% FBS, in 10% FBS there was significant, but non directional and quite random, migration (Figure 3.6).

In the microdevice, a FBS gradient can be achieved by injecting one of the microchannels with growth media containing 10% FBS (complete media) and the other microchannel with media containing 0% FBS (incomplete media), thus establishing a gradient of FBS across the microdevice. In a control experiment, both microchannels are charged with the 10% FBS containing growth media. For OSC-19 spheroids inside the device, when there is no gradient of serum across the microdevice, for example when both channels are charged with the complete growth media, we observed no directional invasion (Figure 3.7). When the OSC-19 spheroids were subjected to a FBS concentration gradient we observed a clear, collective invasion of cells towards that concentration gradient (Figure 3.8).

Whilst this invasion is clearly directional and towards the concentration gradient of the FBS, it is not uniform. Indeed, we consistently observed cell offshoots with significantly more invasive response. This will be entirely consistent with the proposal that in collective migration, leader cells open up the path of invasion and other cells follow them [112]. It is interesting to note that in view of our earlier observation which showed that chemoattractant wave engulfs the spheroid rather than go through it, we believe the invasion is mostly initiated from the outer layers of the spheroid.

Significantly, this invasion is both aggressive (*vide supra*) and coordinated, resulting in cells invading collectively.

Spheroids invasion versus isolated cell migration. Isolated OSC-19 cells where embedded in a collagen hydrogel within the microdevice, and response to 10% FBS gradient was evaluated. Isolated cells trajectories were tracked, showing no preferential migratory direction and very low net displacement (Figure 3.9.a and Figure 3.8.b, at least ten cells were analyzed). Cell viability was measured using FDA/PI once the experiment finished, revealing a majority of cells to be viable (Figure 3.9.c). Interestingly, analysis of time-lapse images revealed that spheroid cells velocity and directionality were much higher compared to the isolated cells (Figure 3.8.b). This observation is in excellent agreement with previous works showing how epithelial cells migrate more intensely when they are allowed to migrate by a collective movement [113, 114]. Given the relatively short time scale of the experiment and the relatively far distance the cell front moves during the experiment, it is unlikely that proliferation plays a major role in the invasion process. Nevertheless, in order to measure any contribution from proliferation to the invasion process, we checked for the expression of Ki-67, a well-established cellular marker of proliferation, in OSC-19 as well as U-87 MG spheroids, by immunofluorescence. For OSC-19 spheroids, the results showed that cells located beyond the leading edge of invading cells where negative for Ki-67 although as expected, population of cells at the invading edges where positive for Ki-67. Whilst the cells on the leading edge are expected to be more proliferative, due to more exposure to the serum, this result demonstrated that proliferation as well as migration contributes to the invasion process.

Operation of microdevice can be fine-tuned for other spheroids. We also investigated migration of U-87MG spheroids. Since these cells are non-endothelial, we expected the pattern of migration to be different. Again, to demonstrate that U87-MG cells migrate in response to serum, we first carried out a migration experiment outside the confines of the microdevice. U87-MG Spheroids embedded in collagen were applied to wells of 96-well plate and covered in complete growth medium to experience a uniform (non-gradient) concentration of FBS. As before, we observed that the rate of spheroid migration depended on the concentration of FBS, however in this case, expansion of the spheroid was significantly faster and even at 0% FBS, we did observe some expansion of the spheroid (Figure 3.10). To account for the greater responsiveness of U87-MG cells to FBS, a less steep concentration gradient of FBS was applied across the microchamber by injecting one of the microchannels with growth media containing 1% FBS and the other microchannel with incomplete media (containing 0% FBS). We found that the less steep concentration gradient helped in visualising migration pattern as there were fewer cells (Figure 3.11). When proliferation was measured, no Ki-67 positive cells were observed, demonstrating that U-87 invasion was due only to migration processes.

3.4 Conclusion

Chemotaxis is the principle mechanism by which cells migrate within multicellular organisms. Within that general description, chemotactic processes play different, and quite significant roles in many biological processes and in particular in many developmental and pathophysiological events. Therefore, in vitro models that enable the study of chemotaxis have become important tools in biology, particularly those models that provide a closer analogy with physiological systems. In this context, the microdevice we describe herein, and its application to the investigation of the migratory aptitude of multicellular spheroids is a particularly powerful tool.

It is already well established that multicellular spheroids provide a number of advantages over 2D cultures [115–117]. They are considered a more complete model that takes into account cell-cell interactions akin to what is observed in real tumours. Our investigations demonstrate further advantages of using microdevices in the study of multicellular spheroids. The control of the chemotactic gradient across the microchamber, coupled to the ability to observe and closely monitor the system over time, makes this a powerful technique for the study of the chemotactic processes. In recent years, collective invasion is arising as the dominant migration mode during epithelial tumour development [104] and the protocol outlined here enables that process to be observed and analyzed *in vitro*.

Furthermore, microfluidic devices such as the one designed and used here, can clearly have a much wider application. Work is ongoing in our groups to expand the scope of this technique, to study the migratory aptitude towards chemotactic cytokines (chemokines) which are known to play a significant role in cancer cell migration and metastasis; and to study co-cultured multicellular spheroids containing mixed population of cells which better represent the tumour microenvironment.

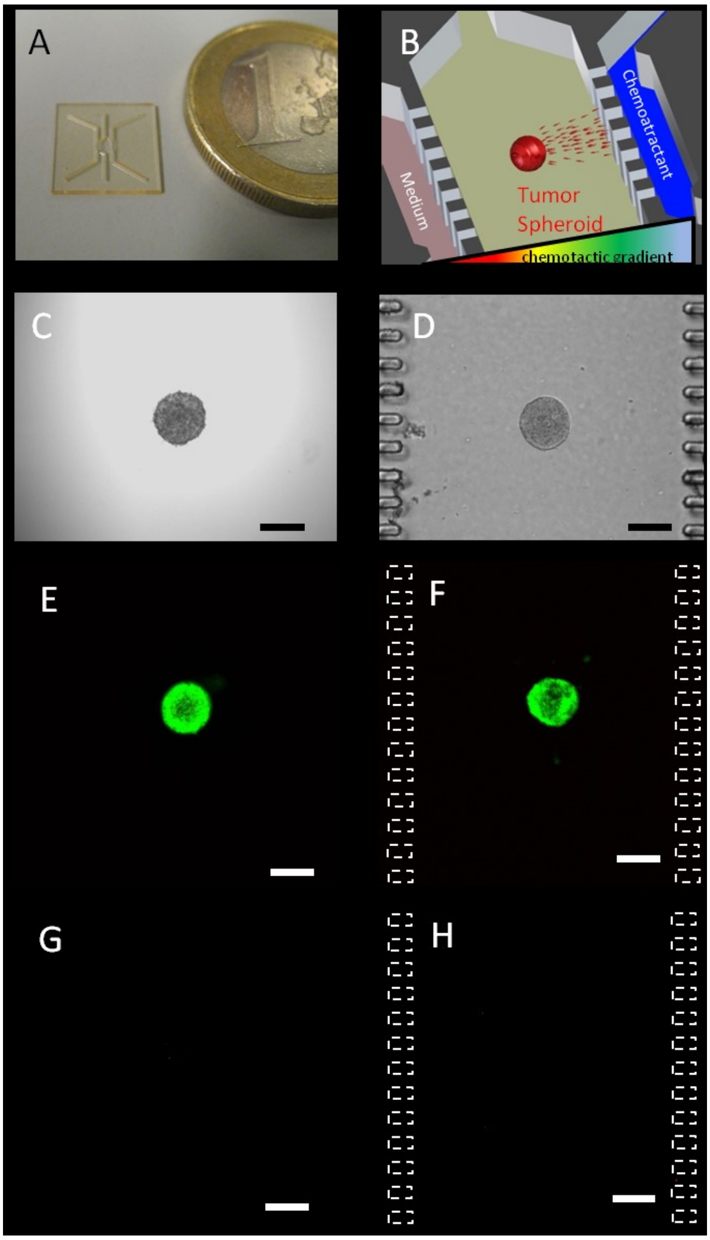

Figure 3.3. Experimental set-up: a) SU-8 fabricated microdevice, a) experimental scheme, c) OSC-19 spheroid of 2000 cells in the hanging drop, d) Same spheroid after embedding in 1.5 mg/ml collagen hydrogel within the microdevice. Treatment of the spheroids with FDA/PI after 48 hours in a hydrogel in a well of a micro titre plate or within the microdevice shows the spheroid is intensely green (e and f respectively) whereas less than five red cells where observed (g and h respectively)Z projection of the whole spheroid is shown. Scale bar is 200 µm.

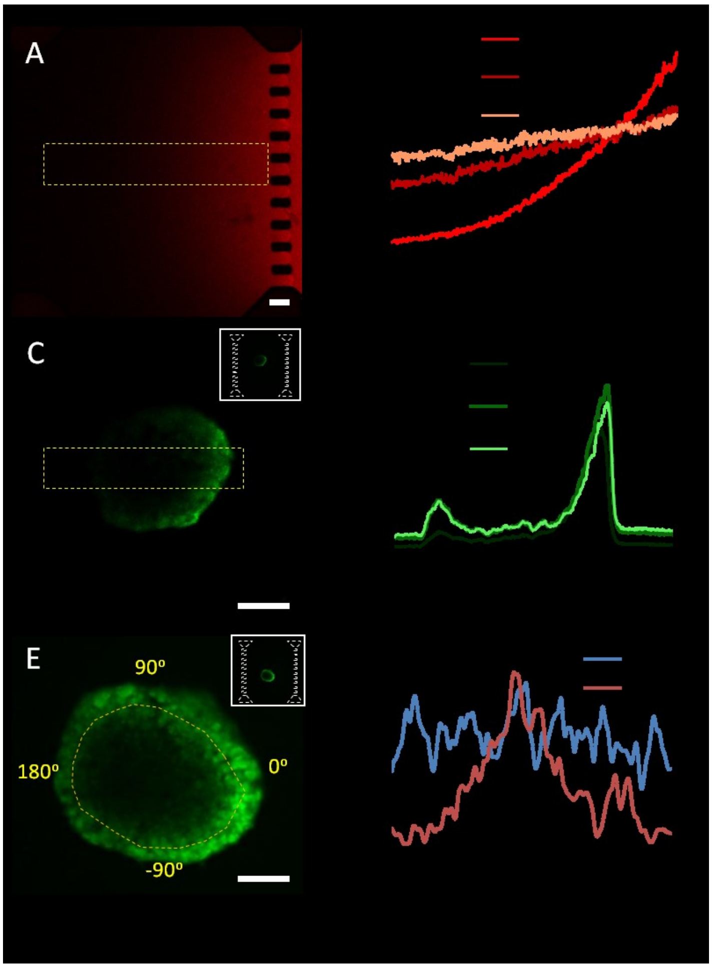

Figure 3.4. Chemical gradient across the microchamber: a) a complete image of the microchamber 5 minutes after red fluorescent Rhodamine B was perfused through the right lateral microchannel, b) evolution of fluorescence intensity of Rhodamine B along the whole microchamber width (as highlighted in yellow in a) over time, c) an image of an OSC-19 spheroid after 5 minutes of FDA perfusion through the right lateral microchannel, d) Fluorescence intensity along the section of the spheroid (as highlighted in yellow in b) after 5 minutes of FDA perfusion, e) fluorescence intensity within the spheroid after 1 hour of FDA perfusion, f) fluorescence intensity along the spheroid perimeter after 1 hour of FDA perfusion through only one lateral microchannel (gradient condition-blue line) or through the hydrogel (control condition-red line). Images corresponding with the spheroid middle focal plane are shown. Scale bar is 100 µm.

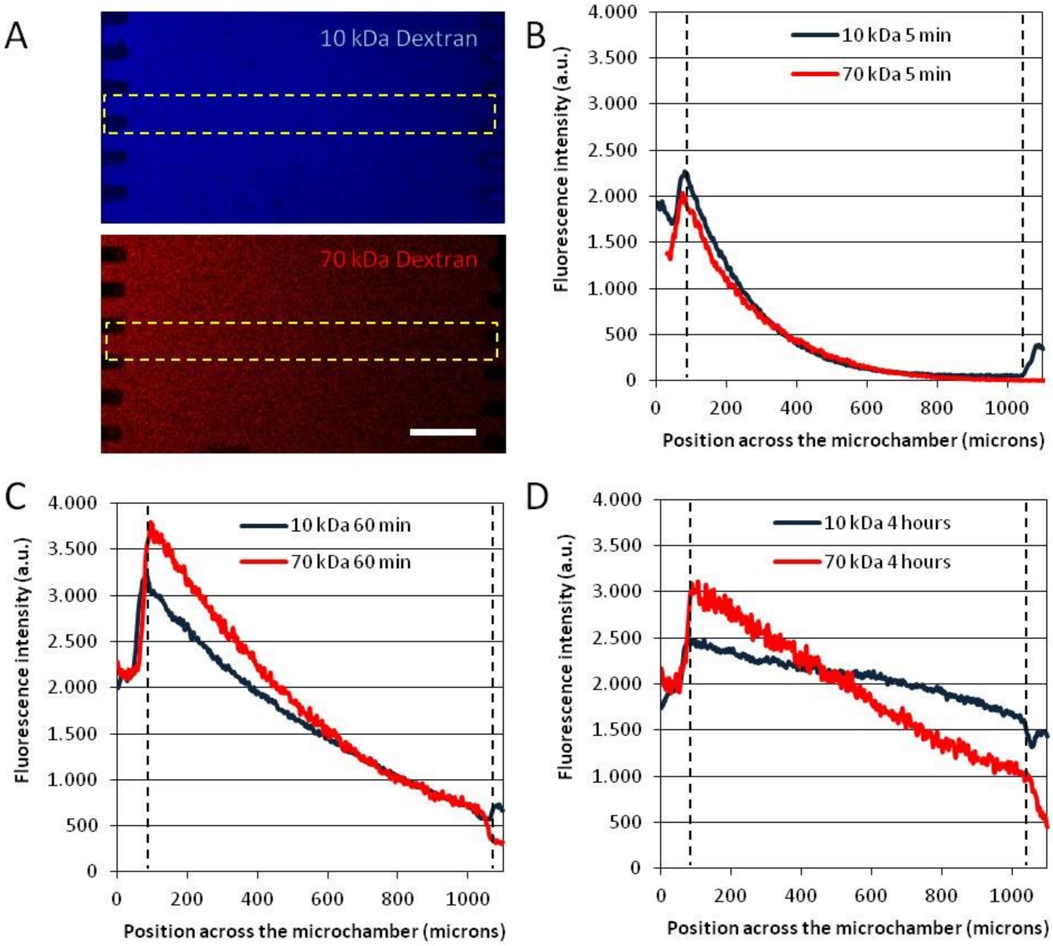

Figure 3.5. Influence of molecule size on diffusion profile: a) cascade blue-10 kDa and TRITC-70 kDa dextran at 10 µM were injected in the left microchannel and confocal images are shown after 4 hours. Fluorescent 10 kDa and 40 kDa diffusion profile is compared at 5 min (b), 60 min (c) and 4 hours (d) post-injection.

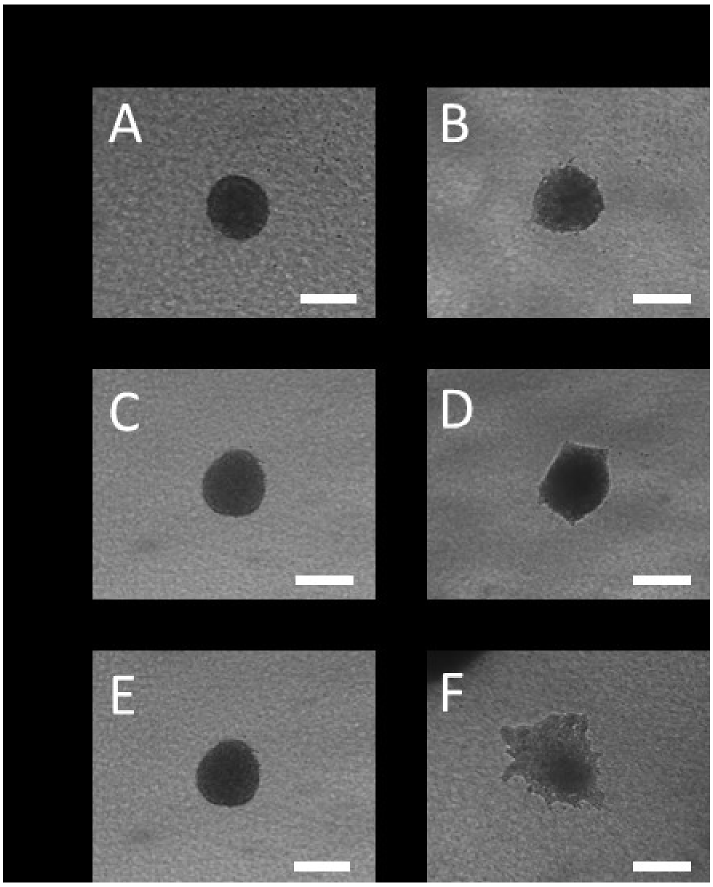

Figure 3.6. FBS influence on OSC-19 spheroid invasion: OSC-19 spheroids were embedded in collagen hydrogel in a six well plate and growth media supplemented with 0%FBS (a and b), 1% FBS (c and d) and 10% FBS (e and f), was applied over them. Photos were taken at embedding time (0 H) and after 20 H. Scale bar is 200 µm.

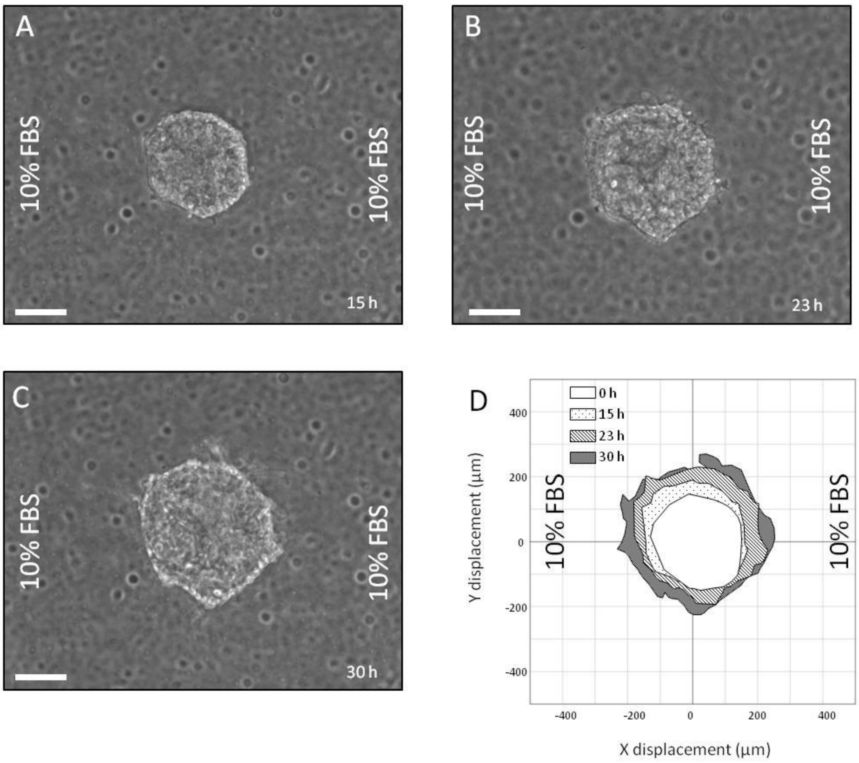

Figure 3.7. Chemotactic behaviour of OSC-19 spheroids under no gradient: OSC-19 spheroids were embedded in collagen hydrogel within the central microchamber. Media supplemented with 10%FBS was perfused through both lateral microchannels. Spheroid invasion is shown after (a) 15 hours, (b) 23 hours, (c) and 30 hours, d) Area occupied by the spheroid at different times is represented in the graph. Scale bar is 100 µm.

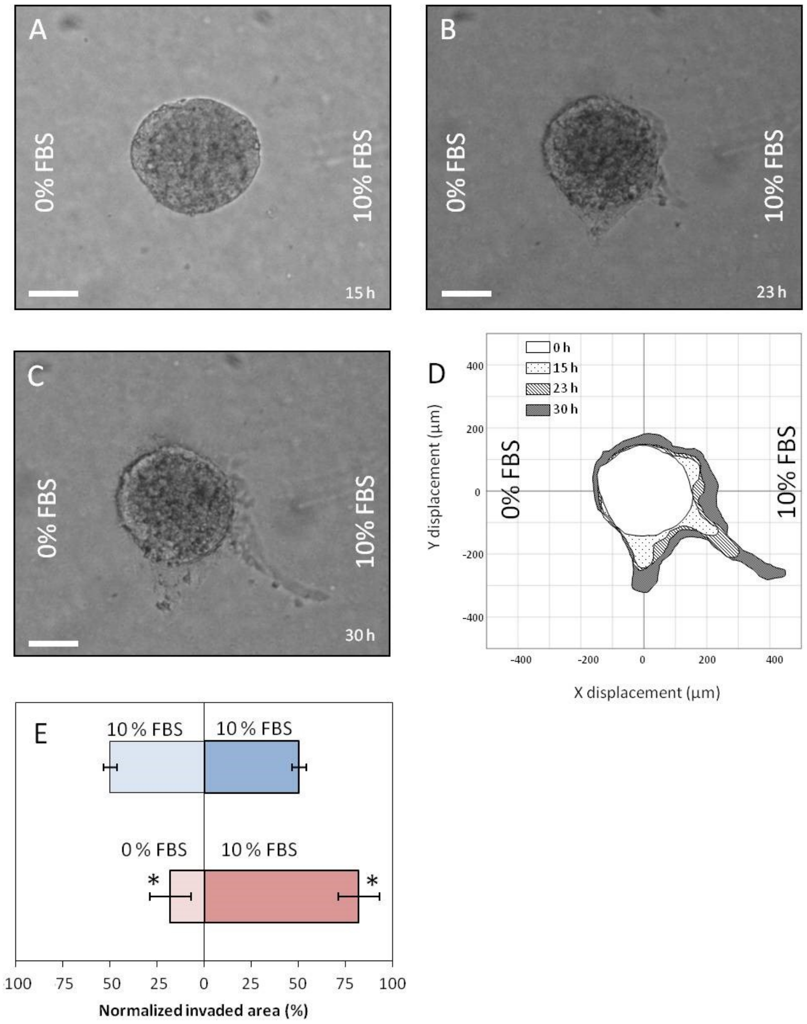

Figure 3.8. Chemotactic behaviour of OSC-19 spheroids under a chemotactic gradient: OSC-19 spheroids were embedded in collagen hydrogel within the central microchamber. Media supplemented with 10%FBS was perfused through right hand lateral microchannel, whereas incomplete media was used in the other. Spheroid invasion is shown after (a) 15 hours, (b) 23 hours, (c) and 30 hours, d) area occupied by the spheroid at different times is represented in the graph. (E) Comparison between invaded area under gradient and non-gradient conditions, asterisk denotes difference between both halves is statistically significant (p-value < 0.05). Scale bar is 100 µm.

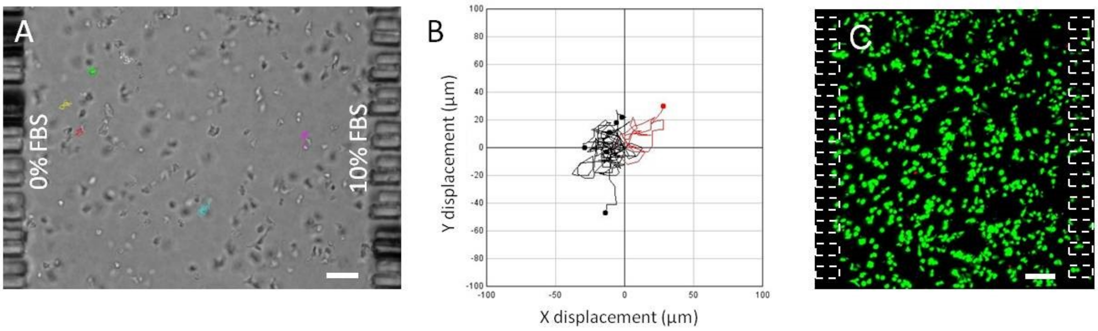

Figure 3.9. Chemotactic behaviour of OSC-19 individual cells: Individual OSC-19 cells were embedded in collagen hydrogel within the central microchamber. Media supplemented with 10%FBS was perfused through one lateral microchannel, whereas basal media was used in the other. a) tracks of migrating cells, b) individual cell trajectories are plotted, showing those with a net displacement to the right in red, and those displaced to the left in black, c) Isolated OSC-19 cell viability after 30 hours under gradient conditions, viable cells are shown in green. Scale bar is 100 µm.

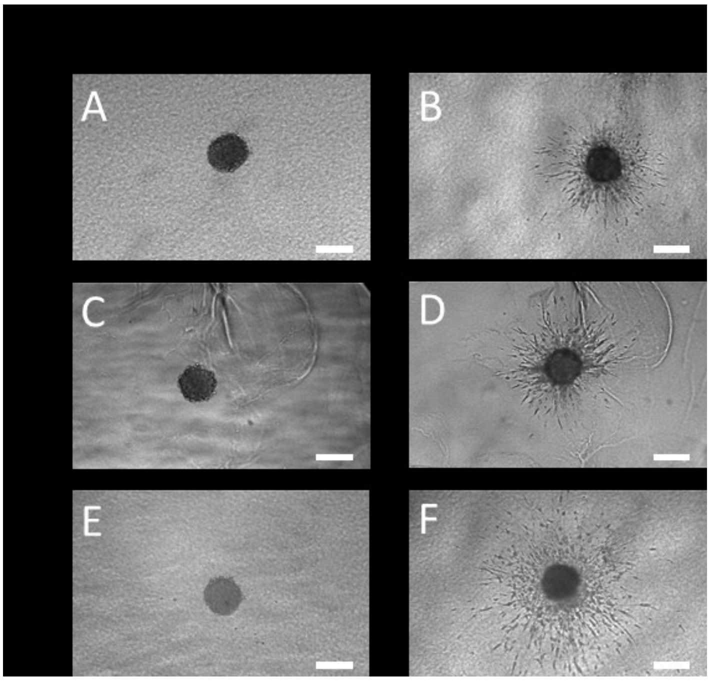

Figure 3.10. FBS influence on U-87-MG spheroid invasion: U87-MG spheroids were embedded in collagen hydrogel in a six well plate and growth media supplemented with 0%FBS (a and b), 1% FBS (c and d) and 10% FBS (e and f), was applied over them. Photos were taken at embedding time (0 H) and after 20 H. Scale bar is 200 µm.

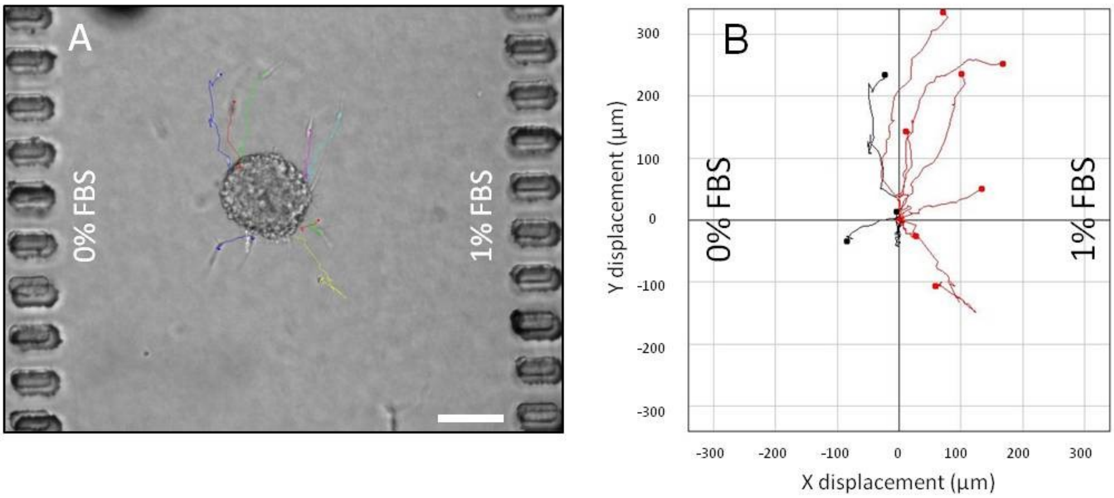

Figure 3.11. Chemotactic behaviour of U-87MG spheroids under a chemotactic gradient: Spheroid was embedded in collagen hydrogel within the central microchamber. Media supplemented with 1%FBS was perfused through one lateral microchannel whereas basal media was used in the other. a) brightfield image with overlaid tracks of migrating cells after 12 hours, b) Individual cell trajectories are plotted, showing those with a net displacement to the right in red, and those displaced to the left in black. Scale bar is 100 µm.

Chapter 4

Development of a 3D cell culture system based on microfluidics for nuclear magnetic resonance and optical monitoring

A new microfluidic cell culture device compatible with real-time nuclear magnetic resonance (NMR) is presented in this chapter. The intended application is the long-term monitoring of 3D cell cultures by several techniques. The system has been designed to fit inside commercially available NMR equipment to obtain maximum readout resolution when working with small samples. Moreover, the microfluidic device integrates a fibre-optic-based sensor to monitor parameters such as oxygen, pH or temperature during NMR monitoring, and it also allows the use of optical microscopy techniques such as confocal fluorescence microscopy. This chapter reports the initial trials culturing neurospheres inside the microchamber of this device and the preliminary images and spatially localised spectra obtained by NMR. The images show the presence of a necrotic area in the interior of the neurospheres, as is frequently observed in histological preparations; this phenomenon appears whenever the distance between the cells and fresh nutrients impairs the diffusion of oxygen. Moreover, the spectra acquired in a volume of 8 nL inside the neurosphere show an accumulation of lactate and lipids, which is indicative of anoxic conditions. Additionally, a basis for general thermostatisation and monitoring and a graphical control software have been developed and are also described.

4.1 Introduction

Nuclear magnetic resonance is a technique that is widely employed in clinical practice for diagnosing and monitoring diseases in patients, particularly when soft tissues are involved.

There are several modalities that exploit the different characteristics of this technique. For example, magnetic resonance imaging (MRI) produces high quality images of the inside of the human body that enable the precise localisation of alterations, whereas magnetic resonance spectroscopy (MRS) provides spectra that are of considerable importance for determining the diagnosis, evaluating the prognosis and conducting the follow up of diseases that are difficult to manage, such as brain tumours [118].

The use of new therapeutic and contrast agents in humans is very restricted, and testing in experimental animals will always be limited.

A detailed microscopic analysis of the response and NMR characteristics of cellular systems in vitro can provide very relevant information for the interpretation of clinical MRI and MRS monitoring observations. Moreover, testing and fine-tuning of the quantification of some parameters are possible at higher resolutions. These measurements can afterwards serve as well-founded references [119].

Furthermore, a multimodal image comparison that includes optical microscopy will provide complementary information, which is often indispensable in clinical practice.

One common approach is the direct study of biopsies taken from the tissue of interest, which can be very informative but frequently has severe limitations [120, 121]. *In vitro* cell culture is a key methodology in biomedical studies, and there is a growing demand for detailed *in vitro* analyses [122]. Nevertheless, the lack of knowledge about the functioning of living tissues and about the factors that induce and maintain the differentiation observed in several types of tissues, in particular the heterogeneous phenotypes that tumoural cells show *in vivo*, limit their replication in research studies.

On the other hand, biotechnological research has generated great interest in the development of new drug delivery systems to improve both the pharmacological and therapeutic properties of drugs. Drug delivery systems based on nanomaterials offer easier penetration in certain regions of the body due to their small size and simple surface modification [123–125].

For example, gold nanoparticles conjugated with antibodies have proved to be useful for both selective imaging and the photothermal ablation of cancer cells

[126–128]. Their importance as contrast agents for NMR or as therapeutic agents relies on an understanding of their distribution, half-life and excretion from or storage inside the target cells and the subsequent development of these cells and their neighbours [129, 130]. Moreover, performing such a complete analysis requires long-term monitoring, including multimodal imaging and NMR, and the observation of an identical system (not a similar one reproduced in another plate) and each individual cell within that system.

To mimic the same conditions experienced by cells in vivo and to have maximum control of that environment, an active study in the scientific community is being conducted to develop devices that combine microfluidic and microfabrication techniques to construct structures and matrices that simulate the cellular environment inside living tissues [131]. Thus, the nutrients and signalling factors as well as the gas exchange and mechanical forces that the cells experience would be extensively controlled [132–135].

The increasing sophistication of the lithography techniques and computer-directed construction used in the fabrication of chips and electronic devices allows the design of complex systems in which several types of sensors can be integrated to implement “micro-scale laboratories” (Lab-on-a-Chip). Diverse materials are employed in the construction of such devices, but resins and polymers (PDMS, COP, PMMA, SU-8, etc.) are predominately used. A wide variety of designs for specific applications are being developed, although most of these designs are still at a preliminary stage of development [136].

NMR microscopy has developed in parallel with the standard macroscopic image techniques used in clinical and animal applications [137–139]. However, further developments and applications will require increased resolution and adequate methods for handling small living samples. Such technological challenges can only be addressed by a close and coordinated collaboration with specialised developers.

Several home-made devices for containing cells during NMR analysis have been prepared for specific studies. Some of these are designed for bulk spectroscopy [140] and others are designed for microimaging [141] or a combination of microimaging and spectroscopy [142, 143], and some are also designed to include fluidics [140]. However, none of these devices are easy to use with standard commercially available equipment, and in general, they are of limited scope.

In this chapter, a new complete system for the long-term monitoring of organotypic cell cultures by NMR and optical techniques is presented. The aim was to develop a complete platform that permits a multimodal analysis of a 3D cell culture while maintaining conditions that mimic natural tissue, including the flow of nutrients and the cellular microenvironment. The results report the development of a microfluidic chip for cells based on SU-8, as well as its packaging for easy handling, replacement and coupling to NMR electronics. We present a preliminary NMR analysis of neurosphere cultures to show the feasibility of the device.

4.2 New microfluidic device design

While there are already many different approaches to obtaining stable cell cultures on microfluidic devices, coupling such devices to an NMR system for monitoring remains challenging in practice. As a result, these devices suffer from limitations in sensitivity and resolution. The strategy selected in this design aims to increase the signal-to-noise ratio using a microcoil in close proximity to the sample and to reach maximum resolution using strong magnetic gradients. As the microfluidic chip is intended to be disposable, the microcoil is fabricated with a different substrate and is then placed directly on top of the cell microchamber by using a dedicated packaging (see Figure 4.1). Moreover, to achieve a minimal distance between the microcoil and the biological sample under study, a thin layer is used for the fabrication of the microchamber cover (75 m). The total thickness of the chip is 550 m. This allows for insertion into the microgradient device while maintaining optimal proximity to the magnetic fields (Figure 4.1d).

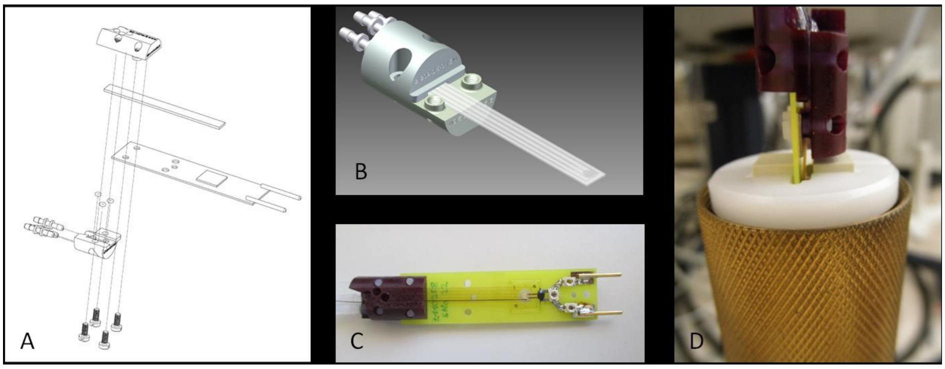

Figure 4.1. (a) View of the device parts assembly. (b) Cell culture chip packaged with microfluidic connections. (c) The PCB is screwed to the packaging to place the microcoil in close contact with the cell culture microchamber. (d) The system is mounted inside the NMR sensor.

The complete assembly of the microfluidic device was designed to include the following items:

1. A PCB with an integrated microcoil fabricated by Bruker Biospin and now commercially available with several microcoil diameters.
2. A microfluidic chip for cell culture (see detail of the design in Figure 4.2) that is designed as follows:

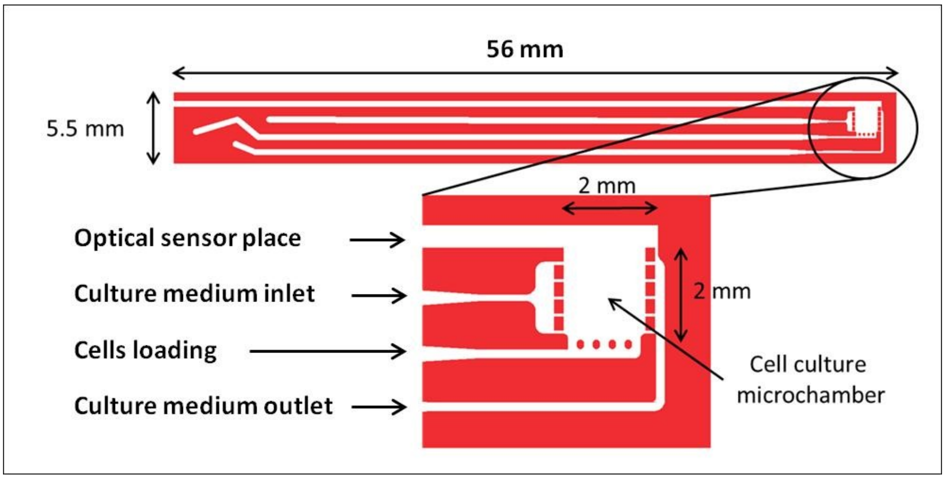

Figure 4.2. Top view of the microfluidic chip design showing the most relevant features and dimensions.

Microfluidic devices were fabricated using SU-8 photolithography combined with an SU-8 to SU-8 bonding process [107, 144]. SU-8 is an NMR-compatible material that offers high fabrication resolution [145], transparency for optical inspection [146], enough mechanical stability for easy handling and coupling with the microcoil [147, 148], and biocompatibility for use as a structural material for cell culture applications [149–153]. The final design of the device is presented in Figure 4.2 and consists of a 56 mm long chip that includes a 2 by 2 mm microchamber. The microchamber can be reached through four dedicated microchannels, which allow the required microfluidic control and facilitate access to the optical sensors. Each one of these four microchannels has a dedicated task as follows:

Optical sensor placement: This microchannel holds the optical fibres used as sensors. The fibre is introduced through the microchannel until the tip finds the main culture chamber. Readout from the fibre is then used for temperature and pH monitoring.

Nutrient inlet: This microchannel is used for the perfusion of nutrients to the microchamber. A constant flow is applied to refresh the oxygen and nutrient concentration during the cell culture experiment. Low-flow rates

(< 1 L/min) were applied to avoid a dragging effect on cells under culture, which could result in voiding the microchamber.

Cell loading: Cells are carried through this microchannel to fill the microchamber. To allow the use of cell aggregates (like neurospheres) and to avoid clogging, the channel width is at least 200 µm or wider.

Nutrient outlet: Nutrients and waste residuals exit the chamber using this microchannel. As shown in Figure 4.2, pillars have narrow distances between them (75 m) to prevent cell aggregates from being dragged out of the microchamber.

3. A packaging body that supports the fluidic connections as well as the whole assembly by dedicated screws and joints (see Figure 4.1) that is designed as follows: The package is divided into two parts: a micro-device holder and an upper cover. The micro-device holder lodges the inlet-sealing o-rings and connects them to three fluidic tube connectors by means of internal channels. It also has mechanical clamps to fix the package to the NMR sensor. As long as the cover is screwed down over the chip holder, the micro-device is sealed and coupled to the tubes and is mechanically attached to the NMR sensor.

4.3 Materials and methods

4.3.1 Fabrication

The fabrication of the microfluidic device starts with the temporary bonding of a Kapton™ film on top of a 4" Pyrex™ wafer. Pyrex™ is used because it has low adhesion to SU-8, enabling an easy final release of the device once the fabrication has concluded. Then, an 80 m thick SU-8 layer is spun and soft-baked (SB) by heating the wafer in two steps; first up to 65 ºC for 10 minutes and then up to 95 ºC for 30 minutes. Once the SB treatment finishes, an exposure of 140 mJ/cm^2 is performed using a mask, which will define the bottom layer of the microfluidic channel. Next, a post-baked (PB) treatment is applied by heating the wafer up to 65 ºC for 5 minutes followed by 95 ºC for 15 minutes. Then, a 160 m thick SU-8 layer is processed on top by repeating the process described above twice, using the same SB, exposure and PB steps. The exposure step is performed using the same parameters while using a new mask, and in this case, the mask defines the microchannels and chambers. Then, a 20 m thick layer is processed for use as a bonding layer. While the SB parameters are kept the same, the PB parameters are changed by reducing the heating step at 95 ºC down to 7 minutes. Then, using another 4” Pyrex wafer with a Kapton film laminated on top, a new 80 m thick layer of SU-8 is processed as previously described to define the cover of the microchannels. This layer includes holes for use as fluidic inlets and outlets. Then, two 80 m and one final 20 m thick SU-8 layers are processed on top using the same mask used in the first wafer to define the microchannels but mirrored. Finally, both wafers are aligned and bonded by applying a pressure of 3 bar at a temperature of 100 ºC. Finally, the devices are manually released.

To avoid interferences in the measurement process, no conducting or magnetic materials are used for any part of the package. The micro-device holder and the cover are made of an epoxy resin and are fabricated by stereolithography. This technology allows each part to be built in a very compact and accurate way, including screws, internal channels of any shape, alignment features, etc. The sealing o-rings are made of a silicone elastomer, the fluidic connectors are made of PEEK, and the screws are made of nylon.

4.3.2 Assembly

Optical fibre-based sensors of pH (PRESENS™, pH-1Micro) and temperature (LumaSense™, Fluoroptic Temperature Probe) are introduced into the microchamber and sealed (Figure 4.3c). The whole device is assembled on the packaging holding the microfluidics and fastened by dedicated plastic screws. Thus, the device can be inserted together with the PCB containing the coil inside the magnetic gradient system for NMR analysis, or it can be mounted on a base for optical monitoring during the culture.

A supporting base with an integrated design made of methacrylate that allows for the replacement of parts has been developed to prepare and monitor the system when it is outside the NMR equipment. The support incorporates a Peltier plate for thermostatisation and several parts to hold and protect the chip and to encapsulate the fluidics and fibre optics. A microcontroller directs the thermostatisation and mechanical operations. We have incorporated a camera for time-lapse recording of the microchamber contents.

Finally, a mini-cabin has been constructed to protect and isolate the monitoring system from physical damage, dust, and thermal fluctuations. The assembly parts are made of methacrylate and aluminium and permit access from all sides.

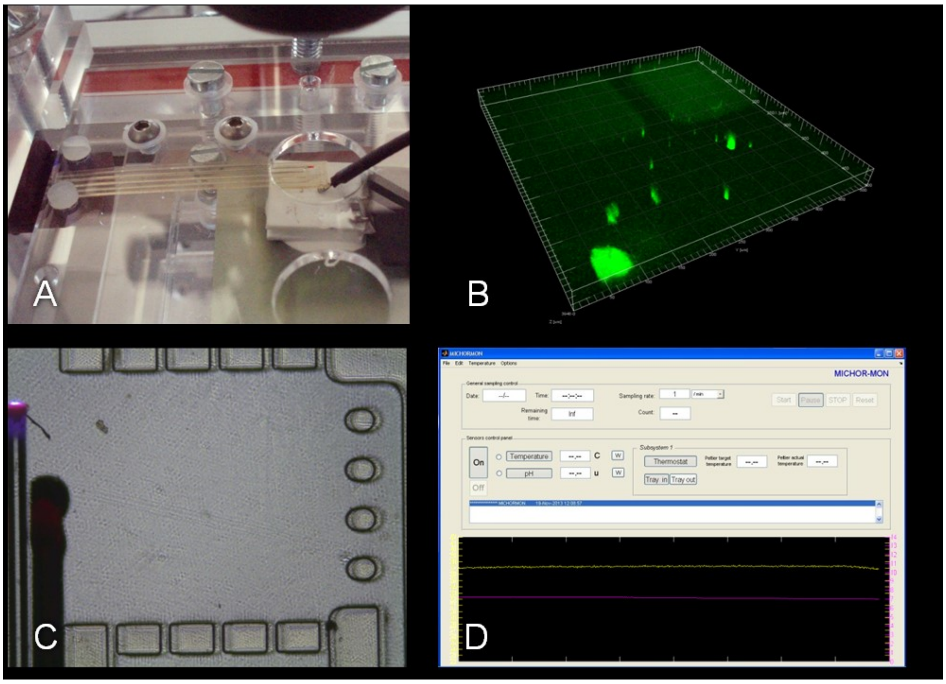

Figure 4.3. Monitoring and control. (a) View of the device mounted on the monitoring base. (b) Confocal 3D image in which the background fluorescence emitted by the SU-8 can be observed; the shape of some pillars are visible at the top, while inside the main chamber, only some silica-based particles containing fluorescence are clearly visible with little background intensity. (c) View of the main culture microchamber where the tips of the fibre optic sensors are visible on the left of the image. (d) Window presenting the GUI of the control and visualisation software MICHORMON.

A wide frontal sliding shutter allows the supporting base to be placed inside the cabin and manipulated from within the cabin. Two lateral and two rear windows also provided with sliding shutters allow the insertion of conductions and cables for external connections. The cabin can be mounted over a basic damping platform or optical board of metric spacing (more information available upon request).

The background fluorescence and resolution obtainable by multiphoton fluorescence microscopy was tested, proving the feasibility of the system (plastics often emit some fluorescence, but in this case, the thin cover used emits a low amount of background fluorescence around the culture chamber, see Figure 4.3b for a bi-photon confocal microscopy assay on an Olympus™ FV1000MPE microscope). Home-made software was developed in Mathlab to control the whole system (temperature, sensor activation, data logging, etc.; see Figure 4.3d).

4.3.3 Neurosphere culture

Neurospheres were grown using a bank of stored precursor cells obtained from the subventricular zone of rat brains prepared in previous experiments [154]. The cells were dispersed mechanically and cultured for seven days in Petri dishes with DMEM:F12 medium containing 10% BFS at 37 ºC with an air atmosphere containing 5% CO2 until neurospheres of a mean diameter of approximately 300 m were formed. The medium was supplemented with an N2 hormone mix and EGF and bFGF as mitogens [155]. The neurospheres were introduced into the microchamber by injection through the dedicated loading channel of the microfluidic device. The system was maintained at 37 ºC, and the basal DMEM:F12 medium with 10% FBS was provided at a low-flow rate of 10 nL/min if not otherwise specified.

4.3.4 NMR

NMR microscopy and spectroscopy was carried out in a Bruker™ spectrometer at 14 T with 60 A xyz gradient amplifiers (GREAT 60) using a Micro5 probe and surface microcoils (500 m internal diameter). Spatial gradients were generated with a new high-gradient system adapted to such microcoils (3000 G/cm).

Gradient echo-based image pulse sequences were tested using a 7 to 15 ms echo time, a 2 mm field of view, 128 to 512 scans and a 1 to 4 h total acquisition time. The experiments generated a matrix of data points of 256 x 256 and 128 x 128.

Single-voxel localised spectra were acquired using a PRESS sequence with water suppression on a volume of 8 nL (0.2 x 0.2 x 0.2). The acquisition time was 1 h 42' (4098 scans).

Tests of the flow control, of the microimage analysis of the injection system and of the fluid dynamics were performed by Gradient Echo and MDEF pulse sequences using flows of 0, 0.2, 1, 10, 100, and 500 L/min. Data were acquired as a matrix of 64 x 64 using 4 scans.

4.4 Results and discussion

4.4.1 Microfluidic device

The resulting SU-8-based microfluidic device is shown in Figures 4.1 and 4.3a. As can be observed, no curvature is obtained despite the unusual length of the chip and the high internal stress associated with SU-8 fabrication processes. As a result, a good contact between the cell culture microchamber and the microcoil can be achieved, resulting in a higher NMR analysis resolution. The planarity of the chip was obtained thanks to the fabrication process strategy, which was based on the bonding of two similarly structured SU-8 films. Being equal in thickness and exactly mirrored in design when finally bonded, the SU-8 chip deflection is negligible. This is because internal stresses from both SU-8 layers work in opposite directions, resulting in a planar device. Moreover, the fabrication process facilitates the safe development of the required micropillars. If such structures had been fabricated on the same SU-8 layer, it would have been difficult to ensure complete SU-8 development without a high risk of pillar tilting or even complete detachment.

This microchamber was designed to fit the new microgradient devices used in Bruker equipment to obtain maximum resolution when working with small samples. In particular, the necessary proximity to the surface of the new planar microcoil required a very thin (approx. 75 m) cover surface over the growth chamber area. This design allows the exploitation of the capabilities of the microcoils and microgradients, while the cell culture is maintained independent of the electronic system.

A long free surface of the chip outside the encapsulate is required for insertion into the NMR equipment and for reaching the microcoil position, but this makes the chip very susceptible to damage and bending. This problem required construction of a dedicated holding system to enable the chip to function outside of NMR devices. The holding system is composed of a cabin and a basement that can support the attachment of the thermal control and the optical monitoring devices.

The size of the pre-chamber was adjusted to guarantee a uniform flow entering the main microchamber. Despite the reduced thickness of the chip, it supports fast flows of approximately 1 mL/min, which can be useful for cleaning and bubble elimination during the preparation of the chamber prior to receiving cells. The size of the microchamber (approximately four square millimetres) requires small quantities of cells and medium, thus an organotypic piece of tissue up to a maximum 400 m thickness can be readily obtained. A dedicated microchannel allows the cells to be placed directly inside the main culture chamber, while the medium flow continues through the pre-chamber, thus circumventing any clogging created during the injection of cells. This offers a major degree of manoeuvrability.

4.4.2 Cell Culture

Neurospheres of approximately 300 m diameter were injected into the microchamber and were successfully grown for 48 h until coalescence. Then, we eliminated the mitogens from the medium (EGF and bFGF growth factors), allowing cells to differentiate for 72 h. A variety of morphologies characteristic of neuronal and radial glia were obtained, including the formation of a 3D structure (see Figure 4.4a, b). A low flow of approximately 10 nL/min was used to maintain a local microenvironment around the cells that allowed an adequate renovation of the medium.

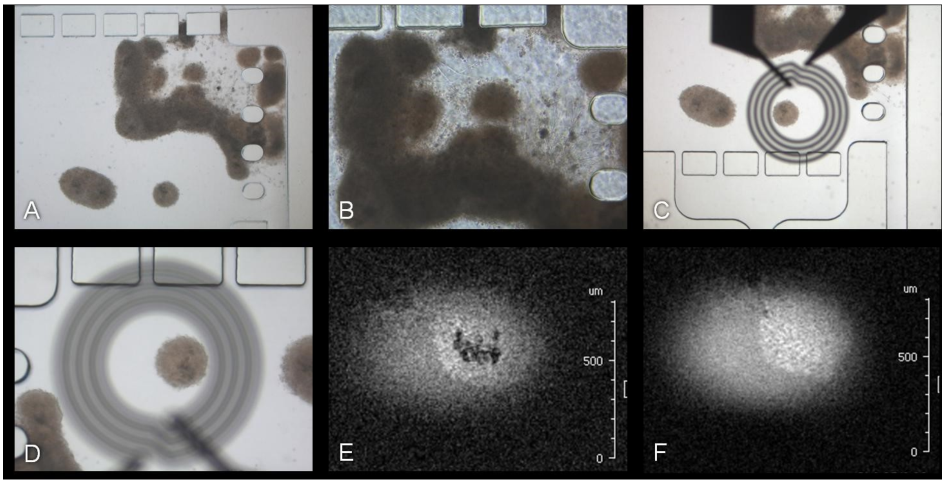

Figure 4.4. Images of the neurospheres growing inside the microfluidic device. (a) Some neurospheres coalesced, growing in a corner at the entrance of the cell conduction channel. (b) The shape of the differentiated cells is indicated by a 3D outgrowth from the aggregated mass. (c) and (d) Optical images with the microcoil superimposed onto the microchamber and showing a neurosphere centred inside; (d) is inverted with respect to (c) to compare with the next images. (e) and (f) NMR microimages obtained at two different sections 180 μm apart; only the area covered by the microcoil appears "illuminated"; in (e), an internal and presumably necrotic area can be observed in this central section, whereas it is not visible in the most superficial section in (f). The in-plane resolution is 8 × 8 μm, whereas the slice thickness is 50 μm.

4.4.3 NMR analysis

NMR microimaging and localised spectroscopy techniques were adapted from our previous work studying brain tumour biopsies to optimise resolution on a standard base [156].

We initially performed fluidic assays with NMR standard tubes and capillary tubes to test the performance of the main experiments at different flow rates of medium inside the NMR instrument, and the whole performance of the injectors was tested. Then, we conducted flow tests with the microfluidic device. The results showed no differences between the images obtained with stopped flow conditions and those obtained with a 0.2 L/min flow. We observed a clear disruption when the flow was increased to over 100 L/min.

When neurospheres were cultured inside the microchamber, we were able to obtain a preliminary set of images and spatially localised spectra. The images (see Figure 4.4) show a darkened area that is most likely due to the presence of a necrotic area in the interior of the neurospheres, which can frequently be observed in ordinary histological preparations when the distance to the surface impairs the diffusion of oxygen.

The spectra acquired in a volume of 8 nL inside the neurosphere show an accumulation of lactate that is indicative of anoxic conditions (Figure 4.5) and is something commonly found in the necrotic areas of glial tumours [120]. The signal-to-noise ratio for the lactate signal was 19 and was only 5 for the glucose signals. We currently are working to improve both the signal-to-noise ratio and resolution by adapting the standard pulse sequences to the new hardware.

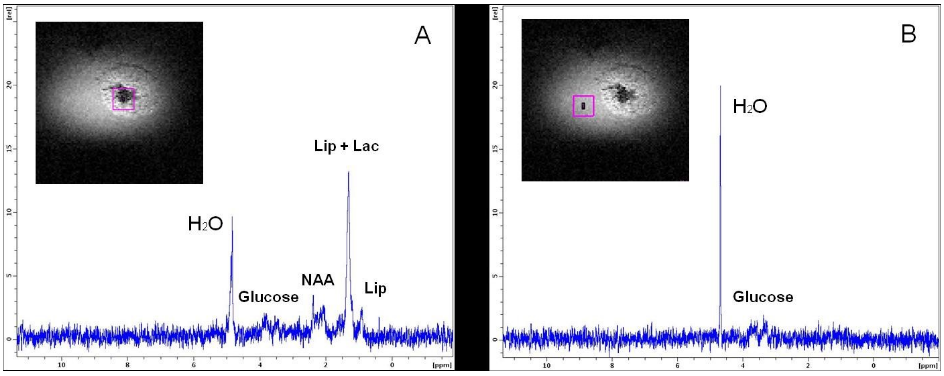

Figure 4.5. NMR water-suppressed 1H spectra obtained inside (a) and outside (b) the neurosphere in a localised voxel of 8 nl. Some tentative designations are labelled in the figure. A considerable amount of lactate and lipids seem to be present in the necrotic interior.

4.4.4 Control

Two optical fibre sensors allowed the temperature and pH to be monitored two times per minute inside the microchamber. Both sensors are based on the sensitivity of a specific fluorophore (quantifying variations produced in the emission spectra) to the changes in temperature and pH in the microenvironment.

Thermostatisation was realised using a Peltier plate and a microcontroller that stabilised the temperature to approximately 37 ºC. Measurements at 12 h reported a standard deviation of approximately 0.1 for the temperature and pH (mean value of 7.2 for pH).

We developed a basic software platform for the concerted monitoring of the different fibre optic sensors, optical imaging and thermostatisation. A graphical user interface allows selection of the data login, paucity of the monitoring, configuration of the sensors, targeting of the temperature control and visualisation.

Though more complex designs for the culture microchamber could be helpful for specific applications, for example to direct or control cellular growth, other alternatives are also possible. We have successfully inserted a specific scaffold during fabrication, which opens the possibility of developing and incorporating independently made pieces of scaffold with the required features to allow a broader array of applications.

4.5 Conclusions

Over the last few years, we developed a prototype micro-reactor (lab-on-chip) for the long-term monitoring of tissue samples and organotypic cellular systems with special characteristics that allows the use of NMR microscopy and/or optical techniques for molecular imaging. The system maintained 3D cellular cultures within an environment similar to the conditions of natural tissue, including the flow of nutrients and the cellular microenvironment. Moreover, specific tools were developed to control the system (integration of temperature sensor, pH sensor, Peltier plate, etc.).

Neurospheres were successfully seeded, grown and differentiated inside the microfluidic chamber to generate a 3D cell culture network. The system allowed the monitoring of temperature and pH inside the microchamber. The images obtained using the system confirmed the presence of necrotic areas in the sections with less access to fresh nutrients, as observed in the histological analysis of real samples. Finally, spectra acquired by NMR in a volume of 8 nL inside the neurosphere showed an accumulation of lactate indicative of anoxic conditions, confirming the viability of NMR analysis within the microchamber.

The whole system constitutes a single platform that will allow several biomedical assays of therapeutic agents to be performed while also being monitored by NMR and optical techniques. The system will require small quantities of drugs or nanodevices, which will be able to reach the cells through a flow system that more closely approximates living conditions than plated cell cultures.

NMR is a non-invasive technique that provides structural and physiological information, which is a characteristic that we believe to be essential for monitoring a live cell assay with minimal disturbance. This micro-device could be of great help in the quest for new powerful clinically relevant image biomarkers directed to specific macromolecular targets while using minimal amounts of product.

Future developments will require a more advanced design for the cell culture platform to maintain real 3D tissue development, including special features from the natural microenvironment as well as the control of these features. To this end, we have initiated attempts to combine 3D scaffold technologies with the microsystem device prototype for organotypic cell culture. Three-dimensional scaffolds with different features at the macro, micro, and nano scales will be fabricated with rapid prototyping techniques alone or in combination with electrospinning [157]. These platforms will allow the precise control of the pore structure and architecture of the fabricated scaffolds, resulting in 3D matrices with controlled structural, physicochemical, and mechanical properties that can be elaborated independently and then inserted into the culture chamber.

Chapter 5

SU-8 micro Coriolis mass flow sensor

This chapter presents the modelling, design, fabrication and test of the first micro Coriolis mass flow sensor fully fabricated in SU-8 by photolithography processes. The sensor consists of a channel with rectangular cross-section with inner opening of 100 µm x 100 µm and is actuated at resonance by Lorentz forces. Metal tracks for the actuation current are deposited on top of the chip. The chip has been tested over a flow range of 0-800 mg/min in the case of water and 0-650 mg/min for isopropyl alcohol (IPA) to confirm that the sensor measures true mass flow (at the maximum flow of the tested range, 0-800 µl/min for both water and IPA, it results in a pressure drop of 0.98 bar for water and 1.97 bar for IPA).

5.1 Introduction

Microfluidic Lab on a Chip (LOC), integrated microfluidic systems and micro total analysis systems (µ-TAS) have gained an immense interest in the last years for many applications in different fields including (bio)chemistry, medicine and biology. Some of the goals are low cost, fast response, biocompatibility and a reduced use of reagents. Having a strong control over the fluids that are used during the experiments is essential: flow sensors are one of the key components for these types of devices.

Up to now, most micro flow sensors have been based on a thermal measurement principle [9, 158]. These sensors can measure flows down to a few nl/min [159, 160], however they are highly dependent on temperature and fluid properties, like density and specific heat [161]. As a result, the fluid has to be known, and the sensor either needs to be calibrated for each fluid or the user needs to use conversion parameters to obtain the flow rate. Flow sensors using the Coriolis flow measuring principle [162] directly measure the mass flow, independent of these parameters and thus need no recalibration or conversions and are capable of measuring flows of unknown or un-calibrated (mixtures of) fluids. Commercially available (macro) Coriolis mass flow sensors in the relevant range are available, but suffer from large internal volume and are very expensive. Recently, silicon-based micro Coriolis mass flow sensors [49, 50, 163–167] with internal volumes in the order of 10-20nl and a small footprint have been developed successfully for different flow ranges. When designed for low flow applications, one of these sensors is capable of measuring up to 20µl/min with an accuracy of 20 nl/min [165], while dedicated versions for higher flow ranges demonstrated to measure up to 300 µl/min with an accuracy of 0.4 µl/min [166]. The high sensitivity reported is due to the excellent mechanical properties of silicon and silicon nitride and the extremely thin channel wall that can be realized, resulting in a high performance flow sensor. However, the fabrication process intrinsically involves silicon micromachining which makes the sensor expensive to produce and not suitable for applications where the device is going to be used only a few times, or where it is meant to be disposable (lab-on-a-chip, diagnostics, biomedical systems, etc.).

In this chapter, it is presented a micro Coriolis mass flow sensor fully fabricated in SU-8. Although SU-8 is certainly not an obvious choice for a resonant sensor because of the high damping due to intrinsic material losses, we show that it is still possible use it for a micro Coriolis flow sensor. Trying to find a compromise between costs and accuracy, the micro SU-8 Coriolis mass flow sensor is proposed to benefit from the previously described advantages of Coriolis type mass flow sensors (insensitivity to fluid parameters, flow profile, etc.), while reducing the fabrication costs [79, 168]. Moreover, SU-8 offers other interesting features such as transparency and biocompatibility [?]. All these attractive properties make that our low-cost biocompatible mass flow sensor has a great potential in biomedical diagnostics and research.

5.2 Sensor design

5.2.1 Operating principle

Figure 5.1 shows the operation principle of a Coriolis mass flow sensor. An alternating actuation current i_a will, in the presence of a constant magnetic field B, cause Lorentz forces F_L that will actuate the channel in a torsional (twist) mode around the rotational axis noted by ω_{am} according to:

$$\overrightarrow{F_L} = L_y(\overrightarrow{i_a} \times \overrightarrow{B})$$

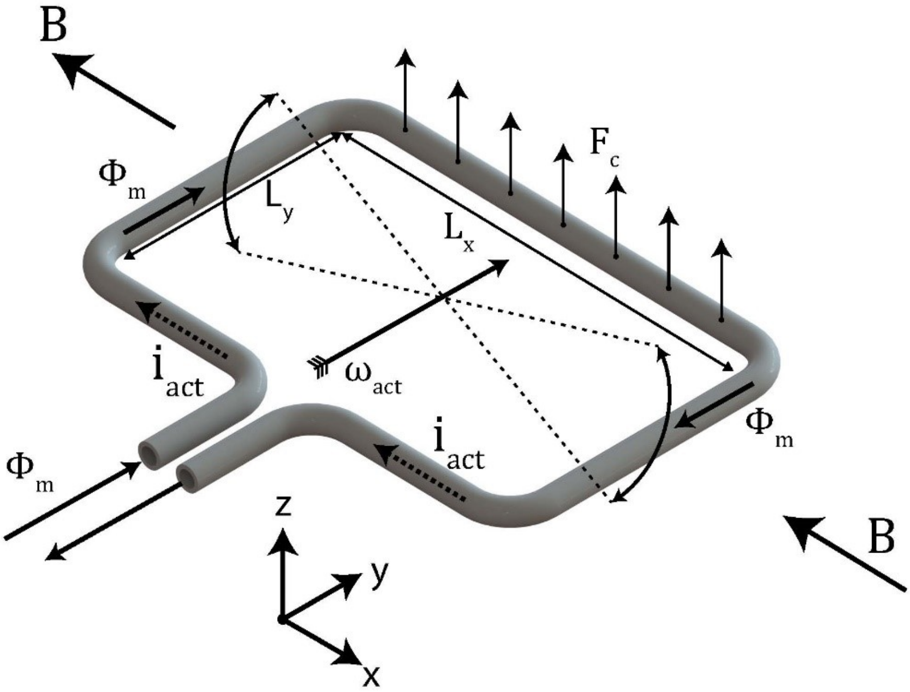

Figure 5.1. Operating principle of a Coriolis mass flow sensor actuated using Lorentz force.

A mass flow Φ_m through the channel will induce a Coriolis force F_c which is proportional to the mass flow and the angular velocity of the tube ω_{am} according to:

$$\overrightarrow{F_C} = -2L_x(\overrightarrow{\omega_{am}} \times \overrightarrow{\Phi_m})$$

The resulting Coriolis force induces an out-of-plane swing vibration mode orthogonal to the actuation mode, with amplitude proportional to the mass flow.

5.2.2 Design

The basic sensor design has been adapted from the silicon-based micro Coriolis mass flow sensor we presented in [164]. In [169], we presented a multi-axis flexible body mechanical model using the Matlab package SPACAR to model the

Parameter	**SU-8 sensor**	**Silicon sensor [COR11]**
Channel material	SU-8	Silicon-rich-nitride
Density channel material (kg/m^3)	1233	2935
Young's modulus channel material (GPa)	4.4	210
Wall thickness (µm)	100	1.5
Channel diameter (µm)	100	40
Channel volume (nl)	130	16
Resonance frequency when filled with water (kHz)	5.65	1.77
Full scale water flow at 1bar pressure drop (mg/min)	800	16.7
Capacitive read-out phase shift at full scale (degree)	1.1 (when calculated using [170])	2.4
Fabrication complexity	Low	High

Table 5.1. Comparative between the SU-8 sensor and the previous silicon sensor.

mechanical behavior of the silicon micro Coriolis mass flow sensor. This model has been adapted for the SU-8 sensor to include the possible channels shapes and the properties of SU-8 to predict the mechanical behavior of the polymer micro device. Taking into account the lower mechanical strength and rigidity of SU-8 and the reduced accuracy of the fabrication process with respect to silicon micromachining, the dimensions of the tube were adapted to compromise between sensor sensitivity and fabrication limitations. In Table 5.1 can be some of the main parameters of both Coriolis flow sensors are shown and the final design is shown in Figure 5.2. The new microfluidic chip includes a microchannel with a square internal cross-section of 100 µm by 100 µm, and channel walls of 100 µm thick. Relatively thick channel walls compared to the channel diameter where chosen due to the limitations of the SU-8 processing, but we expect that improvements in fabrication technology will allow us to reduce the wall thickness to 20 µm or less in the future. The channel window (L_x and L_y in Figure 5.2) remained at 4 mm x 2.5 mm, while external dimensions were chosen to be 10 mm x 10 mm. Compared to the silicon-based sensor [164], the sensitivity will be reduced due to the increase of wall thickness and lower stiffness compared to silicon. However, the increased inner opening is expected to allow for a much higher mass flow for a given pressure drop across the sensor.

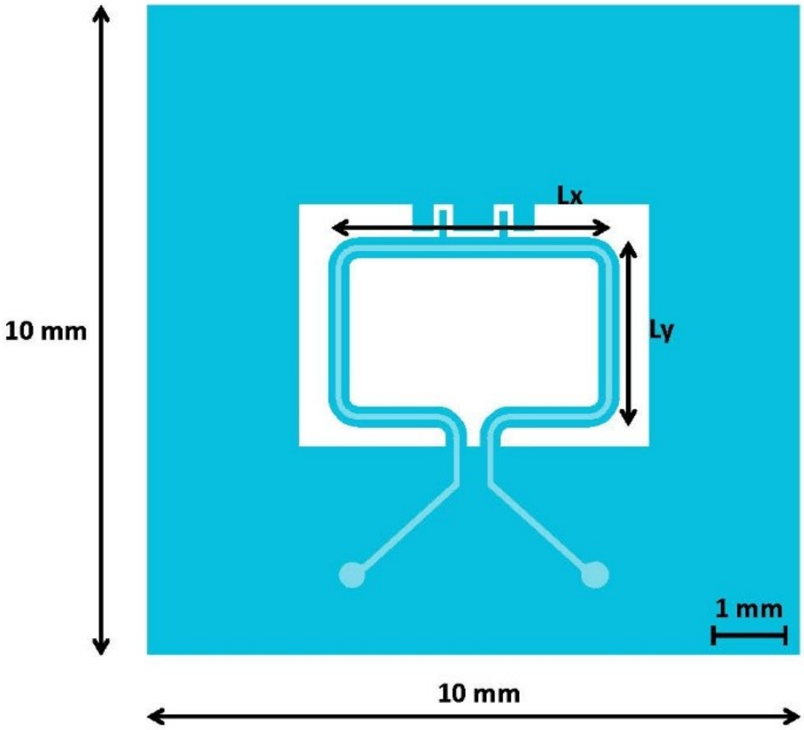

Figure 5.2. SU-8 Coriolis mass flow sensor chip design.

5.3 Fabrication

Figure 5.3 shows an outline of the process flow that was used. The process starts with the temporary bonding of a thin Kapton film (125 µm) on top of a Pyrex substrate (Figure 5.3.a). Kapton was used because of its low adhesion to SU-8, allowing the easy releasing of the devices from the substrate when their fabrication is finished. Once the Kapton film was fixed to the substrate, a 60 µm thick SU-8-50 layer was deposited on top of it. After every spinning step, a soft-bake treatment was performed. All soft-bake steps were performed by heating the wafer up to 65ºC for 30 minutes, followed by a cooling step down to room temperature. Then, another spinning of a 20 µm thick layer was performed followed by a new soft-bake step. As a result, a 90 µm thick layer was obtained. The increased thickness from the expected 80 µm was caused by the difference in surface friction: the first layer was spun on top of a Kapton film, while the second was spun over SU-8 material, increasing its expected thickness. Next, a $140mJ/cm^2$ exposure dose was used to pattern the first layer of the device using a 365 nm wavelength lamp, followed by a post-bake step (Figure 5.3.b). Every post-bake step consists on heating the wafer up to 65ºC for 15 minutes and cooling it down to room temperature. Then, two more SU-8 layers were spun (60 µm and 20 µm layer, respectively) and their corresponding soft-bakes were performed. An exposure of $140mJ/cm^2$ was then applied using the mask which defines the microchannel (Figure 5.3.c). Then, a post-bake was performed followed by a development step to remove the unexposed SU-8 material. The development consisted on an immersion of the wafer into a SU-8 developer for 5 minutes, followed by a rinsed in isopropanol, DI H2O and a drying step using nitrogen (Figure 5.3.d). As a result, an open, freely suspended microchannel was fabricated. To close the microchannel another wafer was processed. First, a 90 µm thick SU-8 layer was processed (spun and soft-baked) on top of another Kapton film temporary bonded to a Pyrex wafer (Figure 5.3.e and 5.3.f). Inlets and outlets were patterned by photolithography using the same exposure and baking parameters explained before. The wafer was finally developed (Figure 5.3.g). Then, both wafers (the bottom and the cover) were aligned and bonded to each other by applying a pressure of 1 bar and heating up to 90ºC for 15 minutes (Figure 5.3.h). Finally, the bonded SU-8 devices were manually released from the Kapton thanks to its low adhesion (Figure 5.3.i). The final thickness of the device was sufficient to be rigid enough for its easy handling, even though there is no substrate. A picture of a finished chip can be observed in Figure 5.3.j.

Once the fully SU-8 micro device is finished, electrodes are added through a metal deposition at chip level. First of all, the device is exposes to ozone plasma to ensure good adhesion between the metal and the SU-8 surface. Then, the chips are sputtered with Cr (10 nm) and Au (200 nm) using a shadow mask to define the electrodes. A working chip can be observed in Figure 5.4.

5.4 Measurements

5.4.1 Mechanical behaviour

When changing the density of the fluid passing through the sensor, a change in its resonance frequency is also expected, as it modifies the total mass of the moving structure. Figure 5.5 shows the simulated resonance frequency of the sensor for fluid densities of $0 - 1000kg/m^3$. For SU-8, a Young's modulus of 4.4 GPa and a density of $1233kg/m^3$ were used [169]. The measured resonance frequencies for water and iso-propyl alcohol (IPA) are shown in the figure as well and are within 2.5% of the simulated values, which can be explained by variations in the fabrication process. As a result, liquid density can be characterized by measuring the change in resonance frequency of the sensor. This can be especially relevant when using unknown mixtures of liquids, or chemically active substances which might change their density with time. By measuring the resonance frequency of the sensor, the flow sensor could also be used to measure the density of the fluid.

Due to the thick channel wall, the stiffness and mass of the tube will be higher than that of the silicon sensor. Furthermore, the quality factor will be lower due to the much higher material losses in SU-8. As a result, the vibration amplitude will be much lower at equal actuation current. Using a magnetic field strength at the electrical track on the tube of 0.1 T and an actuation current of 20 mA, the simulated vibration amplitude of the air-filled tube is 258 nm and measured to be 239 nm at the twist resonance frequency, compared to 54 µm with an actuation current of 5 mA for the silicon sensor. The modelled Coriolis displacement in the specified flow range will be lower by approximately 3 orders of magnitude, which is still well within the measurement accuracy of the used Polytec vibrometer.

5.4.2 Mass flow measurements

To facilitate mass flow readout using a SU-8 Coriolis sensor, a dedicated printed circuit board (PCB) with 3D printed fluidic connections was designed and fabricated. It allows straightforward fluidic and electrical connection, as well as an easy integration of permanent magnets as can be seen in Figure 5.6. Once the sensor is mounted, a Harvard Apparatus PHD Ultra syringe pump is connected to the inlet to control the applied flow rate. The outlet was connected to a waste container

To measure the mechanical displacement of the sensor induced by the Coriolis force, a Polytec MSA-400 laser Doppler vibrometer was used as shown schematically in Figure 5.7. An alternating actuation current is applied to actuate the sensor at the twist mode resonant frequency. The amplitude of the vibration is measured at two points. The mid-point amplitude (denoted with “1”) is the amplitude measured exactly on the rotational axis, where only the Coriolis induced amplitude is present and not the actuated amplitude. The edge amplitude (denoted with “2”) is the actuated amplitude. The ratio between these amplitudes is proportional to the Coriolis force and thus the mass flow.

Flow measurements have been performed using two liquids with different density: water and IPA. Results are shown in figure 8, where the reading of the sensor is plotted as a function of the applied flow rate by the syringe pump.In the case of water, the flow range has been of 0-800 mg/min with a maximum pressure drop of 0.98. For IPA, the tested flow rate has been of 0-650 mg/min which results in a maximum pressure drop of 1.97 bar. A linear relation is observed for both liquids over a range of hundreds of microliters per minute (Figure 5.8a). While both liquids appear to respond with a different slope, once the readout is converted to mass per unit of time, both plots are coincident (Figure 5.8.b), showing the clear advantage of using a Coriolis based flow sensor. Figure 5.8.c shows a typical trumpet-curve with a 5% RD accuracy and a 5% FS- zero-stability. For both liquids (water and IPA) all the points are inside the curve of the 5% FS-zero-stability, that shows that the Coriolis flow sensor based on SU-8 has less accuracy than others based on silicon, the accuracy if good enough for being used as a low cost alternative.

5.5 Discussion

The current measurement setup uses a Polytec MSA-400 laser Doppler vibrometer both for actuation and read-out. The sensors resonance frequency is found by applying a frequency sweep and measuring the edge displacement when there is no flow and then actuating the sensor at the frequency with the highest response. For each flow measurement, the edge displacement and midpoint displacement are measured separately and then divided to get the ratio between actuation and Coriolis mode amplitude. These measurements are based on three assumptions: the resonance frequency does not change during measurements; the amplitude of each point remains constant while the other point is measured and the rotational axis does not change during the measurements. Since all these parameters might be influenced by pressure and temperature, these assumptions will result in an uncertainty in the measurements. Especially for IPA, which has a relatively high viscosity and thus will a high pressure drop along the channel, these uncertainties can cause problems. Future work to reduce these uncertainties will include actuation through an oscillator circuit where the sensor is operated as two-port resonator [166] and an integrated optical or capacitive read-out.

5.6 Conclusions

We have successfully modelled, fabricated and tested a micro Coriolis mass flow sensor fully fabricated in SU-8. The sensor consists of a rectangular shaped channel with external dimensions of 4 mm x 2.5 mm. The channel has a square cross section of 300 µm x 300 µm and the channel wall thickness is 100 µm. The sensor design was based on the results of a multi-axis flexible body model in Matlab and the measured resonance frequency of the actuation mode was within 2.5% of the modelled value for two different fluids. The sensor was actuated in a resonance mode by Lorentz force actuation and read out using a laser Doppler vibrometer. The sensor showed a linear response up to 800 µl/min. Measurements with two liquids with different densities and viscosities resulted in the same mass-flow sensitivities, showing the true mass-flow sensing principle of a flow sensor of the Coriolis type.

Although the material properties of SU-8 are much less favourable for resonant sensors than *e.g.* silicon or silicon nitride, we have shown that it is still possible to use it for fabrication of a micro Coriolis mass flow sensor, resulting in a low-cost, biocompatible sensor. Future work will focus on reducing the wall thickness to channel diameter ratio, which is currently limited by the SU-8 fabrication technology. Furthermore, optical or capacitive readout structures need to be integrated on-chip, to eliminate the need for a separate vibrometer setup.

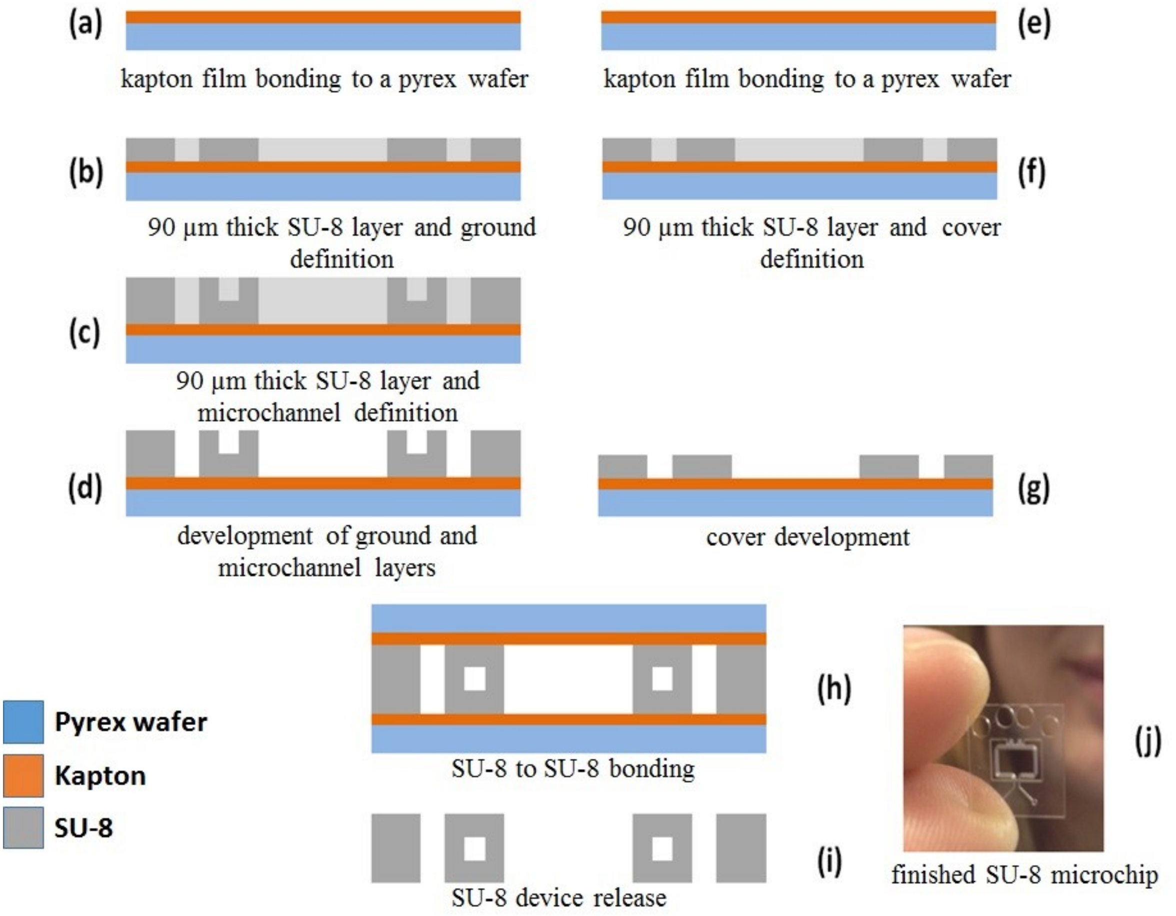

Figure 5.3. Chip fabrication process flow: (a) kapton film bonding to a pyrex wafer, (b) spinning of a 90 µm thick SU-8 layer and definition, (c) spinning of the layer and definition of microchannel, (d) development of ground and microchannel layers, (e) kapton film bonding to a pyrex wafer (f) spinning of a 90 µm thick SU-8 layer and cover definition by photolitography, (g) cover development, (h) SU-8 to SU-8 bonding, (i) SU-8 device release and (j) finished SU-8 microchip.

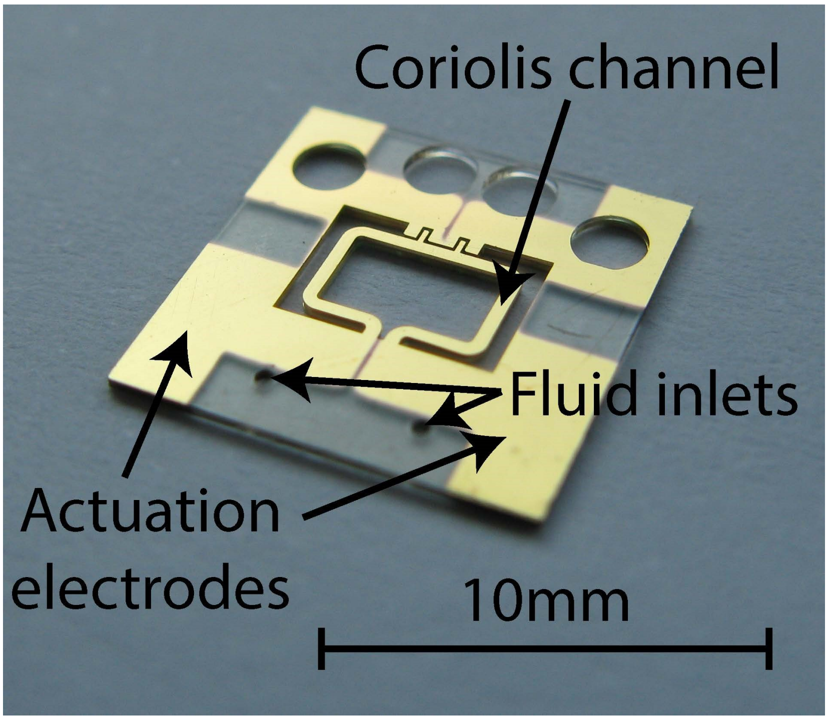

Figure 5.4. SU-8 based microfluidic chip with the defined electrodes.

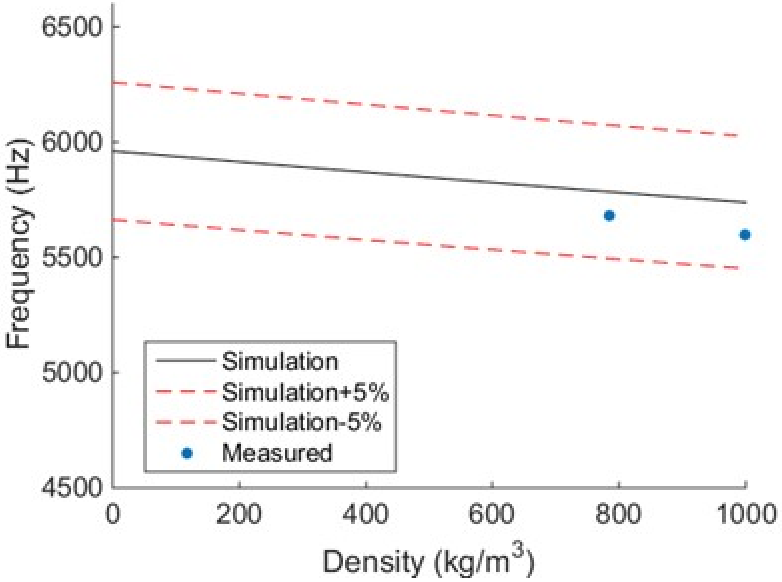

Figure 5.5. Simulated and measured resonance frequency for different densities of the fluid inside the channel.

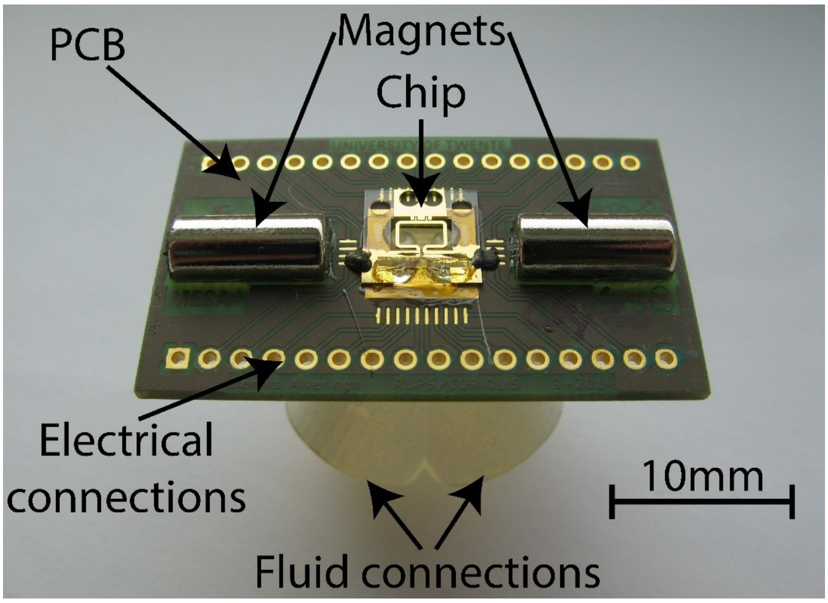

Figure 5.6. Photograph of the fabricated chip mounted on a printed circuit board.

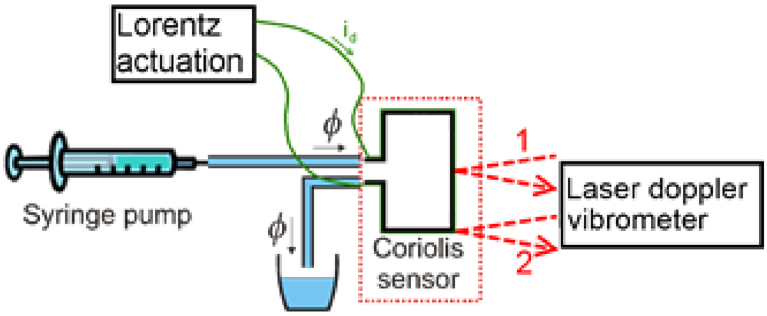

Figure 5.7. Schematic overview of the measurement setup.

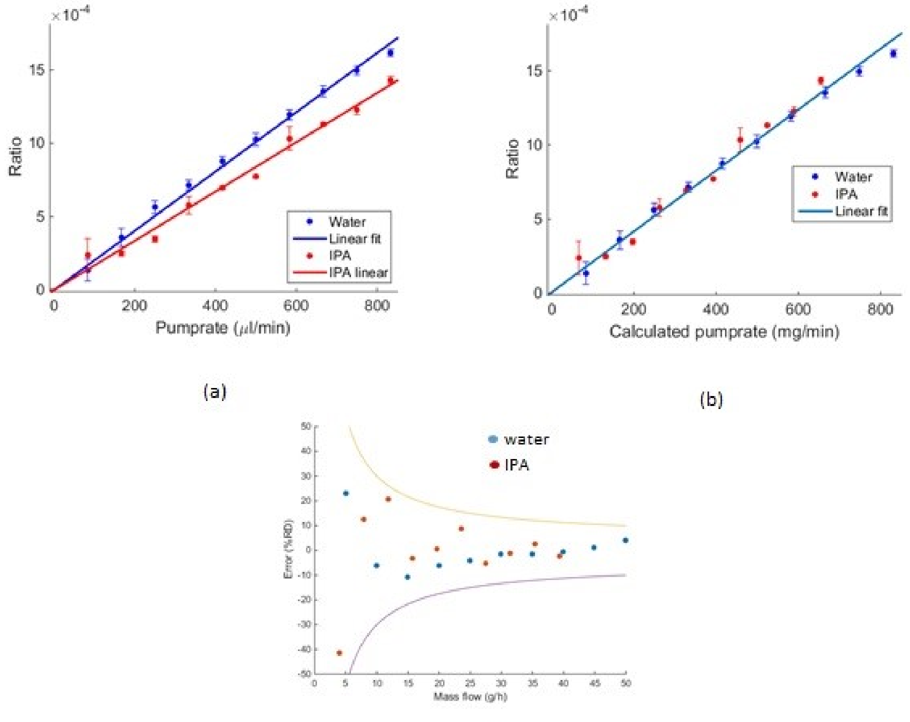

(a)

(b)

(c)

Figure 5.8. Measured ratio between mid-point and edge amplitude as a function of volume flow (a) and mass flow (b) for various fluids. (c) Trumpet-curve with 5% RD accuracy and 5% FS zero-stability for water and IPA.

Chapter 6

Conclusions

6.1 Concluding remarks

In this thesis four different microfluidic devices have been presented, based on SU-8 technology for cell culture applications in a biomimetic environment. The strategy of the use of microtechnologies and more specifically of the one based on this photoresin, is justified in all cases by the characteristics that this presents, among which it is possible to emphasize its low cost in comparison with other methods of manufacture (like micromachining) and materials (Such as silicon) and that it is an inert material and does not allow gas exchange (unlike other widely used materials such as PDMS).

Firstly, a “Lab-On-a-Chip platform was presented with a very simple design and manufacturing process, which facilitates its integration. The creation of this platform supposes to be able to have a portable device for point-of-care (POC) that allows the diagnosis of relevant analytes. In addition, our system has been shown to exhibit high sensitivity, reproducibility and specificity, thanks to the versatile silanization method for surface biofunctionalization. Part of this reproducibility is due to the fact that the construction of the device that allows the 3D microchannel network has been made in SU-8 directly on the functionalized wafer, thus avoiding the introduction of errors and reducing the variability. In addition, we ensure the perfect sealing of the devices. This mixed method of using standard silicon technologies in combination with the manufacture of the microfluidic part in polymer allows a notable reduction in manufacturing costs, which allows a step towards the mass production of this type of devices.

Focusing a little more on biomimetic devices, a device made entirely in SU-8 that allows 3D cell culture through the use of spheroids and observe the migratory effect in them has been presented. The device was carefully designed taking into account, on the one hand, the dimensions that it should have to be able to have a work area representative for the cell culture (1mm^2) and on the other hand, the integration of lateral channels that allow to see the effect of chemotaxis in our culture. These lateral channels are divided from the cell culture area by a smaller microchannels that allow both the correct confinement of the culture, and the migration mechanisms occur only by the gradient effect. With this particular application, it is demonstrated how the microdevice developed, and its application to the investigation of the migratory aptitude of multicellular spheroids is a particularly powerful tool.

Another device has also been introduced which also allows 3D culture, in this case neurospheres, which, as in the previous case, also allows by means of diffusion mechanisms to long-term culture. The device and its packaging are also designed to be compatible with real-time nuclear magnetic resonance (NMR) within a commercial equipment. In this case, in addition, the device has the novel feature of putting fiber-optic-based sensor to monitor, during the NMR test, parameters such as oxygen, pH or temperature. Thanks to the integration of the chip inside a packaging, it is possible to make a change of medium during the experiment, which has allowed the observation of necrotic area in those areas that are further away from this change of medium, a fact that also happens When histological sections are made. This fact confirms that the use of this type of device allows to perform experiments that until now, with the classic technologies could not be done, and which are also physiologically much more relevant and realistic.

Finally, an application of microtechnologies has been presented, not for a biomimetic device per se, but to develop a flow sensor that can be integrated into a complete microfluidic setup. The flow sensors based on the Coriolis effect are widely used successfully in the large industry. It is for this reason, that it was sought to use this same technology, miniaturizing it in applications for laboratory. This type of device was extremely expensive, especially for mass use, because both the raw material (silicon) and the method of manufacture (micromachining) are not economical in their own right. The first Coriolis flow sensor with SU-8 technology has been introduced here. Thanks to this method of manufacture, a mass production of these devices can be though. Although it is true that the sensitivity obtained is not as good as those made in silicon, it is sufficiently precise in the ranges of flows that are usually used in biomedical applications. It is also very interesting that it not only acts as a flow sensor, but also that it is able to detect changes in the density of the fluid, thus opening its use to other fields of application outside the scope of biomedical engineering.

In short, the use of microtechnologies in biomedical applications should be thought of as the fundamental tool to be used during this century. We must move towards more and more physiologically realistic models in order to be able to perform tests faster, more accurately and at a lower cost. The manufacturing methods that have been presented, although they are already an advance towards the mass production methods, are still of limited use and valid like laboratory prototypes. It is necessary to move towards mass production models, such as the injection of plastics with thermoplastic materials that will allow the massive use of this type of devices, providing researchers with the necessary tools, at a reasonable price, for this to be the technological revolution most important of the 21st century in the field of bioengineering and drug development.

6.2 Thesis contributions

As a result of the research conducted throughout the doctoral period, several articles have been published in journals and in proceedings of national and international conferences, as well as patents, posters and the creation of a spin off company, BEOnChip. These contributions are detailed below.

6.2.1 Journal publications

1. “Acoustophoretic isolation of tumor cells and cell clusters in extra-thin low-cost chips”. González, J. Earl, L. J. Fernández, B. Sáinz, A. Pinto, R. Monge, S. Alcalá , A. Castillejo, J.L. Soto and A. Carrato. *Lab on a Chip (submitted, December 2016).*

2. “SU-8 micro Coriolis mass flow sensor”. Rosa Monge, Jarno Groenesteijn, Dennis Alveringh , R.J. Wiegerink , Joost L tters, Luis J. Fernández. *Sensors and Actuators B: Chemical. Volume 241, 31 March 2017, Pages 744 749*

3. “Glioblastoma on a microfluidic chip: Generating pseudopalisades and enhancing aggresiveness through blood vessel obstruction events”. Jose M. Ayuso, Rosa Monge, Alicia Martínez-González, María Virumbrales-Muñoz, Guillermo A. Llamazares, Javier Berganzo, Aurelio Hernández-Laín, Jorge Santolaria, Manuel Doblaré, Christopher Hubert, Jeremy N. Rich, Pilar Sánchez-Gómez, Víctor M. Pérez-García, Ignacio Ochoa, Luis J. Fernández. *Neuro Oncology. https://doi.org/10.1093/neuonc/now230*

4. “An in vitro model for glioblastoma using microfluidics: Generating pseudopalisades on a chip”. José M. Ayuso, Rosa Monge, Alicia Martínez-González, Guillermo A. Llamazares, Javier Berganzo, Aurelio Hernández Laín, Jorge Santolaria, Manuel Doblaré, Pilar Sánchez-Gómez, Víctor M. Pérez-García, Ignacio Ochoa and Luis J. Fernández. *DOI: 10.1158/1538-7445.BRAIN15-B04*

5. “Study of the Chemotactic Response of Multicellular Spheroids in a Microfluidic Device”. Ayuso, Jose M; Basheer, Haneen A; Monge, Rosa; Sánchez-Álvarez, Pablo; Doblaré, Manuel; Shnyder, Steven D; Vinader, Victoria; Afarinkia, Kamyar; Fernández, Luis J; Ochoa, Ignacio. *PloS one, 10, 10, e0139515, 2015, Public Library of Science.*

6. “SU-8 based microdevices to study self-induced chemotaxis in 3D microenvironments”. Ayuso, José María; Monge, Rosa; Llamazares, Guillermo A; Moreno, Marco; Agirregabiria, María; Berganzo, Javier; Doblaré, Manuel; Ochoa, Ignacio; Fernández, Luis J. *Frontiers in Materials, 2, 37 ,2015 ,Frontiers.*

7. “Development of a three-dimensional cell culture system based on microfluidics for nuclear magnetic resonance and optical monitoring”. Esteve, Vicent; Berganzo, Javier; Monge, Rosa; Martínez-Bisbal, M Carmen; Villa, Rosa; Celda, Bernardo; Fernández, Luis. *Biomicrofluidics, 8, 6, 064105, 2014, AIP Publishing.*

8. “Design, manufacture and geometric verification of rapid prototyped microfluidic encapsulations by computed tomography”. Santolaria, Jorge; Monge, Rosa; Tobajas, Ángel; Jiménez, Roberto; Cabrera, Mirko A; Fernández, Luis J. *Computers in Industry, 64, 9, 1138-1151, 2013, Elsevier.*

9. “Nanophotonic lab-on-a-chip platforms including novel bimodal interferometers, microfluidics and grating couplers”. Duval, Daphné; González-Guerrero, Ana Belén; Dante, Stefania; Osmond, Johann; Monge, Rosa; Fernández, Luis J; Zinoviev, Kirill E; Domínguez, Carlos; Lechuga, Laura M. *Lab on a Chip, 12, 11, 1987-1994, 2012, Royal Society of Chemistry.*

6.2.2 Patents

1. 2016. Dispositivo conector para circuitos microfluídicos P201631295. Licensed patent to BEONCHIP S.L.

2. 2016. SU-8 micro Coriolis mass flow sensor. J. Groenesteijn, L.J. Fernández Ledesma, R. Monge Prieto, I. Ochoa Garrido, R.J. Wiegerink. The Netherlands N2016265
3. 2015. Dispositivo y sistema microfluídico para el estudio de cultivos celulares. Rosa Monge, Luis J Fernández, Jose María Ayuso, Guillermo Llamazares, María Virumbrales, Jorge Santolaria, Ignacio Ochoa. Spain P201531607. Licensed patent to BEONCHIP S.L.2015. Chip microfluídico, dispositivo microfluídico, procedimientos y usos asociados Rosa Monge, Luis J Fernández, José Luis Calavia, Jorge Santolaria, Ignacio Ochoa, Javier Orús, Carlos Peribáñez, José Manuel Rodriguez. Spain P201531539
4. 2015. Chip microfluídico, dispositivo microfluídico, procedimientos y usos asociados Rosa Monge, Luis J Fernández, José Luis Calavia, Jorge Santolaria, Ignacio Ochoa, Javier Orús, Carlos Peribáñez, José Manuel Rodríguez. Spain P201531539
5. 2013. Dispositivo microfluídico para cultivo celular biomimético 3D basado en el uso de una membrana porosa que separa dos cámaras con control fluídico independiente. Luis J. Fernández Ledesma, Rosa Monge, Ignacio Ochoa, Guillermo Llamazares. Transfer of know-how. Licensed to EBERS Medical Technology S.L.
6. 2012. Dispositivo de cultivo celular y método asociado a dicho dispositivo Rosa Monge, Luis J. Fernández, Guillermo A. Llamazares, Jorge Santolaria, Ignacio Ochoa, Aitor Aguilar, Rebeca Guerrero. Spain P201230911-PCT/ES13/000141. Licensed patent to BEONCHIP S.L.

6.2.3 Spin Off Company creation & recognitions

During my Ph.D., I focused my research in the development of microtechnologies for cell culture applications. With this knowledge and with the aim of bringing the research generated in the academia to market, I founded in February 2016 **BEONCHIP S.L.**, a company dedicated to the design, manufacture and commercialization of microfluidic devices for cell culture in biomimetic environment. Our devices represent a new paradigm in cell culture: the possibility to recreate the same environment that cells have in a living body, but in your laboratory. The benefits that my work can bring to society range from reducing animal testing to the faster development of new personalized drugs.

1. 2016 H2020-SME Instruments Phase 1. Body-On-A-Chip Project.

2. 2016 EUROSTARS Project (EUREKA program). “BONAFIDE: Bone-On-Chip Analysis Platform for In vitro Drug Performance Evaluation”. Participating and project coordinator.
3. 2016 RETOS (Plan Estatal de Investigación Científica y Técnica y de la Innovación). Desarrollo de un Sistema de preservaci n normotérmica con capacidad de monitorización metabólica no invasiva (PRENOMON). Participating.
4. 2016 Finalist. Campus IBERUS Award. BEONCHIP S.L. November 2016
5. 2016 Finalist. EMPRENDEDOR XXI (LaCaixa) Award. 3rd finalist, Aragón, BEONCHIP S.L. October 2016.
6. 2016 Spin off recognition. University of Zaragoza. September 2016.
7. 2016 Finalist. EVERIS awards 2016.
8. 2016 SPINUP Phase II. University of Zaragoza. BEONCHIP S.L.
9. 2016 Winner “Generando Futuro” Award. V Edition. BEONCHIP Project.
10. 2015 Winner IDEA Award XXII Edition. Best Product. BEONCHIP Project.
11. 2015 SPINUP Phase I. University of Zaragoza.BEONCHIP Project.

Appendices

Chapter 7

Conclusiones

7.1 Observaciones finales

En esta tesis se han presentado cuatro dispositivos microfluídicos diferentes, basados en tecnología de SU-8 para aplicaciones en cultivo celular en ambiente biomimético. La estrategia del uso de microtecnologías y más concretamente de la basada en esta fotorresina, está justificada en todos los casos por las características que esta presenta, entre las que cabe destacar su bajo coste en comparación con otros métodos de fabricacín (como *micromachining*) y materiales (como el silicio), por resultar un material inerte y que no permite el intercambio gaseoso (a diferencia de otros materiales ampliamente utilizados, como el PDMS).

En primer lugar, se ha presentado una plataforma "Lab-On-a-Chip con un diseño y proceso de fabricación muy simples, lo que facilita su integración. La creación de esta plataforma supone poder tener un dispositivos portables para diagnóstico (point-of-care, POC) que permite el diagnostico de relevantes analitos. Además, se ha demostrado que nuestro sistema presenta alta sensibilidad, reproducibilidad and especificidad, gracias a el versátil médodo de silinización para la biofuncionalización de superficies. Parte de esta reproducibilidad se debe a que la construcción del dispositivo que permite tener un entorno de microcanales en 3D, que se ha realizado en SU-8 directamente sobre la oblea funcionalizada, evitando de esta manera la introducción de errores y reduciendo la variabilidad. Además, nos aseguramos el sellado perfecto de los dispositivos. Este método mixto de utilizar tecnologías estándar de silicio en combinación con la fabricación de la parte microfluídica en polímero, permite una notable reducción en costes de fabricación, lo que permite dar un paso hacia la producción en masa de este tipo de dispositivos.

Centrándonos un poco más en lo que son los dispositivos biomiméticos, se ha presentado un dispositivo fabricado íntegramente en SU-8 que permite el cultivo celular 3D mediante el uso de esferoides y observar el efecto migratorio en ellos. El dispositivo fue cuidadosamente diseñado teniendo en cuenta, por un lado, las dimensiones que debería tener para poder tener un área de trabajo representativa para el cultivo (1mm^2) y, por otro lado, la integración de unos canales laterales por lo que poder hacer pasar líquidos, reactivos, etc que permitan ver el efecto de la chemotacsis en nuestro cultivo. Estos canales laterales están divididos del área de cultivo por unos microcanales más pequeño que permiten tanto el correcto confinamiento del cultivo, como que los mecanismos de migración se produzcan únicamente al efecto de gradiente. Con esta aplicación en concreto, queda demostrada cómo el microdispositivo desarrollado y su aplicación en la migración de esferoides multicelulares una herramienta altamente poderosa.

También se ha presentado otro dispositivo que también permite el cultivo 3D, en este caso de neuroesferas, que al igual que en el caso anterior, también permite mediante mecanismos de difusión en cultivo a largo plazo. El dispositivo y su correspondiente encapsulado, son diseñados también de manera que sea compatible con la resonancia nuclear magnética (RMN) a tiempo real, dentro de un equipo comercial. En este caso, además, el dispositivo presenta la novedosa característica de poner integrar en el propio dispositivo a sensor de fibra óptica que permite monitorizar, durante el ensayo en el RMN, parámetros como el oxígeno, pH o temperatura. Gracias a la integración del chip dentro de un encapsulado, es posible realizar un cambio de medio durante la realización del experimento, lo que ha permitido la observación de zona necrótica en aquellas áreas que quedan más lejos de este cambio de medio, hecho que también sucede cuando se realizan cortes histológicos. Este hecho, viene a confirmar que el uso de este tipo de dispositivos permite realizar experimentos que hasta ahora, con las tecnologías clásicas no se podían realizar, y que además son fisiológicamente mucho más relevantes y realistas.

Por último, se ha presentado una aplicación de microtecnologías, no para un dispositivos biomimético en sí mismo, si no para desarrollar un sensor de flujo que pueda ser integrable en un setup microfluídico completo. Los sensores de flujos basados en el efecto Coriolis son ampliamente utilizados con éxito en la gran industria. Es por ello, por lo que se buscó utilizar esta misma tecnología, miniaturizándola en aplicaciones para laboratorio. Este tipo de dispositivos resultaban enormemente caros, sobre todo para su uso masivo, debido a que tanto la materia primar (silicio) como el método de fabricación de los mismos (micromachining) no resultan económicos por sí mismos. Aquí se ha presentado el primer sensor de flujo Coriolis con tecnología SU-8. Gracias a este método de fabricación, se puede pensar en una producción de manera masiva. Aunque bien es cierto, que la sensibilidad obtenida no es tan buena como en los fabricados en silicio, sí que resulta suficientemente precisa en los rangos de flujos que habitualmente se utilizan en las aplicaciones biomédicas. Resulta muy interesante también el hecho de que no sólo actúe como sensor de flujo, sino que también sea capaz de detectar cambios en la densidad del fluido, abriéndose de esta manera su uso a otros campos de aplicación fuera del ámbito de la ingeniería biomédica.

En resumen, el uso de las microtecnologías en aplicaciones biomédicas debe ser pensada como la herramienta fundamental a utilizar durante este siglo. Se debe caminar hacia modelos cada vez más fisiológicamente realistas para poder realizar ensayos de manera más rápida, más precisa y con menor coste. Los métodos de fabricación que se han presentado, aunque ya resultan un avance hacia los métodos de fabricación masivos, son aún de uso limitado y válidos como prototipos de laboratorio. Hay que moverse hacia modelos de fabricación en masa, como la inyección de plásticos con materiales termoplásticos que permitirán el uso masivo de este tipo de dispositivos, dotando a los investigadores de las herramientas necesarias, a un precio razonable, para que esta sea la revolución tecnológica más importante del siglo 21 en el campo de la bioingeniería y el desarrollo de fármacos.

7.2 Contribuciones de la tesis

Como resultado de la investigación realizada durante la tesis doctoral, diversos artículos científicos han sido publicados así como pósters y comunicaciones orales en conferencias tanto nacionales como internacionales, patentes y la creación de una *spin off*, BEOnChip. Estas contribuciones están detalladas a continuación.

7.2.1 Publicaciones científicas

1. "Acoustophoretic isolation of tumor cells and cell clusters in extra-thin low-cost chips". González, J. Earl, L. J. Fernández, B. Sáinz, A. Pinto, R. Monge, S. Alcalá , A. Castillejo, J.L. Soto and A. Carrato. *Lab on a Chip (submitted, December 2016).*
2. "SU-8 micro Coriolis mass flow sensor". Rosa Monge, Jarno Groenesteijn, Dennis Alveringh , R.J. Wiegerink , Joost L tters, Luis J. Fernández. *Sensors and Actuators B: Chemical. Volume 241, 31 March 2017, Pages 744 749*
3. "Glioblastoma on a microfluidic chip: Generating pseudopalisades and enhancing aggresiveness through blood vessel obstruction events". Jose M.

Ayuso, Rosa Monge, Alicia Martínez-González, María Virumbrales-Muñoz, Guillermo A. Llamazares, Javier Berganzo, Aurelio Hernández-Laín, Jorge Santolaria, Manuel Doblaré, Christopher Hubert, Jeremy N. Rich, Pilar Sánchez-Gómez, Víctor M. Pérez-García, Ignacio Ochoa, Luis J. Fernández. *Neuro Oncology. https://doi.org/10.1093/neuonc/now230*

4. “An in vitro model for glioblastoma using microfluidics: Generating pseudopalisades on a chip”. José M. Ayuso, Rosa Monge, Alicia Martínez-González, Guillermo A. Llamazares, Javier Berganzo, Aurelio Hernández Laín, Jorge Santolaria, Manuel Doblaré, Pilar Sánchez-Gómez, Víctor M. Pérez-García, Ignacio Ochoa and Luis J. Fernández. *DOI: 10.1158/1538-7445.BRAIN15-B04*

5. “Study of the Chemotactic Response of Multicellular Spheroids in a Microfluidic Device”. Ayuso, Jose M; Basheer, Haneen A; Monge, Rosa; Sánchez-Álvarez, Pablo; Doblaré, Manuel; Shnyder, Steven D; Vinader, Victoria; Afarinkia, Kamyar; Fernández, Luis J; Ochoa, Ignacio. *PloS one, 10, 10, e0139515, 2015, Public Library of Science.*

6. “SU-8 based microdevices to study self-induced chemotaxis in 3D microenvironments”. Ayuso, José María; Monge, Rosa; Llamazares, Guillermo A; Moreno, Marco; Agirregabiria, María; Berganzo, Javier; Doblaré, Manuel; Ochoa, Ignacio; Fernández, Luis J. *Frontiers in Materials, 2, 37 ,2015 ,Frontiers.*

7. “Development of a three-dimensional cell culture system based on microfluidics for nuclear magnetic resonance and optical monitoring”. Esteve, Vicent; Berganzo, Javier; Monge, Rosa; Martínez-Bisbal, M Carmen; Villa, Rosa; Celda, Bernardo; Fernández, Luis. *Biomicrofluidics, 8, 6, 064105, 2014, AIP Publishing.*

8. “Design, manufacture and geometric verification of rapid prototyped microfluidic encapsulations by computed tomography”. Santolaria, Jorge; Monge, Rosa; Tobajas, Ángel; Jiménez, Roberto; Cabrera, Mirko A; Fernández, Luis J. *Computers in Industry, 64, 9, 1138-1151, 2013, Elsevier.*

9. “Nanophotonic lab-on-a-chip platforms including novel bimodal interferometers, microfluidics and grating couplers”. Duval, Daphné; González-Guerrero, Ana Belén; Dante, Stefania; Osmond, Johann; Monge, Rosa; Fernández, Luis J; Zinoviev, Kirill E; Domínguez, Carlos; Lechuga, Laura M. *Lab on a Chip, 12, 11, 1987-1994, 2012, Royal Society of Chemistry.*

7.2.2 Patentes

1. 2016. Dispositivo conector para circuitos microfluídicos P201631295. Licensed patent to BEONCHIP S.L.
2. 2016. SU-8 micro Coriolis mass flow sensor. J. Groenesteijn, L.J. Fernández Ledesma, R. Monge Prieto, I. Ochoa Garrido, R.J. Wiegerink. The Netherlands N2016265
3. 2015. Dispositivo y sistema microfluídico para el estudio de cultivos celulares. Rosa Monge, Luis J Fernández, Jose María Ayuso, Guillermo Llamazares, María Virumbrales, Jorge Santolaria, Ignacio Ochoa. Spain P201531607. Licensed patent to BEONCHIP S.L.2015. Chip microfluídico, dispositivo microfluídico, procedimientos y usos asociados Rosa Monge, Luis J Fernández, José Luis Calavia, Jorge Santolaria, Ignacio Ochoa, Javier Orús, Carlos Peribáñez, José Manuel Rodriguez. Spain P201531539
4. 2015. Chip microfluídico, dispositivo microfluídico, procedimientos y usos asociados Rosa Monge, Luis J Fernández, José Luis Calavia, Jorge Santolaria, Ignacio Ochoa, Javier Orús, Carlos Peribáñez, José Manuel Rodríguez. Spain P201531539
5. 2013. Dispositivo microfluídico para cultivo celular biomimético 3D basado en el uso de una membrana porosa que separa dos cámaras con control fluídico independiente. Luis J. Fernández Ledesma, Rosa Monge, Ignacio Ochoa, Guillermo Llamazares. Transfer of know-how. Licensed to EBERS Medical Technology S.L.
6. 2012. Dispositivo de cultivo celular y método asociado a dicho dispositivo Rosa Monge, Luis J. Fernández, Guillermo A. Llamazares, Jorge Santolaria, Ignacio Ochoa, Aitor Aguilar, Rebeca Guerrero. Spain P201230911-PCT/ES13/000141. Licensed patent to BEONCHIP S.L.

7.2.3 Creación de empresa *spin off* y reconocimientos

Durante el doctorado, he focalizado mi investigación en el desarrollo de microtecnologías para aplicaciones en cultivo celular. Con este conocimiento y con la intención de que la investigación generada en la universidad se pueda introducir en el mercado, fundé en febrero de 2016 **BEONCHIP S.L.**, una empresa dedicada al diseño, fabricación y comercialización de dispositivos microfluídicos para cultivo celular en ambientes biomiméticos. Nuestros dispositivos representan un nuevo paradigma en el cultivo celular: la posibilidad de recrear el mismo ambiente que tienen las células en un ser vivo, pero en el laboratorio. Los beneficios que este trabajo puede traerle a la sociedad van desde la reducción de la experimentación animal, a el rápido desarrollo de fármacos personalizados.

1. 2016 H2020-SME Instruments Phase 1. Body-On-A-Chip Project.
2. 2016 EUROSTARS Project (EUREKA program). “BONAFIDE: Bone-On-Chip Analysis Platform for In vitro Drug Performance Evaluation”. Participantes y coordinadores del proyecto.
3. 2016 RETOS (Plan Estatal de Investigación Científica y Técnica y de la Innovación). Desarrollo de un Sistema de preservaci n normotérmica con capacidad de monitorización metabólica no invasiva (PRENOMON). Participantes.
4. 2016 Finalista. Campus IBERUS. BEONCHIP S.L. Noviembre 2016
5. 2016 Finalista. EMPRENDEDOR XXI (LaCaixa). Tercer finalista, Aragón, BEONCHIP S.L. Octubre 2016.
6. 2016 Spin off reconocimiento. Universidad de Zaragoza. Septiembre 2016.
7. 2016 Finalista. EVERIS 2016.
8. 2016 SPINUP fase II. Universidad de Zaragoza. BEONCHIP S.L.
9. 2016 Ganador “Generando Futuro”. V Edición. BEONCHIP Proyecto. .
10. 2015 Ganador Premio IDEA XXII Edición. Mejor producto. BEONCHIP Proyecto.
11. 2015 SPINUP fase I. Universidad de Zaragoza. BEONCHIP Proyecto.

Bibliography

Bibliography

[1] Craighead H. G. Berg A. and Yang P.-D. From microfluidic applications to nanofluidic phenomena. Chem. Soc. Rev., (39):899–900, 2010.

[2] Tian W.-C. and Finehout E. Current and Future Trends in Microfluidics within Biotechnology Research., chapter Chapter 11. Lee A. P. and Lin G., Eds., Springer, 2008.

[3] Whitesides G. M. The origins and the future of microfluidics. Nature., (442):368–373, 2006.

[4] Dertinger S. K. W. Ajdari A. Mezic I. Stone H. A. Stroock A. D. and Whitesides G. M. Chaotic mixer for microchannels. Science., (295):647–651, 2002.

[5] Bu M. Evans A. G. R. Husband B. and Melvin T. Investigation for the operation of an integrated peristaltic micropump. J. Micromech. Microeng., (14):S64–S69, 2004.

[6] Chou H. P. Thorsen T. Scherer A. Unger M. A. and Quake S. R. Monolithic microfabricated valves and pumps by multilayer soft lithography. Science., (288):113–116, 2000.

[7] Maerkl S. J. Thorsen T. and Quake S. R. Microfluidic large-scale integration. Science., (298):580–584, 2002.

[8] Geschke O. Jorgensen A. M. Kristensen A. Kutter J. P. Mogensen K. B. Balslev S., Bilenberg B. and Snakenborg D. Fully integrated optical system for lab-on-a-chip applications. in Proc. IEEE Int. Conf. on Micro Electro Mechanical Systems, MEMS., pages 89–92, 2004.

[9] E. Meng J.T.W. Kuo, L. Yu. Micromachined thermal flow sensors—a review. Micromachines, (3):550–573.

[10] C.M. Chang C.P. Lin C.H. Lin L.M. Fu C.Y. Lee Y.H. Wang, C.P. Chen. Mems-based gas flow sensors. Microfluid. Nanofluid., (6):333–346, 2009.

[11] Jerman J. H. Terry S. C. and Angell J. B. A gas chromatographic air analyzer fabricated on a silicon wafer. IEEE Trans. Electron Devices., (26):1880–1886, 1979.

[12] Fluri K. Seiler K. Fan Z.-H. Effenhauser C. S. Harrison S. J. and Manz A. Micromachining a miniaturized capillary electrophoresis-based chemical analysis system on a chip. Science., (261):895–897, 1993.

[13] Davidson J. C. Raley N. F. and Balch J. W. Examination of glass-silicon and glass-glass bonding techniques for microfluidic systems. Proc. SPIE., (2639):41–45, 1995.

[14] Mello A. J. D. Kopp M. U. and Manz A. Chemical amplification: continuous-flow pcr on a chip. Science., (280):1046–1048, 1998.

[15] Stjernstrom M. and Roeraade J. Method for fabrication of microfluidic systems in glass. J. Micromech. Microeng., (8):33–38, 1998.

[16] Wang C. Skinner C. Colyer K. Harrison D. Li J. Bings N. and Thibault P. Microfluidic devices connected to glass capillaries with minimal dead volume. Anal. Chem., (71):3292–3296, 1999.

[17] Benoit V. Aitchison J. S. Ruano J. M. and Cooper J. M. Flame hydrolysis deposition of glass on silicon for the integration of optical and microfluidic devices. Anal. Chem., (72):1093–1097, 2000.

[18] Skelley A. M. Liu C. N. Lagally E. T. Grover W. H. and Mathies R. A. Monolithic membrane valves and diaphragm pumps for practical large-scale integration into glass microfluidic devices. Sens. Actuators B., (89):315–323, 2003.

[19] Fang Q. Jia Z.-J. and Fang Z.-L. Bonding of glass microfluidic chips at room temperatures. Anal. Chem., (76):5597–5602, 2004.

[20] Sugioka K. Cheng Y. and Midorikawa K. Microfluidic laser embedded in glass by three-dimensional femtosecond laser microprocessing. Opt. Lett., (29):2007–2009, 2004.

[21] Melvin T. Ensell G. J. Wilkinson J. S. Bu M.-Q. A new masking technology for deep glass etching and its microfluidic application. Sens. Actuators B., (115):476–482, 2004.

[22] Allen P. B. and Chiu D. T. Calcium-assisted glass-to-glass bonding for fabrication of glass microfluidic devices. Anal. Chem., (80):7153–7157, 2008.

[23] Albrecht B. Vulto P., Huesgen T. and Urban G. A. A full-wafer fabrication process for glass microfluidic chips with integrated electroplated electrodes by direct bonding of dry film resist. J. Micromech. Microeng., (19), 2009.

[24] Christina H. Tu David H. Cribbs Carl W. Cotman Seog Woo Rhee, Anne M. Taylor and Noo Li Jeon. Patterned cell culture inside microfluidic devices. Lab On a Chip, (5):102–107, 2005.

[25] Lin F Minh-Canh Nguyen C et al. Wang SJ, Saadi W. Differential effects of egf gradient profiles on mda-mb-231 breast cancer cell chemotaxis. Exp Cell Res, (300):180–189, 2004.

[26] Lin F Nandagopal S, Wu D. Combinatorial guidance by ccr7 ligands for t lymphocytes migration in co-existing chemokine fields. PLoS One, (6: e18183), 2011.

[27] B.C. Pemble, C.M.; Towe. A miniature shape memory alloy pinch valve. Sens. Actuat. A, (77):145–148, 1999.

[28] A.C.; Lee A.; George-A.H.; Whitesides G.M. Weibel, D.B.; Siegel. Pumping fluids in microfluidic systems using the elastic deformation of poly(dimethylsiloxane). Lab On a Chip, (7):1832–1836, 2007.

[29] M.; Potenta S.; Sia-S.K.; Lee A.; Whitesides G.M. Weibel, D.B.; Kruithof. Torque-actuated valves for microfluidics. Anal. Chem., (77):4726–4733, 2005.

[30] S.; Backhouse C.J. Pilarski, P.M.; Adamia. An adaptable microvalving system for on-chip polymerase chain reactions. J. Immunol. Meth., (305):48–58, 2005.

[31] D.; Berlin A.A. Sundararajan, N.; Kim. Microfluidic operations using deformable polymer membranes fabricated by single layer soft lithography. Lab On a Chip, (5):350–354, 2005.

[32] H.; Drechsler U.; Wolf-H.; Wolf M.; Michel B.; de Rooij N.; Delamarche E. Juncker, D.; Schmid. Autonomous microfluidic capillary system. Anal. Chem., (74):6139–6144, 2002.

[33] D.J. Walker, G.M.; Beebe. A passive pumping method for microfluidic devices. Lab On a Chip, (2):131–134, 2002.

[34] G.; Pandolfi A.; Ortiz-M.; Anderson W.F.; Quake S.R. Studer, V.; Hang. Scaling properties of a low-actuation pressure microfluidic valve. J. Appl. Phys., (95):393–398, 2004.

[35] J.; Lee K.; Park-Y.; Sun K.; Lee T.; Lee S. Kim, J.; Baek. Photopolymerized check valve and its integration into a pneumatic pumping system for biocompatible sample delivery. Lab On a Chip, (6):1091–1094, 2006.

[36] F.C.M.; Bouwstra S. Vanlintel, H.T.G.; Vandepol. A piezoelectric micropump based on micromachining of silicon. Sens. Actuat., (15):153–167, 1988.

[37] J.G. Smits. Piezoelectric micropump with 3 valves working peristaltically. Sens. Actuat. A, (21):203–206, 1990.

[38] X.Y.; Futai N.; Cho-B.S.; Takayama S. Gu, W.; Zhu. Computerized microfluidic cell culture using elastomeric channels and braille displays. Proc. Natl. Acad. Sci. USA, (101):15861–15866, 2004.

[39] W.; Song J.W.; Takayama-S. Futai, N.; Gu. Handheld recirculation system and customized media for microfluidic cell culture. Lab On a Chip, (6):149–154, 2006.

[40] W.; Bergveld P. Bohm, S.; Olthuis. An integrated micromachined electrochemical pump and dosing system. Biomed. Microdevices, (1):121–130, 1999.

[41] B.; Olthuis W.; Bergveld-P. Bohm, S.; Timmer. A closed-loop controlled electrochemically actuated micro-dosing system. J. Micromech. Microeng., (10):498–504, 2000.

[42] S.; Cady N.; Batt-C. Lui, C.; Stelick. Low-power microfluidic electro-hydraulic pump (ehp). Lab On a Chip, (10):10–79, 2010.

[43] M.I.; Horwitz J.S.; Kabler-M.N.; Auyeung R.C.Y.; Kim W.J. Rife, J.C.; Bell. Miniature valveless ultrasonic pumps and mixers. Sens. Actuat. A, (86):135–140, 2000.

[44] A.P. Tovar, A.R.; Lee. Lateral cavity acoustic transducer. Lab On a Chip, (9):41–43, 2009.

[45] M.V.; Tovar A.R.; Okabe-Y. Lee, A.P.; Patel. Microfluidic air-liquid cavity acoustic transducers for on-chip integration of sample preparation and sample detection. J. Assoc. Lab. Autom., (15):449–454, 2010.

[46] M.V.; Lee A.P. Tovar, A.R.; Patel. Lateral air cavities for microfluidic pumping with the use of acoustic energy. Microfluid. Nanofluid. doi: 10.1007/s10404-010-0758-1., 2011.

[47] E.F.-C. Meng. Mems technology and devices for a microfluid dosing system. ph.d. dissertation,. California Institute of Technology, Pasadena, CA, USA,, page 150, 2003.

[48] Wiegerink RJ Groenesteijn J Haneveld J. Lammerink TSJ, Lötters JC. Single chip flow sensing system with a dynamic flow range of more than 4 decades. Solid-State Sensors, Actuators and Microsystems Conference (TRANSDUCERS),, (3):p. 890, 2011.

[49] D. Riley N. Najafi R. Smith, D. Sparks. A mems based coriolis mass flow sensor for industrial applications. IEEE Trans. on Industrial Electronics, (56):1066–1071, 2009.

[50] M. Dijkstra H. Droogendijk M.J. de Boer R.J. Wiegerink J. Haneveld, T.S.J. Lammerink. Highly sensitive micro coriolis mass flow sensor. Proceedings MEMS, pages 920–923, 2008.

[51] Nguyen NT. Micromachined flow sensors—a review. Flow Meas Instrum., page 8(1):7 16., 1997.

[52] Boisen A. Noeth N, Keller SS. Integrated cantilever-based flow sensors with tunable sensitivity for in-line monitoring of flow fluctuations in microfluidic systems. Sensors., (14(1):229 44.), 2013.

[53] Qin L Chyu MK Wang Q-M. Wang Y, Li Z. Theoretical and experimental studies of a surface acoustic wave flow sensor. IEEE Trans Ultrason Ferroelectr Freq Control., (59(3):481 90.), 2012.

[54] Curtis D Chin, Vincent Linder, and Samuel K Sia. Lab-on-a-chip devices for global health: Past studies and future opportunities. Lab on a Chip, 7(1):41–57, 2007.

[55] Frances S Ligler. Perspective on optical biosensors and integrated sensor systems. Analytical chemistry, 81(2):519–526, 2008.

[56] Maria A Schwarz and Peter C Hauser. Recent developments in detection methods for microfabricated analytical devices. Lab on a Chip, 1(1):1–6, 2001.

[57] Joseph Wang. Electrochemical biosensors: towards point-of-care cancer diagnostics. Biosensors and Bioelectronics, 21(10):1887–1892, 2006.

[58] M-Carmen Estevez, Mar Alvarez, and Laura M Lechuga. Integrated optical devices for lab-on-a-chip biosensing applications. Laser & Photonics Reviews, 6(4):463–487, 2012.

[59] Amanda Kussrow, Carolyn S Enders, and Darryl J Bornhop. Interferometric methods for label-free molecular interaction studies. Analytical chemistry, 84(2):779–792, 2011.

[60] Katrien De Vos, Jordi Girones, Tom Claes, Yannick De Koninck, Stepan Popelka, Etienne Schacht, Roel Baets, and Peter Bienstman. Multiplexed antibody detection with an array of silicon-on-insulator microring resonators. IEEE Photonics Journal, 1(4):225–235, 2009.

[61] D-X Xu, M Vachon, A Densmore, R Ma, A Delâge, S Janz, J Lapointe, Y Li, G Lopinski, D Zhang, et al. Label-free biosensor array based on silicon-on-insulator ring resonators addressed using a wdm approach. Optics letters, 35(16):2771–2773, 2010.

[62] K Cottier, M Wiki, G Voirin, H Gao, and RE Kunz. Label-free highly sensitive detection of (small) molecules by wavelength interrogation of integrated optical chips. Sensors and Actuators B: Chemical, 91(1):241–251, 2003.

[63] Jaime García-Rupérez, Veronica Toccafondo, María José Bañuls, Javier García Castelló, Amadeu Griol, Sergio Peransi-Llopis, and Ángel Maquieira. Label-free antibody detection using band edge fringes in soi planar photonic crystal waveguides in the slow-light regime. Optics Express, 18(23):24276–24286, 2010.

[64] Aurel Ymeti, Jan Greve, Paul V Lambeck, Robert Wijn, Rene G Heideman, and Johannes S Kanger. Drift correction in a multichannel integrated optical young interferometer. Applied optics, 44(17):3409–3412, 2005.

[65] Kirill Zinoviev, Laura G Carrascosa, José Sánchez del Río, Borja Sepúlveda, Carlos Domínguez, and Laura M Lechuga. Silicon photonic biosensors for lab-on-a-chip applications. Advances in Optical Technologies, 2008, 2008.

[66] Frank B Myers and Luke P Lee. Innovations in optical microfluidic technologies for point-of-care diagnostics. Lab on a Chip, 8(12):2015–2031, 2008.

[67] Xudong Fan and Ian M White. Optofluidic microsystems for chemical and biological analysis. Nature photonics, 5(10):591–597, 2011.

[68] Carl Fredrik Carlborg, Kristinn Björgvin Gylfason, A Kaźmierczak, Fabian Dortu, MJ Banuls Polo, A Maquieira Catala, GM Kresbach, Hans

Sohlström, Thomas Moh, Laurent Vivien, et al. A packaged optical slot-waveguide ring resonator sensor array for multiplex label-free assays in labs-on-chips. Lab on a Chip, 10(3):281–290, 2010.

[69] Peter Kozma, András Hámori, Sándor Kurunczi, Kaspar Cottier, and Robert Horvath. Grating coupled optical waveguide interferometer for label-free biosensing. Sensors and Actuators B: Chemical, 155(2):446–450, 2011.

[70] James T Kirk, Gina E Fridley, Jeffrey W Chamberlain, Elijah D Christensen, Michael Hochberg, and Daniel M Ratner. Multiplexed inkjet functionalization of silicon photonic biosensors. Lab on a Chip, 11(7):1372–1377, 2011.

[71] Guillaume Suárez, Young-Hyun Jin, Janko Auerswald, Stefan Berchtold, Helmut F Knapp, Jean-Marc Diserens, Yves Leterrier, Jan-Anders E Månson, and Guy Voirin. Lab-on-a-chip for multiplexed biosensing of residual antibiotics in milk. Lab on a Chip, 9(11):1625–1630, 2009.

[72] Andrea Crespi, Yu Gu, Bongkot Ngamsom, Hugo JWM Hoekstra, Chaitanya Dongre, Markus Pollnau, Roberta Ramponi, Hans H van den Vlekkert, Paul Watts, Giulio Cerullo, et al. Three-dimensional mach-zehnder interferometer in a microfluidic chip for spatially-resolved label-free detection. Lab on a Chip, 10(9):1167–1173, 2010.

[73] Kirill E Zinoviev, Ana Belén González-Guerrero, Carlos Domínguez, and Laura M Lechuga. Integrated bimodal waveguide interferometric biosensor for label-free analysis. Journal of Lightwave Technology, 29(13):1926–1930, 2011.

[74] RG Heideman and PV Lambeck. Remote opto-chemical sensing with extreme sensitivity: design, fabrication and performance of a pigtailed integrated optical phase-modulated mach–zehnder interferometer system. Sensors and Actuators B: Chemical, 61(1):100–127, 1999.

[75] Maria B Dühring and Ole Sigmund. Improving the acousto-optical interaction in a mach–zehnder interferometer. Journal of Applied Physics, 105(8):083529, 2009.

[76] B Sepúlveda, G Armelles, and Laura M Lechuga. Magneto-optical phase modulation in integrated mach–zehnder interferometric sensors. Sensors and Actuators A: Physical, 134(2):339–347, 2007.

[77] Stefania Dante, Daphné Duval, Borja Sepúlveda, Ana Belen González-Guerrero, José Ramón Sendra, and Laura M Lechuga. All-optical phase modulation for integrated interferometric biosensors. Optics express, 20(7):7195–7205, 2012.

[78] Mario Castaño-Álvarez, M Teresa Fernández-Abedul, Agustín Costa-García, María Agirregabiria, Luis J Fernández, Jesús Miguel Ruano-López, and Borja Barredo-Presa. Fabrication of su-8 based microchip electrophoresis with integrated electrochemical detection for neurotransmitters. Talanta, 80(1):24–30, 2009.

[79] R Vilares, C Hunter, I Ugarte, I Aranburu, J Berganzo, J Elizalde, and LJ Fernandez. Fabrication and testing of a su-8 thermal flow sensor. Sensors and Actuators B: Chemical, 147(2):411–417, 2010.

[80] Francisco J Blanco, M Agirregabiria, J Berganzo, K Mayora, J Elizalde, A Calle, Carlos Domínguez, and Laura M Lechuga. Microfluidic-optical integrated cmos compatible devices for label-free biochemical sensing. Journal of Micromechanics and Microengineering, 16(5):1006, 2006.

[81] MT Arroyo, LJ Fernández, M Agirregabiria, N Ibanez, J Aurrekoetxea, and FJ Blanco. Novel all-polymer microfluidic devices monolithically integrated within metallic electrodes for sds-cge of proteins. Journal of Micromechanics and Microengineering, 17(7):1289, 2007.

[82] Mark D Turner, Belinda Nedjai, Tara Hurst, and Daniel J Pennington. Cytokines and chemokines: at the crossroads of cell signalling and inflammatory disease. Biochimica et Biophysica Acta (BBA)-Molecular Cell Research, 1843(11):2563–2582, 2014.

[83] Elzbieta Kolaczkowska and Paul Kubes. Neutrophil recruitment and function in health and inflammation. Nature Reviews Immunology, 13(3):159–175, 2013.

[84] Marcie R Williams, Verónica Azcutia, Gail Newton, Pilar Alcaide, and Francis W Luscinskas. Emerging mechanisms of neutrophil recruitment across endothelium. Trends in immunology, 32(10):461–469, 2011.

[85] Fran Balkwill. Cancer and the chemokine network. Nature Reviews Cancer, 4(7):540–550, 2004.

[86] Evanthia T Roussos, John S Condeelis, and Antonia Patsialou. Chemotaxis in cancer. Nature Reviews Cancer, 11(8):573–587, 2011.

[87] John Condeelis, Robert H Singer, and Jeffrey E Segall. The great escape: when cancer cells hijack the genes for chemotaxis and motility. Annu. Rev. Cell Dev. Biol., 21:695–718, 2005.

[88] Carlton R Cooper, Robert A Sikes, Brian E Nicholson, Yan-Xi Sun, Kenneth J Pienta, and Russell S Taichman. Cancer cells homing to bone: the significance of chemotaxis and cell adhesion. In The Biology of Skeletal Metastases, pages 291–309. Springer, 2004.

[89] Roberto Mayor and Eric Theveneau. The neural crest. Development, 140(11):2247–2251, 2013.

[90] Andras Czirok and Charles D Little. Pattern formation during vasculogenesis. Birth Defects Research Part C: Embryo Today: Reviews, 96(2):153–162, 2012.

[91] Stephen Boyden. The chemotactic effect of mixtures of antibody and antigen on polymorphonuclear leucocytes. Journal of Experimental Medicine, 115(3):453–466, 1962.

[92] Neysi Ibarra, Simone L Blagg, Francisca Vazquez, and Robert H Insall. Nap1 regulates dictyostelium cell motility and adhesion through scar-dependent and-independent pathways. Current biology, 16(7):717–722, 2006.

[93] Victoria Vinader, Yousef Al-Saraireh, Helen L Wiggins, Joshua Z Rappoport, Steve D Shnyder, Laurence H Patterson, and Kamyar Afarinkia. An agarose spot chemotaxis assay for chemokine receptor antagonists. Journal of pharmacological and toxicological methods, 64(3):213–216, 2011.

[94] Sally H Zigmond. Ability of polymorphonuclear leukocytes to orient in gradients of chemotactic factors. J. cell Biol, 75(2 Pt 1):606–616, 1977.

[95] DANIEL Zicha, GRAHAM A Dunn, and ALASTAIR F Brown. A new direct-viewing chemotaxis chamber. Journal of cell science, 99(4):769–775, 1991.

[96] Andrew J Muinonen-Martin, Douwe M Veltman, Gabriela Kalna, and Robert H Insall. An improved chamber for direct visualisation of chemotaxis. PloS one, 5(12):e15309, 2010.

[97] Jiandong Wu, Xun Wu, and Francis Lin. Recent developments in microfluidics-based chemotaxis studies. Lab on a Chip, 13(13):2484–2499, 2013.

[98] Sudong Kim, Hyung Joon Kim, and Noo Li Jeon. Biological applications of microfluidic gradient devices. Integrative Biology, 2(11-12):584–603, 2010.

[99] Thomas M Keenan and Albert Folch. Biomolecular gradients in cell culture systems. Lab on a Chip, 8(1):34–57, 2008.

[100] Noo Li Jeon, Stephan KW Dertinger, Daniel T Chiu, Insung S Choi, Abraham D Stroock, and George M Whitesides. Generation of solution and surface gradients using microfluidic systems. Langmuir, 16(22):8311–8316, 2000.

[101] Thomas M Keenan, Chia-Hsien Hsu, and Albert Folch. Microfluidic "jets" for generating steady-state gradients of soluble molecules on open surfaces. Applied physics letters, 89(11):114103, 2006.

[102] Ulrike Haessler, Yevgeniy Kalinin, Melody A Swartz, and Mingming Wu. An agarose-based microfluidic platform with a gradient buffer for 3d chemotaxis studies. Biomedical microdevices, 11(4):827–835, 2009.

[103] Shing-Yi Cheng, Steven Heilman, Max Wasserman, Shivaun Archer, Michael L Shuler, and Mingming Wu. A hydrogel-based microfluidic device for the studies of directed cell migration. Lab on a Chip, 7(6):763–769, 2007.

[104] Peter Friedl, Joseph Locker, Erik Sahai, and Jeffrey E Segall. Classifying collective cancer cell invasion. Nature cell biology, 14(8):777–783, 2012.

[105] Peter Friedl and Katarina Wolf. Tumour-cell invasion and migration: diversity and escape mechanisms. Nature Reviews Cancer, 3(5):362–374, 2003.

[106] Mahmut Yilmaz, Gerhard Christofori, and Francois Lehembre. Distinct mechanisms of tumor invasion and metastasis. Trends in molecular medicine, 13(12):535–541, 2007.

[107] FJ Blanco, M Agirregabiria, J Garcia, J Berganzo, M Tijero, MT Arroyo, JM Ruano, I Aramburu, and Kepa Mayora. Novel three-dimensional embedded su-8 microchannels fabricated using a low temperature full wafer adhesive bonding. Journal of Micromechanics and Microengineering, 14(7):1047, 2004.

[108] Toshikazu Yokoi, Akira Yamaguchi, Tetsuyo Odajima, and Kazunori Furukawa. Establishment and characterization of a human cell line derived from a squamous cell carcinoma of the tongue. 1988.

[109] Jens M Kelm, Nicholas E Timmins, Catherine J Brown, Martin Fussenegger, and Lars K Nielsen. Method for generation of homogeneous multicellular tumor spheroids applicable to a wide variety of cell types. Biotechnology and bioengineering, 83(2):173–180, 2003.

[110] Hongyang Li, Ying Dai, Jianchang Shu, Rongjie Yu, Yonglong Guo, and Jiansu Chen. Spheroid cultures promote the stemness of corneal stromal cells. Tissue and Cell, 47(1):39–48, 2015.

[111] Alexis D Armour, Heather M Powell, and Steven T Boyce. Fluorescein diacetate for determination of cell viability in tissue-engineered skin. Tissue Engineering Part C: Methods, 14(1):89–96, 2008.

[112] Antoine A Khalil and Peter Friedl. Determinants of leader cells in collective cell migration. Integrative biology, 2(11-12):568–574, 2010.

[113] Sandrine Etienne-Manneville. Neighborly relations during collective migration. Current opinion in cell biology, 30:51–59, 2014.

[114] Li Li, Robert Hartley, Bjoern Reiss, Yaohui Sun, Jin Pu, Dan Wu, Francis Lin, Trung Hoang, Soichiro Yamada, Jianxin Jiang, et al. E-cadherin plays an essential role in collective directional migration of large epithelial sheets. Cellular and Molecular Life Sciences, 69(16):2779–2789, 2012.

[115] Juergen Friedrich, Reinhard Ebner, and Leoni A Kunz-Schughart. Experimental anti-tumor therapy in 3-d: spheroids–old hat or new challenge? International journal of radiation biology, 83(11-12):849–871, 2007.

[116] Franziska Hirschhaeuser, Heike Menne, Claudia Dittfeld, Jonathan West, Wolfgang Mueller-Klieser, and Leoni A Kunz-Schughart. Multicellular tumor spheroids: an underestimated tool is catching up again. Journal of biotechnology, 148(1):3–15, 2010.

[117] LA Kunz-Schughart. Multicellular tumor spheroids: intermediates between monolayer culture and in vivo tumor. Cell biology international, 23(3):157–161, 1999.

[118] Alena Horská and Peter B Barker. Imaging of brain tumors: Mr spectroscopy and metabolic imaging. Neuroimaging clinics of North America, 20(3):293–310, 2010.

[119] Carolyn Mountford, Cynthia Lean, Peter Malycha, and Peter Russell. Proton spectroscopy provides accurate pathology on biopsy and in vivo. Journal of Magnetic Resonance Imaging, 24(3):459–477, 2006.

[120] Vicent Esteve, Bernardo Celda, and M Carmen Martínez-Bisbal. Use of 1h and 31p hrmas to evaluate the relationship between quantitative alterations in metabolite concentrations and tissue features in human brain tumour biopsies. Analytical and bioanalytical chemistry, 403(9):2611–2625, 2012.

[121] Vicent Esteve, Beatriz Martínez-Granados, and M Carmen Martínez-Bisbal. Pitfalls to be considered on the metabolomic analysis of biological samples by hr-mas. Frontiers in chemistry, 2:33, 2014.

[122] Gareth Jenkins and Colin D Mansfield. Microfluidic diagnostics: methods and protocols. Humana Press, 2013.

[123] Anna Bernardi, Jesus Jiménez-Barbero, Alessandro Casnati, Cristina De Castro, Tamis Darbre, Franck Fieschi, Jukka Finne, Horst Funken, Karl-Erich Jaeger, Martina Lahmann, et al. Multivalent glycoconjugates as anti-pathogenic agents. Chemical Society Reviews, 42(11):4709–4727, 2013.

[124] Elena Aznar, Ramón Martínez-Máñez, and Félix Sancenón. Controlled release using mesoporous materials containing gate-like scaffoldings. Expert opinion on drug delivery, 6(6):643–655, 2009.

[125] Núria Mas, Daniel Arcos, Lorena Polo, Elena Aznar, Sandra Sánchez-Salcedo, Félix Sancenón, Ana García, M Dolores Marcos, Alejandro Baeza, María Vallet-Regí, et al. Towards the development of smart 3d "gated scaffolds" for on-command delivery. small, 10(23):4859–4864, 2014.

[126] Shan Jiang, Khin Yin Win, Shuhua Liu, Choon Peng Teng, Yuangang Zheng, and Ming-Yong Han. Surface-functionalized nanoparticles for biosensing and imaging-guided therapeutics. Nanoscale, 5(8):3127–3148, 2013.

[127] Sungwook Jung, Jutaek Nam, Sekyu Hwang, Joonhyuck Park, Jaehyun Hur, Kyuhyun Im, Nokyoung Park, and Sungjee Kim. Theragnostic ph-sensitive gold nanoparticles for the selective surface enhanced raman scattering and photothermal cancer therapy. Analytical chemistry, 85(16):7674–7681, 2013.

[128] Marites P Melancon, Wei Lu, Meng Zhong, Min Zhou, Gan Liang, Andrew M Elliott, John D Hazle, Jeffrey N Myers, Chun Li, and R Jason Stafford. Targeted multifunctional gold-based nanoshells for magnetic resonance-guided laser ablation of head and neck cancer. Biomaterials, 32(30):7600–7608, 2011.

[129] Richard A Murray, Yuan Qiu, Fabrizio Chiodo, Marco Marradi, Soledad Penadés, and Sergio E Moya. A quantitative study of the intracellular dynamics of fluorescently labelled glyco-gold nanoparticles via fluorescence correlation spectroscopy. Small, 10(13):2602–2610, 2014.

[130] Ana Paula Candiota, Milena Acosta, Rui Vasco Simões, Teresa Delgado-Goñi, Silvia Lope-Piedrafita, Ainhoa Irure, Marco Marradi, Oscar Bomati-Miguel, Nuria Miguel-Sancho, Ibane Abasolo, et al. A new ex vivo method to evaluate the performance of candidate mri contrast agents: a proof-of-concept study. Journal of nanobiotechnology, 12(1):12, 2014.

[131] Anja van de Stolpe and Jaap den Toonder. Workshop meeting report organs-on-chips: human disease models. Lab on a chip, 13(18):3449–3470, 2013.

[132] Jamil El-Ali, Peter K Sorger, and Klavs F Jensen. Cells on chips. Nature, 442(7101):403–411, 2006.

[133] Lily Kim, Michael D Vahey, Hsu-Yi Lee, and Joel Voldman. Microfluidic arrays for logarithmically perfused embryonic stem cell culture. Lab on a Chip, 6(3):394–406, 2006.

[134] Lily Kim, Yi-Chin Toh, Joel Voldman, and Hanry Yu. A practical guide to microfluidic perfusion culture of adherent mammalian cells. Lab on a Chip, 7(6):681–694, 2007.

[135] Anna Tourovskaia, Xavier Figueroa-Masot, and Albert Folch. Differentiation-on-a-chip: a microfluidic platform for long-term cell culture studies. Lab on a Chip, 5(1):14–19, 2005.

[136] Eric K Sackmann, Anna L Fulton, and David J Beebe. The present and future role of microfluidics in biomedical research. Nature, 507(7491):181–189, 2014.

[137] Stephen J Blackband, David L Buckley, Jonathan D Bui, and M Ian Phillips. Nmr microscopy—beginnings and new directions. Magnetic Resonance Materials in Physics, Biology and Medicine, 9(3):112–116, 1999.

[138] Mikko I Kettunen and Kevin M Brindle. Apoptosis detection using magnetic resonance imaging and spectroscopy. Progress in Nuclear Magnetic Resonance Spectroscopy, 47(3):175–185, 2005.

[139] Helene Benveniste and Stephen J Blackband. Translational neuroscience and magnetic-resonance microscopy. The Lancet Neurology, 5(6):536–544, 2006.

[140] Klaus Ehrmann, Kristopher Pataky, Matthieu Stettler, Florian Maria Wurm, Jürgen Brugger, Pierre-André Besse, and Radivoje Popovic. Nmr spectroscopy and perfusion of mammalian cells using surface microprobes. Lab on a Chip, 7(3):381–383, 2007.

[141] Timothy M Shepherd, Bjorn Scheffler, Michael A King, Greg J Stanisz, Dennis A Steindler, and Stephen J Blackband. Mr microscopy of rat hippocampal slice cultures: a novel model for studying cellular processes and chronic perturbations to tissue microstructure. Neuroimage, 30(3):780–786, 2006.

[142] Samuel C Grant, Nanci R Aiken, H Daniel Plant, Stephen Gibbs, Thomas H Mareci, Andrew G Webb, and Stephen J Blackband. Nmr spectroscopy of single neurons. Magnetic resonance in medicine, 44(1):19–22, 2000.

[143] SC Grant, DL Buckley, S Gibbs, AG Webb, and SJ Blackband. Mr microscopy of multicomponent diffusion in single neurons. Magnetic Resonance in Medicine, 46(6):1107–1112, 2001.

[144] Daphné Duval, Ana Belén González-Guerrero, Stefania Dante, Johann Osmond, Rosa Monge, Luis J Fernández, Kirill E Zinoviev, Carlos Domínguez, and Laura M Lechuga. Nanophotonic lab-on-a-chip platforms including novel bimodal interferometers, microfluidics and grating couplers. Lab on a Chip, 12(11):1987–1994, 2012.

[145] J Liu, B Cai, J Zhu, G Ding, X Zhao, C Yang, and D Chen. Process research of high aspect ratio microstructure using su-8 resist. Microsystem Technologies, 10(4):265–268, 2004.

[146] Om Prakash Parida and Navakant Bhat. Characterization of optical properties of su-8 and fabrication of optical components. In Int. Conf. on Opt. and Photon.(CSIO), pages 4–7, 2009.

[147] Ane Altuna, Gemma Gabriel, Liset Menéndez de la Prida, María Tijero, Anton Guimerá, Javier Berganzo, Rafa Salido, Rosa Villa, and Luis J Fernández. Su-8-based microneedles for in vitro neural applications. Journal of Micromechanics and Microengineering, 20(6):064014, 2010.

[148] Luis J Fernández, Ane Altuna, Maria Tijero, Gemma Gabriel, Rosa Villa, Manuel J Rodríguez, Montse Batlle, Roman Vilares, Javier Berganzo, and FJ Blanco. Study of functional viability of su-8-based microneedles for neural applications. Journal of Micromechanics and Microengineering, 19(2):025007, 2009.

[149] Ming Ni, Wen Hao Tong, Deepak Choudhury, Nur Aida Abdul Rahim, Ciprian Iliescu, and Hanry Yu. Cell culture on mems platforms: a review. International journal of molecular sciences, 10(12):5411–5441, 2009.

[150] Geoffrey Kotzar, Mark Freas, Phillip Abel, Aaron Fleischman, Shuvo Roy, Christian Zorman, James M Moran, and Jeff Melzak. Evaluation of mems materials of construction for implantable medical devices. Biomaterials, 23(13):2737–2750, 2002.

[151] Krishnamurthy V Nemani, Karen L Moodie, Jeoffry B Brennick, Alison Su, and Barjor Gimi. In vitro and in vivo evaluation of su-8 biocompatibility. Materials Science and Engineering: C, 33(7):4453–4459, 2013.

[152] LG Rigat-Brugarolas, A Elizalde-Torrent, M Bernabeu, M De Niz, L Martin-Jaular, C Fernandez-Becerra, A Homs-Corbera, J Samitier, and HA del Portillo. A functional microengineered model of the human splenon-on-a-chip. Lab on a Chip, 14(10):1715–1724, 2014.

[153] Karen Y Torrejon, Dennis Pu, Magnus Bergkvist, John Danias, Susan T Sharfstein, and Yubing Xie. Recreating a human trabecular meshwork outflow system on microfabricated porous structures. Biotechnology and bioengineering, 110(12):3205–3218, 2013.

[154] Henrik Ahlenius and Zaal Kokaia. Isolation and generation of neurosphere cultures from embryonic and adult mouse brain. Mouse Cell Culture: Methods and Protocols, pages 241–252, 2010.

[155] Sara Gil-Perotín, María Duran-Moreno, Arantxa Cebrián-Silla, Mónica Ramírez, Paula García-Belda, and José Manuel García-Verdugo. Adult neural stem cells from the subventricular zone: a review of the neurosphere assay. The Anatomical Record, 296(9):1435–1452, 2013.

[156] M Carmen Martínez-Bisbal, Vicent Esteve, Beatriz Martínez-Granados, and Bernardo Celda. Magnetic resonance microscopy contribution to interpret high-resolution magic angle spinning metabolomic data of human tumor tissue. BioMed Research International, 2011, 2010.

[157] L Moroni, JR De Wijn, and CA Van Blitterswijk. Integrating novel technologies to fabricate smart scaffolds. Journal of Biomaterials Science, Polymer Edition, 19(5):543–572, 2008.

[158] Yu-Hsiang Wang, Chang-Pen Chen, Chih-Ming Chang, Chia-Pin Lin, Che-Hsin Lin, Lung-Ming Fu, and Chia-Yen Lee. Mems-based gas flow sensors. Microfluidics and nanofluidics, 6(3):333, 2009.

[159] Yoshihiro Mizuno, Matthieu Liger, and Yu-Chong Tai. Nanofluidic flowmeter using carbon sensing element. In Micro Electro Mechanical Systems, 2004. 17th IEEE International Conference on.(MEMS), pages 322–325. IEEE, 2004.

[160] M Dijkstra, MJ De Boer, JW Berenschot, TSJ Lammerink, RJ Wiegerink, and M Elwenspoek. Miniaturized thermal flow sensor with planar-integrated sensor structures on semicircular surface channels. Sensors and Actuators A: Physical, 143(1):1–6, 2008.

[161] RJ Wiegerink, TSJ Lammerink, M Dijkstra, and J Haneveld. Thermal and coriolis type micro flow sensors based on surface channel technology. Procedia Chemistry, 1(1):1455–1458, 2009.

[162] Tao Wang and Roger Baker. Coriolis flowmeters: a review of developments over the past 20 years, and an assessment of the state of the art and likely future directions. Flow Measurement and Instrumentation, 40:99–123, 2014.

[163] Peter Enoksson, Goran Stemme, and Erik Stemme. A silicon resonant sensor structure for coriolis mass-flow measurements. Journal of microelectromechanical systems, 6(2):119–125, 1997.

[164] J Haneveld, TSJ Lammerink, MJ De Boer, RGP Sanders, Aditya Mehendale, JC Lötters, M Dijkstra, and RJ Wiegerink. Modeling, design, fabrication and characterization of a micro coriolis mass flow sensor. Journal of Micromechanics and Microengineering, 20(12):125001, 2010.

[165] Wouter Sparreboom, Jan Van De Geest, Marcel Katerberg, Ferry Postma, Jeroen Haneveld, Jarno Groenesteijn, Theo Lammerink, Remco Wiegerink, and Joost Lötters. Compact mass flow meter based on a micro coriolis flow sensor. Micromachines, 4(1):22–33, 2013.

[166] J Groenesteijn, M Dijkstra, TSJ Lammerink, JC Lötters, and RJ Wiegerink. A compact micro coriolis mass flow sensor with flow bypass for a monopropellant micro propulsion system. 2014.

[167] J Groenesteijn, TSJ Lammerink, RJ Wiegerink, J Haneveld, and JC Lötters. Optimization of a micro coriolis mass flow sensor using lorentz force actuation. Sensors and Actuators A: Physical, 186:48–53, 2012.

[168] Aitor Ezkerra, Luis José Fernández, Kepa Mayora, and Jesús Miguel Ruano-López. Su8 diaphragm micropump with monolithically integrated cantilever check valves. Lab on a Chip, 11(19):3320–3325, 2011.

[169] Cheng Luo, Thomas W Schneider, Robert C White, John Currie, and Makarand Paranjape. A simple deflection-testing method to determine poisson's ratio for mems applications. Journal of Micromechanics and Microengineering, 13(1):129, 2002.

[170] J Groenesteijn, L van de Ridder, JC Lötters, and RJ Wiegerink. Modelling of a micro coriolis mass flow sensor for sensitivity improvement. In SENSORS, 2014 IEEE, pages 954–957. IEEE, 2014.